DOCTOR OF PHILOSOPHY

The characterisation of porous carbons using computer modelling and experimental techniques

Scaife, Sara Jo

Award date:
1999

Awarding institution:
University of Wales, Bangor

The Characterisation of Porous Carbons Using Computer Modelling and Experimental Techniques

A thesis submitted

by

S. J. Scaife

to the University of Wales, Bangor

in candidature for the degree of

Philosophiae Doctor

September 16, 1999

Abstract

To characterise accurately the surface of porous carbons a combination of molecular models and experimental techniques is used. The nature of graphitic and activated carbon surfaces and their adsorption characteristics are investigated by scanning electron microscopy, x-ray diffraction and experimental and theoretical adsorption isotherms. The nature of the pore spaces filled by different gases at different temperatures are explored using molecular models at the nanoscale and structural models (slit-pore) on the mesoscale. Density Functional Theory which is based on statistical mechanics was used to model adsorption isotherms for various gases at 77K and 293K in idealised porous systems.

Porous carbons were characterised by applying a numerical method to determine the distribution of pores of varying size. The reliability of the pore size distribution, widely determined from nitrogen adsorption isotherms at 77K, has been improved by considering other gases such as argon, carbon-dioxide and methane and higher temperatures. Finally, the pore size distribution of a typical microporous carbon was used to predict its adsorption selectivity properties.

Acknowledgements

Many thanks to my supervisor Prof N. Quirke and tutor Dr J. N. Macdonald for their guidance and support. I also thank colleagues from the Computational Chemistry Group at Bangor.

Special thanks to Peter, Adam, Ernie, Mark and Flo for their patience and help.

I am particularly grateful for the funding and opportunity provided by Coulter Ltd to pursue this doctorate.

This work is dedicated to S. Brown and P. Carroll.

S. J. Scaife 16th September 1999.

Contents

List of Figures

List of Tables

Chapter 1

Introduction

The accumulation of molecules at a surface is known as adsorption. The physical properties of these particles will be different from those of the particles in the bulk phase. Many industrial processes involve adsorption in materials which have microstructures (i.e. pores on the nanometre and sub-nanometre scale). For example, molecular sieves (materials with a porous microstructure) are used as filters for the separation and purification of gases. In order to understand and improve these processes we need to understand the properties of molecules on surfaces and in pores.

There are many different types of adsorbent. This work is concerned with non-porous and porous carbons (also called activated carbons). Elemental carbon exists in 2 crystalline forms; diamond and graphite most carbon is found in non-graphitic forms such as coals, chars and cokes.

Non-graphitic carbons are divided into two groups; graphitisable carbons are those which can be converted into graphitic carbons by heat treatment [11] see Fig 1.1.

Figure 1.1: *Types of Carbon*

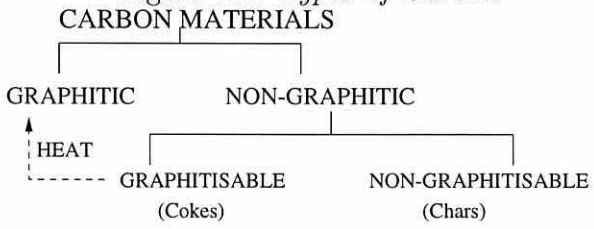

Poly-aromatic compounds such as naphthalene, anthracene and phenanthrene carbonise to graphitisable, anisotropic cokes when heated to 700^0C or more.

The non-graphitisable carbons or chars are the products of carbonisation from

substances such as wood and highly volatile bituminous coals.

Heating non-graphitisable materials at temperatures $<700^0$C (pyrolysis) changes their structure and at temperatures above $>700^0$C, carbonisation occurs and disruption of the original polymers occurs. During pyrolysis small molecules such as water and carbon-dioxide are removed from the macromolecular network and a new lattice is created continuously with a higher ratio of carbon to hydrogen and carbon to oxygen. Carbon atoms re-adjust their positions and approximate to the 6-membered ring systems found in the more stable state of graphitic carbon (which has a lamellar like structure) and as a result considerable strain energy is introduced in the new lattice. Due to the defective nature of the newly formed ring systems the density of the carbon (approx $1 g.cm^{-3}$) is less than that of single crystal graphite ($2.267 g.cm^{-3}$). The spaces between the disrupted, randomly bonded ring systems constitute the microporosity of the carbon. Graphitisable carbons are less defective containing little porosity and have densities of approx $2 g.cm^{-3}$.

Activated carbons are therefore porous carbon materials derived from chars which have been gasified with steam or carbon-dioxide in the range 700-1100^{0}C (physical activation) or have been treated with compounds such as $ZnCl_2$ and H_3PO_4 (chemical activation), during or after carbonisation to increase their porosity. However, the method by which porosity increases is not well understood. Activated carbons are characterised by internal surface areas ranging from approximately 500 to $3000 m^2.g^{-1}$.

The use of activated carbons dates back as early as 2000BC in their application to water purification [9]. During World War I, granular activated carbon was

manufactured for use in gas masks. Today, approximately 240000 tons per year of activated carbons is used for liquid phase applications and 60000 tons per year for gas-phase applications worldwide [10].

1.1 Types of adsorption

Molecules can attach to surfaces in 2 ways. In chemisorption bonds are formed between the adsorbate and substrate, and adsorption is often via dissociation of the molecule into fragments. The enthalpy of adsorption is usually around -200kJ.mol^{-1} [27] and can take place at high temperatures, leading to a monolayer. The incremental increase in the amount adsorbed decreases with each incremental increase in pressure.

Physical adsorption is a similar process to condensation, Van der Waals forces are involved (i.e. a dipole, non-polar or electrostatic interaction). The enthalpy of adsorption is typically -20kJ.mol^{-1} [27], and the adsorbed molecule retains its identity. Adsorption is only appreciable at low temperatures (i.e. below the boiling point of the material) and multilayer adsorption occurs. The amount of adsorption is more a function of the adsorbate rather than the substrate here. The incremental increase in the amount adsorbed increases with each incremental increase in pressure of the bulk gas.

The variation in potential energy of a molecule with its distance from the substrate surface is shown in Figs 1.2 and 1.3 for chemisorption. A molecule's potential energy falls as it approaches the surface and becomes physisorbed (a precursor state

for chemisorption). As the molecule's bonds are stretched away from equilibrium there is an initial rise in energy. This is followed by a rapid decrease in energy as the molecule becomes chemisorbed, and dissociation into fragments often occurs. Referring to the potential energy profiles for the dissociative chemisorption of an $A-A$ molecule (Figs 1.2 and 1.3), P is the enthalpy of non-dissociative physisorption and C that for chemisorption (at $T = 0$).

Figure 1.2: *Potential Energy Profile for Non-activated Chemisorption.*

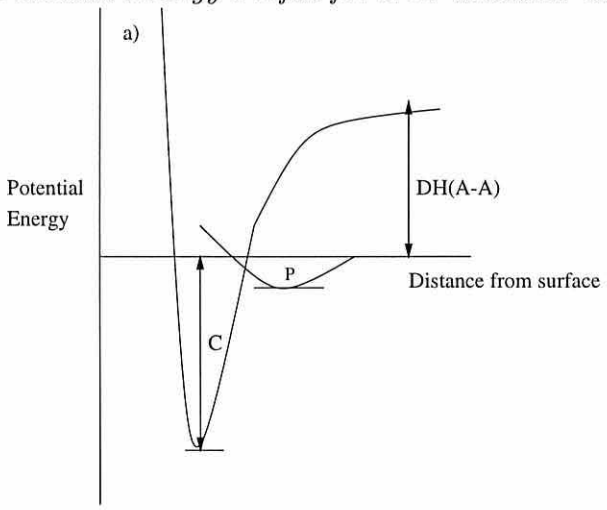

When the potential energy barrier separating the physisorbed and chemisorbed states is low (Fig 1.2), chemisorption is a non-activated process and is rapid. Activated chemisorption is a much slower process and occurs when the activation barrier is high (Fig 1.3).

Figure 1.3: *Potential Energy Profile for Activated Chemisorption.*

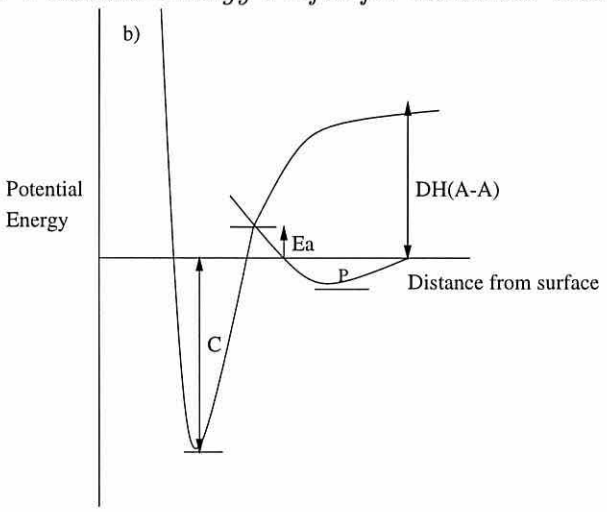

Therefore, depending on the activation energy barrier, chemisorption may be a fast or slow process and the rates of adsorption are not a reliable way of distinguishing between the 2 different types of adsorption. The principal test to distinguish between chemi and physisorption is the enthalpy of adsorption.

The extent of surface coverage depends on the pressure of the bulk gas; a graphical representation of this is an *adsorption isotherm.* The type of adsorption observed in pores is markedly different for different pore size sizes. A classification scheme for pores, determined by their size, has been devised by IUPAC [56] and is shown in Table 1.1. Isotherms can generally be divided into a finite number of types. Fig 1.4 shows 6 basic isotherm types as gas uptake plotted against pressure. The isotherm types in Fig 1.4 are known as the BET classification [30].

Table 1.1: *IUPAC Classification Scheme.*

Pore Type	**Pore Size (Å)**
Macropore	> 500
Mesopore	20 to 500
Super-micropore	7 to 20
Ultra-micropore	< 7

In large pores (macropores) there is no interaction from opposing walls and a monolayer is formed in the initial low pressure region. This type of filling is observed in the physical adsorption of vapours onto low-surface area adsorbents and gives an adsorption isotherm of the form of Type II of the BET classification (shown in Fig 1.4). Where gas uptake is plotted against the relative pressure. The first point of inflexion in the isotherm (marked by the arrow in Fig 1.4) where the linear region begins, corresponds to a complete monolayer.

A second type of filling behaviour is found in macropores where the adsorption curve is convex to the pressure axis has the shape of the Type III isotherm of the BET classification. This corresponds to the adsorption of vapours on low-surface area adsorbents where a weak interaction between the surface and adsorbing molecules exists.

Figure 1.4: *BET Classification of Isotherms.*

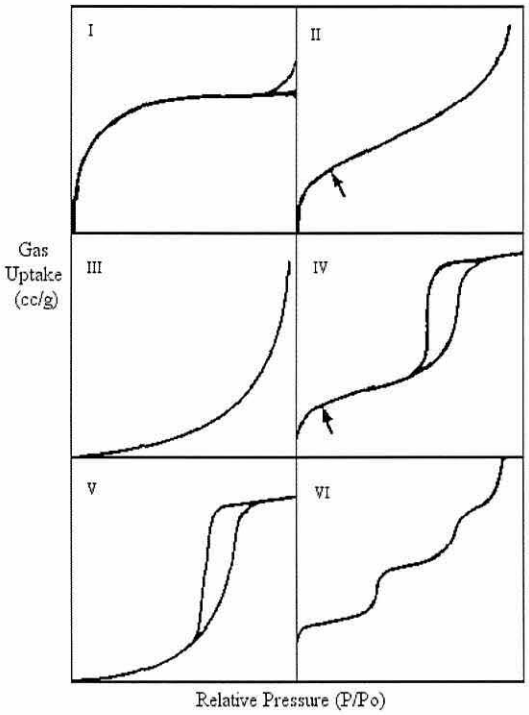

The type of filling observed in mesopores is similar to that observed in macropores where a monolayer is formed at low pressures. A hysteresis loop occurs where the adsorption and desorption branches of the isotherm are non-overlapping. This is associated with capillary condensation of the adsorbate to a liquid in mesopores to give a Type IV isotherm (Fig 1.4). Where the hysteresis loop opens, the monolayer is completed, at higher pressures a multilayer builds up until the pores are completely filled with adsorbate in a liquid form. The isotherms observed from the adsorption in mesopores do not approach infinite adsorption asymptotically at the saturation vapour pressure (as occurs in macroporous systems) instead they give a branch which is almost horizontal to the pressure axis where adsorption increases very slowly due to compression in the liquid-filled pore. When the interaction between the surface

and adsorbing molecules is weak in a mesoporous material, a Type V isotherm is observed (Fig 1.4).

The adsorption isotherm associated with adsorption in a micropore gives a curve concave to the pressure axis and then forms a long, flat branch, almost horizontal when the pores are filled. Adsorption in micropores therefore leads to an isotherm of Type I (Fig 1.4).

The Type VI isotherm has steps which represent complete formation of successive monomolecular layers. It has been proposed [60] that extremely homogenous, non-porous surfaces yield Type VI isotherms.

The aim of this thesis was to apply the method of Quirke and coworkers [83] in order to explore the nature of the adsorption of different gases with graphitic and activated carbon surfaces, the nature of the pore spaces as seen by different gases at different temperatures and to determine whether or not the pore size distribution describing the amorphous carbons could be used to predict adsorption properties such as selectivity. This was achieved using molecular models at the nanoscale, structural models (a slit pore) on the mesoscale and experimental techniques.

An approximate theory called Density Functional Theory, which can be applied to classical fluids and is based on statistical mechanics was used to calculate theoretical adsorption isotherms for various gases at 77K and 293K in idealised porous systems. This theory is described in Chapter 2.

The method of measuring experimental adsorption isotherms is explained in Chapter 3, with a review of methods which may be used to calculate the specific surface area of adsorbents.

Chapter 4 is concerned with the behaviour of gases adsorbing onto low surface area carbons which can be compared directly with the semi-empirical, modelled isotherms. The sensitivity to parameters describing the interaction between adsorbate-adsorbate and adsorbate and adsorbent molecules were investigated and optimised in order to attain the best possible fit of theory to experiment for the adsorption of various gases at 77K and 293K.

The pore size distributions of various activated carbons were calculated from adsorption isotherms at 77K and 293K of various gases in Chapter 5 and a method of calculating the selectivity properties of a typical activated carbon are presented in Chapter 6.

Chapter 2

Statistical Thermodynamics of Adsorption

2.1 Introduction

This chapter describes three areas of theory which are of central importance to the thesis. The first deals with the principles underlying statistical mechanics which allows one to predict macroscopic properties from knowledge of the molecular state of the system.

The simple case where molecular interactions are neglected, along with the method of calculating the macroscopic properties of such a system are presented in Section (2.2.2). These methods can be applied to dilute gases for example. Macroscopic properties can be calculated for a real system where molecular interactions are taken into account by introducing the concept of ensembles (Section 2.2.4).

Section (2.2) provides the necessary background material for the second area of theory; Density Functional Theory. This is an approximate theory based on statistical mechanics and can be directly applied to problems involving adsorption (Section 2.3). In essence, DFT is used to calculate adsorption isotherms which are compared with those obtained experimentally for low surface area carbons. Finally, the adsorption isotherms calculated using DFT can be used in combination with the experimentally measured adsorption isotherms to determine the pore size distribution of the adsorbate surface. This is achieved numerically using a minimisation algorithm to match the two isotherms by varying the parameters (describing the pore size distribution) used to calculate the theoretical isotherm.

2.2 Statistical Mechanics

2.2.1 Microscopic vs Macroscopic

A portion of matter separated from its surroundings by a boundary is called a *system*. A system is *open* if a *flow of matter* across the boundaries is possible; otherwise it is *closed*. Where there is no interaction whatever between a system and its surroundings we have an *isolated system*. The system may be observed on a *macroscopic* level where we consider a large number of molecules of the order 10^{19}cm^{-3} and the thermodynamic properties of the system such as the volume and pressure can in general be directly measured as no molecular assumptions are required.

On the *microscopic* level, assumptions are made about the types of atoms, and the forces between them. There will be a large number of quantum states consistent with fixed macroscopic properties. The state of a system must be known in order to calculate a thermodynamic property as the values of that property will differ in each possible quantum state. However, it is impossible to experimentally determine which of the $3\text{x}10^{19}$ (at least) possible microstates at any instant a system is in, even with the aid of the best computer, and therefore thermodynamic properties of the system cannot be measured directly.

The thermodynamic properties of a macroscopic system depend only on the average behaviour of all the atoms in that system, i.e the average of the microstates. To illustrate this point consider how we describe the macroscopic property *pressure*. The pressure of a gas is the average force per unit area exerted by its molecules. There is no differentiation between the force resulting from each individual atom

i.e. collisions. The average behaviour of many atoms is predicted from statistical methods. Statistical mechanics provides a bridge between the macroscopic and microscopic levels of a system whereby 'the macroscopic properties are expressed in terms of the average values of microscopic properties' [25]. Depending on the state of a system, its statistical mechanics may be classified as shown in Fig 2.1. The treatment of systems in equilibrium is called statistical thermodynamics. Thermodynamics provides mathematical relations between the various experimental properties of macroscopic systems in equilibrium, without considering the constitution of matter. Statistical thermodynamics calculates thermodynamic properties from a molecular point of view, i.e it assumes the existence of atoms and molecules.

Figure 2.1: *Techniques of Statistical Mechanics*

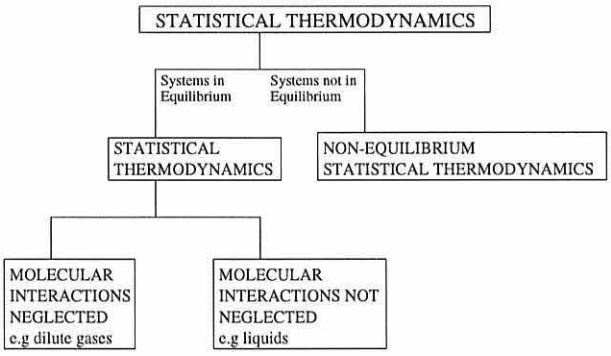

The techniques of statistical mechanics allow us to predict the macroscopic properties (e.g pressure, temperature, internal energy) from assumptions concerning the microscopic states of the system. This thesis is concerned with the application of the techniques of statistical thermodynamics to the physical problems of adsorption where molecular interactions are taken into account.

2.2.2 Average Behaviour of Non-Interacting Molecules

In order to calculate macroscopic properties such as density, the average value of the microscopic states constituting the system must be calculated. Accounting for the effects of molecular interactions increases the complexity of the problem (this will be elaborated on from Section 2.2.4 onwards). First the case where molecular interactions are neglected, as it is simpler and will provide interesting and helpful background material for what is to follow.

Consider a system composed of N molecules, each molecule may exist in states with energies ϵ_0, ϵ_1, ϵ_2 ... where ϵ_0, the lowest state, is taken as the zero of energy, $\epsilon_0 = 0$. The total energy of the system is a constant E_t and is a sum of the individual energies, i.e. the molecules are 'independent' so that interactions between them are negligible. We are in fact dealing with a perfect gas:

$$E_t = \sum_{i=1}^{N} \epsilon_i \tag{2.1}$$

Where ϵ_i is the energy of the i_{th} molecule and N is the total number of molecules. In reality, interaction between molecules will of course occur; energy will be re-distributed amongst the molecules and their modes of motion, and a dynamic equilibrium will be reached, however we assume that such interactions are weak.

In a given quantum state let there be n_i molecules in a state of energy ϵ_i at temperature T. At equilibrium we can calculate the populations of these energy levels (i.e the number of molecules n_1 having energy ϵ_1 and n_2 having energy ϵ_2 etc) using statistical thermodynamics. In order to do this we assume a priori that

all energy levels have equal likelihood of being occupied whatever their nature.

At an instant in time a particle may find itself in a different quantum state, but on average, n_1 molecules will occupy the quantum state with energy ϵ_1, and n_2 molecules will occupy the quantum state with energy ϵ_2. This is the equilibrium assumption and it implies that the population of the microstates does not change with time.

The number of *distinguishable*[1] ways in which N molecules can be arranged in their available states is called the *weight* of the configuration[2], the *thermodynamic probability* of the particular macrostate or the *number of microstates*. It is given by:

$$W = \frac{N!}{n_0!\ n_1!\ n_2!\ \ldots} \tag{2.2}$$

Where W is the weight, N is the total number of molecules in the system and n_0 is the number of molecules in state ϵ_0 and n_1 is the number of molecules in state ϵ_1.

When W is a maximum, the number of molecules will be evenly distributed amongst the available states (if the energies of the states do not differ). The system will also be at equilibrium and the most probable distribution will be achieved.

[1]The systems are distinguishable since they are macroscopic systems.

[2]The specification of a set of populations n_0, $n_1 \cdots$ in the form $\{n_0, n_1 \cdots\}$ is called the instantaneous configuration of the system.

2.2.3 The Most Probable Distribution

The most probable configuration of the system will have a weight which is greater than that corresponding to less probable configurations. Therefore, in order to find the most probable distribution we need to find the values of n_0, n_1 ... which render W a maximum. However, the total energy of the system, E_t, and the total number of molecules in the system, N, must remain a constant. Thus:

$$\sum_i n_i \, \epsilon_i = E_t = constant \tag{2.3}$$

Where E_t is the total energy of the system and

$$\sum_i n_i = N = constant \tag{2.4}$$

Where N is the total number of molecules in the system.

For N independent molecules at thermal equilibrium, the most probable distribution of these molecules amongst the various states n_1, n_2, of energies ϵ_1, ϵ_2 is known as the *Boltzmann Distribution*, and is often written as:

$$p_i = \frac{e^{-\beta\epsilon_i}}{q} \tag{2.5}$$

Where $p_i = \frac{n_i}{N}$ is the fraction of molecules in state i, and $\beta = \frac{1}{kT}$ [26]. The *molecular partition function* q is expressed as:

$$q = \sum_j e^{-\beta\epsilon_j} \tag{2.6}$$

It is a measure of how the total number of molecules are distributed over those states which are thermally accessible at the temperature, T, of the system. At thermal equilibrium, the thermodynamic properties of a system of independent molecules are calculated from q. Thus q plays a key role in statistical thermodynamics. Now consider systems in which molecular interactions take place i.e. those which are used to describe adsorption processes.

2.2.4 Interacting Molecules and Ensembles

When considering systems composed of interacting molecules the concept of an *ensemble* must be introduced. Take a collection of particles in a closed system, where no matter may transfer across the system's boundaries. The system is characterised by independent thermodynamic variables and is thus a replica (on a macroscopic level) of the thermodynamic system to be studied. Replication of this system X times produces an *ensemble of systems*.

In a *canonical ensemble* (Fig 2.2) [26] we first combine X systems of a specified volume, V, with walls that are impermeable to the passage of molecules but are heat conducting. Each system containing N particles is immersed in a heat bath at temperature T. In such a thermodynamic system the energy is able to fluctuate. Once equilibrium is established the entire ensemble is at a uniform temperature, T and each system has the same fixed values of N and V. The entire ensemble is then thermally insulated (i.e. the walls of the entire ensemble are not heat conducting), isolated and referred to as a *supersystem*.

Figure 2.2: *A Canonical Ensemble.*

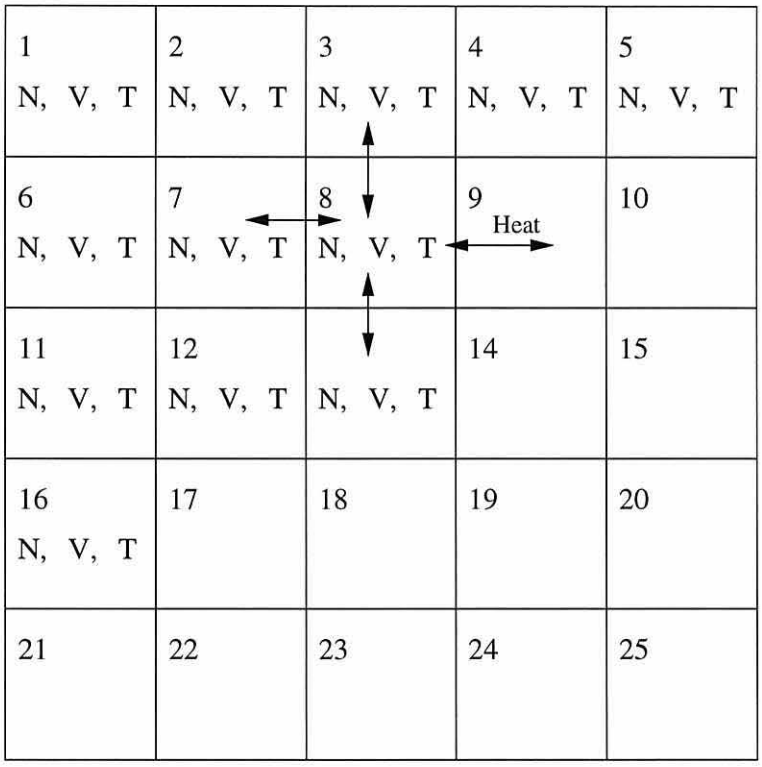

The supersystem is characterised by the volume, XV, a total energy E_t and a total number of molecules XN. As each system in the ensemble is not isolated, the energy of each system is not fixed at a specific value. The average values of a mechanical variable[3] such as energy may be calculated at equilibrium. However, we must consider all possible energy states for each system of the ensemble i.e. $E_1(N,V)$, $E_2(N,V)$ and so on, such that $E_{j+1} \geq E_j$. At any one time a given number of systems a_1 of the ensemble will be found in state 1 with energy E_1:

[3]Mechanical variables are those that have well defined values in a given quantum state.

State No.	1	2	3	$\cdots$	l
Energy	E_1	E_2	E_3	$\cdots$	E_l
Occupation No	a_1	a_2	a_3	$\cdots$	a_l

The occupation number describes the number of systems of the ensemble in that particular set, and a set of occupation numbers is a distribution, $\{a_j\} = \mathbf{a}$.

In the canonical ensemble the total number of systems is constant at X;

$$\sum_j a_j = X \tag{2.7}$$

and the entire canonical ensemble (which is isolated) has some fixed energy E_t;

$$\sum_j a_j E_j = E_t \tag{2.8}$$

Taking into account Equations (2.7) and (2.8) every distribution of occupation numbers is equally probable. The number of different distributions is given by the weight:

$$W(\mathbf{a}) = \frac{X!}{\prod_j a_j!} \tag{2.9}$$

The set of a_j's which maximise $W(\mathbf{a})$, under the constraints in Equations (2.7) and (2.8), is denoted a_j^* and is called the most probable distribution. With fixed N, V and T the probability P_j that a system is in the j_{th} quantum state is thus:

$$P_j = \frac{1}{X}\frac{W(\mathbf{a}^*)\, a_j^*}{W(\mathbf{a}^*)} = \frac{a_j^*}{X} \tag{2.10}$$

The canonical ensemble averages of a mechanical variable such as energy may be calculated from:

$$\bar{M} = \sum_j M_j P_j \tag{2.11}$$

Where M_j is the value of M in the j_{th} quantum state. Applying Lagrange's method of undetermined multipliers [5] the most probable distribution in terms of the Lagrange multipliers (α and β) is:

$$a_j^* = X e^{-\alpha} e^{-\beta E_j} \quad j = 1, 2 \cdots \tag{2.12}$$

Where $\beta = \frac{1}{kT}$. Substituting the distribution Equation (2.12) into Equation (2.7) and Equation (2.8) gives:

$$e^{\alpha} = \sum_j e^{-\beta E_j} \tag{2.13}$$

Elimination of $e^{-\alpha}$ in Equation (2.12) by use of Equation (2.13) gives :

$$P_j = \frac{a_j^*}{X} = \frac{e^{-\beta E_j(N,V)}}{\sum_j e^{-\beta E_j(N,V)}} \quad j = 1, 2 \cdots \tag{2.14}$$

Where the denominator of Equation (2.14) is called the *canonical (ensemble) partition function*, Q:

$$Q\,(N, V, T) = \sum_j e^{-E_j(N,V)/kT} \tag{2.15}$$

and serves as a bridge between the quantum mechanical energy states of a macroscopic system and the thermodynamic properties of that system.

To obtain the expression for the average of a mechanical property such as energy, Equation (2.14) is substituted into Equation (2.11):

$$\bar{E} = \bar{E}(N, V, \beta) = \frac{\sum_j E_j(N, V)\, e^{-\beta E_j(N,V)}}{\sum_j e^{-\beta E_j(N,V)}} \tag{2.16}$$

The average energy $\bar{E}$ corresponds to the thermodynamic energy E, according to the ensemble postulate of Gibbs. Equation (2.16) can be written in terms of Q:

$$\bar{E} = kT^2 \left(\frac{\partial \ln Q}{\partial T} \right)_{N,V} \tag{2.17}$$

Non-mechanical variables such as entropy, S may also be related to Q:

$$S = \frac{\bar{E}}{T} + k \ln Q \tag{2.18}$$

Using Equations (2.17) and (2.18) and the fact that :

$$A = E - TS \tag{2.19}$$

Where A is the Helmholtz free energy and can be expressed in terms of Q:

$$A(N, V, T) = -kT \ln Q(N, V, T) \tag{2.20}$$

which is useful because A is the characteristic thermodynamic function for the independent variables N, V, T (those of the canonical ensemble). Equation (2.20) is an important link between thermodynamics and the canonical partition function because expressions for the thermodynamic properties entropy, S, pressure, P and

the chemical potential, μ may be derived from it. For example, differentiating with respect to temperature gives the entropy, S,

$$S = k \ln Q + kT \left(\frac{\partial \ln Q}{\partial T} \right)_{V,N} \tag{2.21}$$

The canonical ensemble is an example of one of the many possible ensembles that can be constructed. When the walls of the systems in the canonical ensemble are permeable to the transport of matter, we have a *grand canonical ensemble* which is a further generalisation of what has been described so far.

2.2.5 The Grand Canonical Ensemble

In a grand canonical ensemble, X systems have a constant volume V. The systems are open and therefore the walls are permeable to matter and energy and the number of molecules, N, are allowed to fluctuate between systems around some mean value $\bar{N}$.

The systems are placed in a large reservoir of molecules at temperature T until equilibrium is reached. At equilibrium the entire ensemble is isolated and referred to as a *supersystem*. Each system is characterised by the independent variables volume, V, temperature, T, and chemical potential, μ. The generalisation to non-constant numbers of molecules makes the grand canonical ensemble directly applicable to problems involving adsorption. It can be used to calculate average number density values for example in a surface pore of constant volume and temperature at a chemical potential value which can be related to a pressure value through the

virial equation of state (Section 4.3). In this way an adsorption isotherm can be constructed for a series of pressure values.

The number of systems in the ensemble that contain N molecules and are in the particular energy state $E_j(N,V)$ is denoted $n_j(N)$. All states associated with all possible distributions have equal probability of occurrence in the ensemble.

In order for a distribution to be acceptable it must satisfy the following 3 relations:

$$\sum_{j,N} n_j(N) = X \tag{2.22}$$

$$\sum_{j,N} n_j(N) E_j(N,V) = E_t \tag{2.23}$$

$$\sum_{j,N} n_j\,(N)\,N = N_t \tag{2.24}$$

Where X, E_t and N_t are the total number of systems in the ensemble, the total energy of the ensemble and the total number of molecules in the ensemble respectively and all 3 are constant. For a distribution, the number of possible states is:

$$W\,(\{n\}) = \frac{X!}{\prod_N \prod_j n_j(N)!} \tag{2.25}$$

The dominating distribution i.e. the most probable, is found by maximising (2.25) under the constraints in Equations (2.22) to (2.24) to give:

$$n_j^*(N) = Xe^{-\alpha}e^{-\beta E_j(N,V)}e^{-\gamma N} \tag{2.26}$$

The probability that any system, chosen at random contains N molecules in the j_{th} energy state with energy $E_j(N,V)$ is thus:

$$P_j(N) = \frac{e^{-\beta E_j(N,V)}e^{-\gamma N}}{\sum_{i,N'} e^{-\beta E_i\left(N',V\right)/kT}e^{-\gamma N'}} \tag{2.27}$$

The average energy may now be expressed as:

$$E \leftrightarrow \bar{E}\,(= E_t/X) = \sum_{j,N} P_j(N)E_j\,(N,V) \tag{2.28}$$

and the average number of molecules:

$$N \leftrightarrow \bar{N}\,(= N_t/X) = \sum_{j,N} P_j(N)N \tag{2.29}$$

To evaluate γ from Equation (2.27):

$$d\bar{E} = \sum_{j,N} E_j\,(N,V)\,dP_j\,(N) + \sum_{j,N} P_j\,(N)\,dE_j\,(N,V) \tag{2.30}$$

Substituting $E_j\,(N,V)$ from Equation (2.27):

$$d\bar{E} = -\frac{1}{\beta}\sum_{j,N}[\gamma N + \ln P_j\,(N) + \ln \Xi]dP_j\,(N) + \sum_{j,N} P_j\,(N)\,\frac{\partial E_j\,(N,V)}{\partial V}dV \tag{2.31}$$

Where

$$\Xi = \sum_{j,N} e^{-\beta E_j(N,V)}e^{-\gamma N} \tag{2.32}$$

The grand partition function, Ξ acts as a bridge between thermodynamics and statistical thermodynamics for open, isothermal systems.

Referring to Equation (2.29), Equation (2.31) becomes:

$$-\frac{1}{\beta}\, d[\sum_{j,N} P_j\,(N) \ln P_j\,(N)] = d\bar{E} + \bar{p}dV + \frac{\gamma}{\beta} d\bar{N} \tag{2.33}$$

and knowing

$$TdS = dE + pdV - \mu dN \tag{2.34}$$

Thus:

$$\mu \leftrightarrow \frac{\gamma}{\beta} \tag{2.35}$$

and

$$TdS \leftrightarrow \frac{1}{\beta} d[\sum_{j,N} P_j\,(N) \ln P_j\,(N)] \tag{2.36}$$

In terms of the entropy, S:

$$S \leftrightarrow \frac{1}{k} \sum_{j,N} P_j\,(N) \ln P_j\,(N) \tag{2.37}$$

and again:

$$\frac{1}{kT} \leftrightarrow \beta \tag{2.38}$$

and

$$\frac{\mu}{kT} \leftrightarrow -\gamma \tag{2.39}$$

Re-writing Equation (2.27):

$$P_j\left(N,V,T,\mu\right) = \frac{e^{-E_j(N,V)/kT}e^{N\mu/kT}}{\Xi\left(V,T,\mu\right)} \tag{2.40}$$

where

$$\Xi = \sum_{j,N} e^{-E_j(N,V)/kT}e^{N\mu/kT} \tag{2.41}$$

and

$$\Xi\left(V,T,\mu\right) = \sum_{N} Q\left(N,V,T\right)e^{N\mu/kT} \tag{2.42}$$

A grand ensemble is just a collection of canonical ensembles in thermal contact with each other, each characterised by N. Inserting Equation (2.27) into (2.37):

$$S = \frac{\bar{E}}{T} - \frac{\bar{N}\mu}{T} + k\ln\Xi = \frac{E}{T} - \frac{N\mu}{T} + \frac{pV}{T} \tag{2.43}$$

and hence

$$pV = kT\ln\Xi\left(V,T,\mu\right) \tag{2.44}$$

and pV is the thermodynamic characteristic function for the variables V, T and μ:

$$d\left(pV\right) = SdT + Nd\mu + pdV \tag{2.45}$$

Thermodynamic properties for an open, isothermal system as a function of V, T, and μ may now be derived from Equation (2.42) and Equation (2.45):

$$S = kT\left(\frac{\partial \ln \Xi}{\partial T}\right)_{V,\mu} + k \ln \Xi \tag{2.46}$$

$$N = kT\left(\frac{\partial \ln \Xi}{\partial \mu}\right)_{V,T} \tag{2.47}$$

$$p = kT\left(\frac{\partial \ln \Xi}{\partial V}\right)_{\mu,T} = kT\frac{\ln \Xi}{V} \tag{2.48}$$

Where S is the entropy, N is the number of molecules, and p is the pressure.

2.3 Density Functional Theory

2.3.1 A Theoretical Model For Adsorption

Density Functional Theory (DFT) is based on statistical mechanics and provides a theoretical model for adsorption. The version of DFT used here is different from the version of DFT applied to Electronic Structure for example which is also referred to as DFT. Detailed accounts of DFT applied to electronic systems are given elsewhere [23], [24].

DFT is an approximate theory which is used to simplify and solve the equations in statistical mechanics in contrast to molecular simulation which solves the equations of statistical mechanics numerically. DFT is used to calculate a profile of the density of adsorbate molecules, $\rho(r)$, for all locations within a pore, at thermal equilibrium.

The grand canonical variables, V, T, and μ describe the open, isothermal system; in this case a single pore. The system is open and in contact with the bulk adsorbate gas. Adsorbate molecules are represented by hard spheres. The density profile is important because once this is known other thermodynamic properties may be calculated. These include the adsorption isotherm which is of central importance in this thesis.

The grand potential or grand free energy, Ω, for such a system is defined by:

$$\Omega = A - \sum_{\alpha} \mu_{\alpha} N_{\alpha} \tag{2.49}$$

Where A is the Helmholtz free energy, μ is the chemical potential of component α and N_{α} is the number of molecules of component α. Ebner and Saam [51] and Yang et al [52] were among the first to apply density functional methods to classical fluids, and these approximate theories have become very popular.

The free energy, A, of inhomogeneous fluids, fluids which are confined between pore walls for example, can be expressed as a functional[4] of the density profile $\rho(r)$. This concept is the basis of density functional methods.

The exact differential of A is

$$dA = SdT - PdV + \gamma d\mathsf{S} + \sum_{\alpha} \mu_{\alpha} dN_{\alpha} \tag{2.50}$$

[4]A functional is a mapping of a function into a number. [A function is a mapping from one number or set of numbers into another]. For example, I is a functional of the function $x(t)$ in the interval (a,b) when it depends on all the values taken by $x(t)$ throughout the interval. e.g $I[x(t)] = \int_a^b x(t)dt$

Where S is the entropy, P is pressure, V is volume, γ is surface tension, and S is the surface area.

Using Equation (2.50) and differentiating (2.49) gives:

$$d\Omega = SdT - pdV + \gamma d\mathsf{S} - \sum_{\alpha} N_{\alpha} d\mu_{\alpha} \tag{2.51}$$

Using Euler's theorem [28] to solve for A and Ω we have:

$$A = -PV + \gamma\mathsf{S} + \sum_{\alpha} \mu_{\alpha} N_{\alpha} \tag{2.52}$$

and

$$\Omega = -PV + \gamma\mathsf{S} \tag{2.53}$$

For a homogeneous fluid:

$$\Omega = -PV \tag{2.54}$$

Expressing the grand free energy and Helmholtz free energy as functionals of the density profile, $\Omega[\rho(r)]$ and $A[\rho(r)]$, it can be shown that for a given $\rho(r)$ there is a unique value of Ω and A [40]. By varying $\rho(r)$ and finding its global minimum the equilibrium density profile of the system is found. The minimum values of Ω and A that correspond to the equilibrium density profile [40], [41] $\rho_{eq}(r)$ are called the *thermodynamic grand free energy* and the *intrinsic Helmholtz free energy* (the Helmholtz energy in the absence of an external field i.e. the pore walls).

The free energy functionals $\Omega[f]$ and $A[f]$, are defined as:

$$\Omega[f(r^N)] = Tr_{cl} f(r^N)\{U + V - \mu N + kT \ln f(r^N)\} \tag{2.55}$$

and

$$A[f(r^N)] = Tr_{cl} f(r^N)\{U + kT \ln f(r^N)\} \tag{2.56}$$

Where U is the total intermolecular potential energy, V is the potential energy due to an external field, in this case the pore walls, $f(r^N) = f(r_1, r_2 \cdots r_N)$ and represents the molecular N-body distribution function for a system which is not at equilibrium. Tr_{cl} is the classical trace:

$$Tr_{cl}(\cdots) = \sum_N \left(\frac{q_{qu}}{\Lambda_t^3}\right)^N \frac{1}{N!}(\cdots)\, dr_1, dr_2, \cdots dr_N \tag{2.57}$$

Where q_{qu} is the quantal part of the molecular partition function, Λ_t is the kinetic energy part of the molecular partition function, and r_i is the position of the centre of molecule i, and $Tr_{cl} f\left(r^N\right) = 1$.

At equilibrium $f_{eq}(r^N)$ is given by the grand canonical expression:

$$f_{eq}(r^N) = \frac{1}{\Xi}\, exp\{-\frac{1}{kT}(U + V - \mu N)\} \tag{2.58}$$

Where the grand partition function, Ξ is:

$$\Xi = Tr_{cl}\, exp\{-\frac{1}{kT}(U + V - \mu N)\} \tag{2.59}$$

The grand free energy functional given in Equation (2.55) can now be written as:

$$\Omega[f] = -kT \ln \Xi = \Omega \tag{2.60}$$

The intrinsic Helmholtz free energy given in Equation (2.56) in terms of the grand partition function is:

$$A[f] = -kT \ln \Xi + \mu < N >= A_i \tag{2.61}$$

Where $< N >$ is the average number of molecules in the system, μ is the chemical potential and A_i is the intrinsic Helmholtz free energy.

The grand potential functional, $\Omega[f]$ in terms of $A[f]$ is written as:

$$\Omega[f] = A[f] + \int dr f(r) v(r) - \mu \int dr f(r) \tag{2.62}$$

Where $v(r)$ is the external potential acting on a molecule i.

The one-body distribution function, $f(r)$ is normalised and is proportional to the probability density of finding a molecule at position r and is denoted as:

$$f(r_1) = \sum_N \left(\frac{q_{qu}}{\Lambda_t^3}\right)^N \frac{1}{(N-1)!} \int dr_2, dr_3 \cdots dr_N f(r_2, r_3 \cdots r_N) \tag{2.63}$$

In (2.55) and (2.56), Ω and A are treated as functionals of the full N-body distribution function, $f(r^N)$. As $f(r^N)$ is a functional of $f(r)$, $\Omega[f]$ and $A[f]$ can be taken to be functionals of the one-body distribution function $f(r)$. At equilibrium $f(r) = \rho_{eq}(r)$ (the number of molecules per unit volume at point r) and so $\Omega[f]$ becomes $\Omega[\rho(r)]$ and $A[f]$ becomes $A[\rho(r)]$.

Determining The Equilibrium Density Profile

At equilibrium Ω is a minimum and so differentiating Ω with respect to the density profile at constant external field $v(r)$ and (μ, V, T):

$$\left(\frac{\partial\Omega[\rho(r)]}{\partial\rho(r)}\right)_{\rho=\rho_{eq}} = 0 \tag{2.64}$$

According to Equation (2.60) and the fact that $\Omega[f]$ becomes $\Omega[\rho(r)]$ we can write:

$$\Omega[\rho(r)] = \Omega \tag{2.65}$$

The equilibrium intrinsic chemical potential, $\mu_i(r)$ (chemical potential in the absence of an external field) is defined by:

$$\mu_i(r) = \left(\frac{\delta A}{\delta\rho(r)}\right)_{\rho=\rho_{eq}} \tag{2.66}$$

and

$$\mu_i(r) + v(r) = \mu \tag{2.67}$$

Where μ is the chemical potential and consists of an external field contribution, v, and an intrinsic contribution μ_i. Referring to Equation (2.62) in order to obtain the grand potential an expression for A is required. With an expression for A, an iterative computational method minimises A to produce $\rho_{eq}(r)$.

The Helmholtz energy density $A_o[\rho(r)]$ is split into an ideal gas part and a residual or non-ideal part:

$$A_o = A_o^{id} + A_o^r \tag{2.68}$$

The ideal part, $A_o^{id}(r)$ depends only on the density $\rho(r)$ at the point r i.e. it is *local*. The residual part $A_o^r(r)$ depends on the density profile at all points r for the inhomogeneous fluid i.e. it is *non-local*. It is assumed that the residual Helmholtz free energy density of the inhomogeneous fluid can be equated to that for a homogeneous fluid (i.e. they possess the same potential U_o) at a given smoothed or 'non-local' density $\bar{\rho}(r)$, and thus we have:

$$A_o[\rho(r)] = \int dr A_o^{id}[\rho(r)] + \int dr \rho(r) \psi_o^{r,un}[\bar{\rho}(r)] \tag{2.69}$$

Where $\psi_o^{r,un}$ is the Helmholtz energy per molecule for a uniform fluid. The main approximation in this form of density functional theory, as shown in Equation (2.69) is the replacement of the residual Helmholtz free energy for an inhomogeneous fluid by that for a uniform fluid. The smoothed density $\bar{\rho}(r)$ is taken to be the average of the local densities at points r' near to r, the centre of interest and is defined as:

$$\bar{\rho}(r) = \int dr' \rho(r') w(|r - r'|) \tag{2.70}$$

Where $w(r)$ is a normalized isotropic weighting function. It is also assumed that $\psi_o^{r,un}$ is equated to that for a fluid of hard spheres of diameter σ, and $\psi_o^{r,un}$ can then be calculated from the Carnahan-Starling equation [39] which is an accurate equation of state for uniform hard spheres, with $\bar{\rho}(r)$ of Equation (2.70) used for the density.

Choosing A Weighting Function

To calculate the smoothed density in Equation (2.70), a form for the weighting function $w(r)$ is required which describes the structure and thermodynamics of the uniform hard sphere fluid, i.e. the weighting function must give a good description of the two-body direct correlation function, $(C_o(r_1 r_2) = C_o(r))$ of the uniform hard sphere fluid. A second functional derivative of the residual Helmholtz energy functional [40] describes the structure and thermodynamics of the fluid and is given by:

$$C_o(r_1, r_2) = -\frac{1}{kT} \frac{\delta^2 A_o^r}{\delta\rho(r_1)\,\delta\rho(r_2)} \tag{2.71}$$

A_o^r is the last term on the right hand side of Equation (2.69).

The choice of the weighting function $w(r)$ dictates which type of density functional theory is used, and several types have been used to study fluids in pores [53], [54]. For example, if we let

$$\omega(r) = \delta(r) \tag{2.72}$$

Where $\delta(r)$ is the Dirac delta function, the smoothed density of Equation (2.70) becomes the local density $\rho(r)$. This is called the local density functional theory, and is successful for fluid-fluid interfaces [41] however it gives poor results for pore-fluid interfaces due to the pore walls causing large fluctuations in the densities.

In this thesis, Tarazona's theory to second order [42] is used where it is assumed that $w(r)$ has a power series expansion in the smoothed density.

$$w(r^{'};\bar{\rho}(r)) = w_o(r^{'}) + w_1(r^{'})\bar{\rho} + w_2(r^{'})\bar{\rho}(r)^2 + \cdots \tag{2.73}$$

Where $w_o(r^{'})$, $w_1(r^{'})$ and $w_2(r^{'})$ are the weighting functions [42]. Substitution of Equation (2.73) into (2.70) we obtain an integral equation for $\bar{\rho}(r)$:

$$\bar{\rho}(r) = \bar{\rho}_o(r) + \bar{\rho}_1(r)\bar{\rho}(r) + \bar{\rho}_2(r)(\bar{\rho}(r))^2 + \cdots \tag{2.74}$$

Where

$$\bar{\rho}_i(r) = \int dr^{'}\rho(r^{'})w_i(|r - r^{'}|) \quad i = 0, 1, 2 \tag{2.75}$$

As the weighting factor depends on the smoothed density it must be calculated at each point in the pore.

$C_o(r)$ for the uniform hard sphere fluid is obtained from Equation (2.71) where A_o^r is evaluated at the smoothed density in Equation (2.74) using the Carnahan-Starling equation [39] to calculate A_o^r.

Tarazona's theory to second order was chosen to represent the weighting function as it gives excellent agreement with molecular simulation results for the density profile [42] and it has also been successful in predicting the solid-fluid transition for a hard-sphere fluid in contact with a wall [42]. The advantages of approximate theories such as DFT over full molecular simulation are the speed and ease of the calculation. However, the Tarazona DFT becomes difficult to use when applied to more complex systems such as mixtures as there is some ambiguity in the definition of the weighting functions [20], or for cylindrical pores of diameter less than 4σ as

the theory does not give the one dimensional limit correctly [42].

Providing the runs are long enough in molecular simulations to properly describe the real system, exact solutions should be given for the model [43] [44].

This thesis will focus on the application of DFT to adsorption in pores of restricted geometry, the determination of the pore size distributions of porous carbons at 293K and 77K for different adsorbates and their adsorptive selectivity in mixtures.

In order to apply DFT to a real material a model describing the porous carbon surface, the adsorbate molecules and their interaction with each other and the adsorbent is required.

2.4 Modelling Adsorption

The DFT method assumes that the real material's heterogeneity is approximated by a distribution of pore sizes and is thus treated as an effective porous material. Thus any heterogeneity due to variations in pore shape, chemical groups on the surface, pore networking and blocking effects are not accounted for.

Porous carbons are distinct from one another in the number, size and distribution of pores constituting their structure. According to Brunauer, Emmett and Teller's classification [29], [30], the shape of a material's adsorption isotherm gives some indication of the physical processes that are occurring and the type of porosity the material possesses. Establishing the distribution of pores of a given width (i.e. the pore size distribution (PSD)) provides a method of characterisation of materials.

In the past, pore size distributions have been determined from classical methods

such as the Kelvin equation (Chapter 3), and the Horvath and Kawazoe model (HK) (Chapter 3) [34]. However, Kelvin related models fail for pore widths less than 70-80 $\mathring{A}$ for carbons as the equation does not take into account the presence of a pre-condensation film on the pore walls [3]. Unlike the Kelvin equation, the Horvath and Kawazoe method accounts for the strong solid-fluid attractive forces in micropores. However, the HK method does not take into account pore wetting and assumes a pore is completely empty if it is below its filling pressure or completely full if it is above its filling pressure, and therefore gives poor results for mesopore pore size distributions.

The DFT method of calculating isotherms can predict the full isotherm and not just the capillary condensation pressure, it can also be used at supercritical pressures where a phase change occurs and is accurate for small pores. These are all areas where classical methods fail.

DFT has been applied to the problem of obtaining PSD's [45], [46], [47], [48], [49], [50] and can be applied to pores of widths which tend to $0\mathring{A}$.

2.4.1 Determination of a Porous Carbon's Pore Size Distribution

In this thesis the following assumptions are made to model the adsorption process. We assume; (1) that the surface of a porous carbon consists of an array of pores of uniform width, H, which are slit-like in geometry as first proposed by Everett [33] (and approximates typical lamellar pore geometries as observed in activated carbon

fibres [1]), each of which (2) fill according to a local isotherm, $\rho(P,H)$ calculated from DFT (Section 2.3), where ρ, is the uptake of gas at an equilibrium gas-phase pressure, P, in a pore of width H, (3) pore junction effects are neglected because the ratio of pore length to pore width is large, and (4) the surface is devoid of hetero-atoms, functional groups, and defects (i.e. the surface is uncorrugated and chemically homogeneous), and finally (5) the size of the pores is small compared to the total adsorbing surface area of the material. The experimental adsorption of gases on porous carbons, $N(P)$, is measured volumetrically (Chapter 3), and is modelled by the generalised adsorption isotherm [22]:

$$N(P) = \int_{H_{min}}^{H_{max}} \rho(P,H) f(H) dH \tag{2.76}$$

This adsorption integral is a Fredholm equation of the first kind [31]. The experimental isotherm $N(P)$ is called the 'driving term' and the local isotherm, $\rho(P,H)$ is the 'kernel' of the Fredholm equation and is calculated from DFT (Section 2.3).

Given $\rho(P,H)$ and $N(P)$, solving the adsorption integral for $f(H)$ is ill-posed and small perturbations in $N(P)$ (i.e. experimental errors) can yield large perturbations in $f(H)$. A gamma distribution represents the function $f(H)$. This is a multi-modal function and is given by the expression [45]:

$$f(H) = \sum_{i=1}^{m} \frac{\alpha_i(\gamma_i H)^{\beta_i}}{\Gamma(\beta_i)H} exp(-\gamma_i H) \tag{2.77}$$

Where m is the number of modes in the distribution, α_i, β_i, and γ_i are adjustable parameters that are related to the amplitude, mean and variance of mode i respec-

tively. H is the pore width. The number of modes in Equation (2.77) is equal to the number of inflection points in the experimental adsorption isotherm. Initial starting values are assigned to the parameters α, β and γ which provide the additional, necessary constraint on $f(H)$. The solution that is considered to be $f(H)$ is the one that gives the best fit to the experimentally determined total isotherm, and in this work it is obtained numerically by minimising the sum of the square of the differences r, between the experimental and theoretical isotherms:

$$r = \frac{1}{n_P} \sum_{i=1}^{n_P} \Big[\sum_{j=1}^{n_H} \rho(P_i, H_j) f(H_j) \Delta H_j - N(P_i) \Big]^2 \tag{2.78}$$

Where r is the mean square error per fitted point, n_P is the number of experimental points, and n_H is the total number of pore widths.

2.4.2 Model Description

In order to calculate the theoretical uptake of an adsorbate in a pore of width H (i.e. the local isotherm $\rho(P, H)$ of Equation (2.76)) a model is required.

2.4.3 The Adsorbent Model

A porous carbon is envisaged as an array of individual pores which [33] are slit-like in geometry. As illustrated in Fig (2.3) an individual pore is modelled as the space between two parallel graphite planes which are assumed to be infinite in extent and represent the pore walls.

The graphitic planes are composed of carbon atoms and the distance between

the nuclei of the surface carbon atoms of the 2 opposing planes is defined as the physical pore width, H_{phys} or H and is used throughout this work.

Each wall of the pore consists of graphitic planes which are separated by a uniform distance $\Delta = 0.335$nm. The model graphite surface has a density, $\rho_s = 0.114\mathring{A}^{-3}$ and is assumed to be void of any surface defects, hetero-atoms or functional groups. In other words it is uncorrugated and chemically homogeneous.

The Adsorbate Model

A simplified representation of the potential energy of interaction between molecules is the Lennard-Jones 12-6 potential (LJ(12,6)) and is expressed as:

$$U(r) = 4\epsilon\left[\left(\frac{\sigma}{r}\right)^{12} - \left(\frac{\sigma}{r}\right)^{6}\right] \tag{2.79}$$

Where $U(r)$ is the potential energy of interaction as a function of separation distance, r, while ϵ is the depth of the well, and σ is the intermolecular diameter of the adsorbate molecule or the 'collision diameter'. The LJ(12-6) potential is drawn in Fig (2.4):

Figure 2.3: *Model of a Single Carbon Slit Pore.*

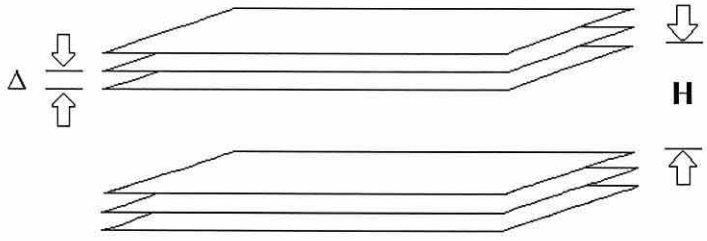

The Adsorbate-Adsorbate Potential

Following the LJ(12,6), potential the fluid-fluid interaction, ϕ_{ff} is given by:

$$\phi_{ff}(r) = 4\epsilon_{ff}\left[\left(\frac{\sigma_{ff}}{r}\right)^{12} - \left(\frac{\sigma_{ff}}{r}\right)^{6}\right] \tag{2.80}$$

Where r is the separation distance, ϵ_{ff} is the parameter for the bulk fluid-fluid well-depth, and σ_{ff} is the parameter for the molecular diameter of the adsorbate molecule. ϵ_{ff} and σ_{ff} are both fitted parameters (see Chapter 4).

The Adsorbate-Adsorbent Potential

The Steele 10-4-3 potential is the basis for the adsorbate-adsorbent interaction potential, ϕ_{sf} i.e for the adsorbate molecule interacting with a single graphite plane.

Figure 2.4: *Diagram of the LJ(12,6) Potential.*

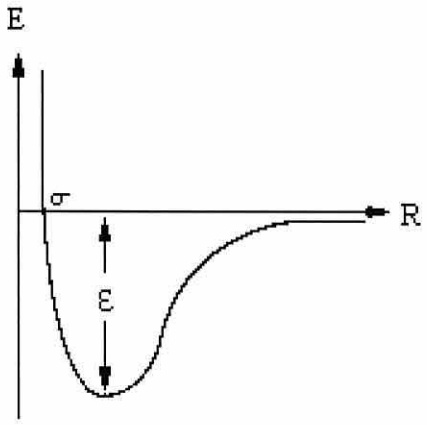

$$\phi_{sf}(z) = \epsilon_w \left[\frac{2}{5} \left(\frac{\sigma_{sf}}{z} \right)^{10} - \left(\frac{\sigma_{sf}}{z} \right)^{4} - \frac{{\sigma_{sf}}^4}{3\Delta \left(z + 0.61\Delta \right)^3} \right] \tag{2.81}$$

Where z is the distance between the nuclei of the adsorbate molecule and the nuclei of the atoms in the outer layer of the solid adsorbent, σ_{sf} is the effective adsorbate-adsorbent intermolecular diameter, and ϵ_{sf} is the Lennard-Jones well-depth of the adsorbate-adsorbent atom site interaction. The parameters σ_{sf} and ϵ_{sf} were determined using the Lorentz-Berthelot combination rules [Appendix A].

The Lennard-Jones potential between one adsorbate molecule and each carbon atom of the individual graphite planes is integrated to give the 10-4-3 Steele potential, where the '10' and '4' terms represent the repulsive and attractive interaction respectively, and the '3' term is a result of the summation of the attractive part of the potential over the remaining layers of the adsorbent. The parameter ϵ_w is given by:

$$\epsilon_w = 2\pi\epsilon_{sf}\rho_s\sigma_{sf}^2\Delta \tag{2.82}$$

Where ρ_s is the graphitic density, σ_{sf} is the effective adsorbate-adsorbent intermolecular diameter, and Δ is the distance between 2 planes of graphite in a single slab. The value of ϵ_w is obtained from a fitting procedure described in Chapter 4. As we are dealing with a slit-pore, the adsorbate molecule interacts with 2 graphite planes, and so the overall potential, V_{ext} is expressed as:

$$V_{ext}(z) = \phi_{sf}(z) + \phi_{sf}(H - z) \tag{2.83}$$

Where H is the physical pore width and ϕ_{sf} is the adsorbate-adsorbent interaction potential.

Now the interaction potentials for the adsorbate-adsorbate and adsorbate-adsorbent interactions are defined, statistical mechanics is applied using the non-local form of DFT (Section 2.3) to obtain the local adsorption isotherms $\rho(P, H)$ for individual slit-shaped pores of size H. The calculation is for a specified temperature, T and pressure P. The pressure P is related to the chemical potential, μ through the *virial equation of state* (Section 4.3).

The system (a pore) under study is thereafter described by the Grand Canonical Ensemble (Section 2.2.5). In order to calculate an adsorption isotherm non-local DFT is applied to calculate the equilibrium density, ρ at a series of pressure values for the same pore of volume, V (specified by the pore width, H) and temperature, T. Once a series of isotherms has been calculated for a particular gas adsorbate, r of Equation (2.78) is minimised and thus the PSD is determined.

Chapter 3

Experimental Adsorption Isotherms

3.1 Introduction

This chapter describes the method of measuring the experimental isotherm data, $N(P)$, first introduced in Chapter 2 in Equation (2.76). The experimental isotherm data is required in order to solve the adsorption integral in Equation (2.76) and thus determine the pore size distribution of a given microporous carbon. The surface area of the material may also be calculated (see Section 3.1.5) once reliable experimental data have been attained. A value for the surface area is important where non-porous or 'reference' materials are concerned in testing the validity of the experimental method and also in determining the values of the interaction parameters which are to be used in calculating the theoretical local isotherms, $\rho(P, H)$, (Chapter 4), also to be used in Equation (2.76).

A description of the experimental equipment and method of measuring the amount of gas adsorbed by a known mass of sample at constant temperature is presented. This is followed by a review of methods which can be applied to the experimental isotherm data to determine pore surface areas and pore size distributions. A comparison of the pore volumes and pore size distributions determined from the numerical method outlined in Section 2.4 for different adsorbates at 77K and 293K is discussed in Chapter 5.

The experimental adsorption isotherms were measured on an Omnisorp 100 series instrument [58], a schematic diagram of the instrument is shown in (Fig 3.1).

Figure 3.1: *A Schematic Diagram of the Omnisorp 100 Machine.*

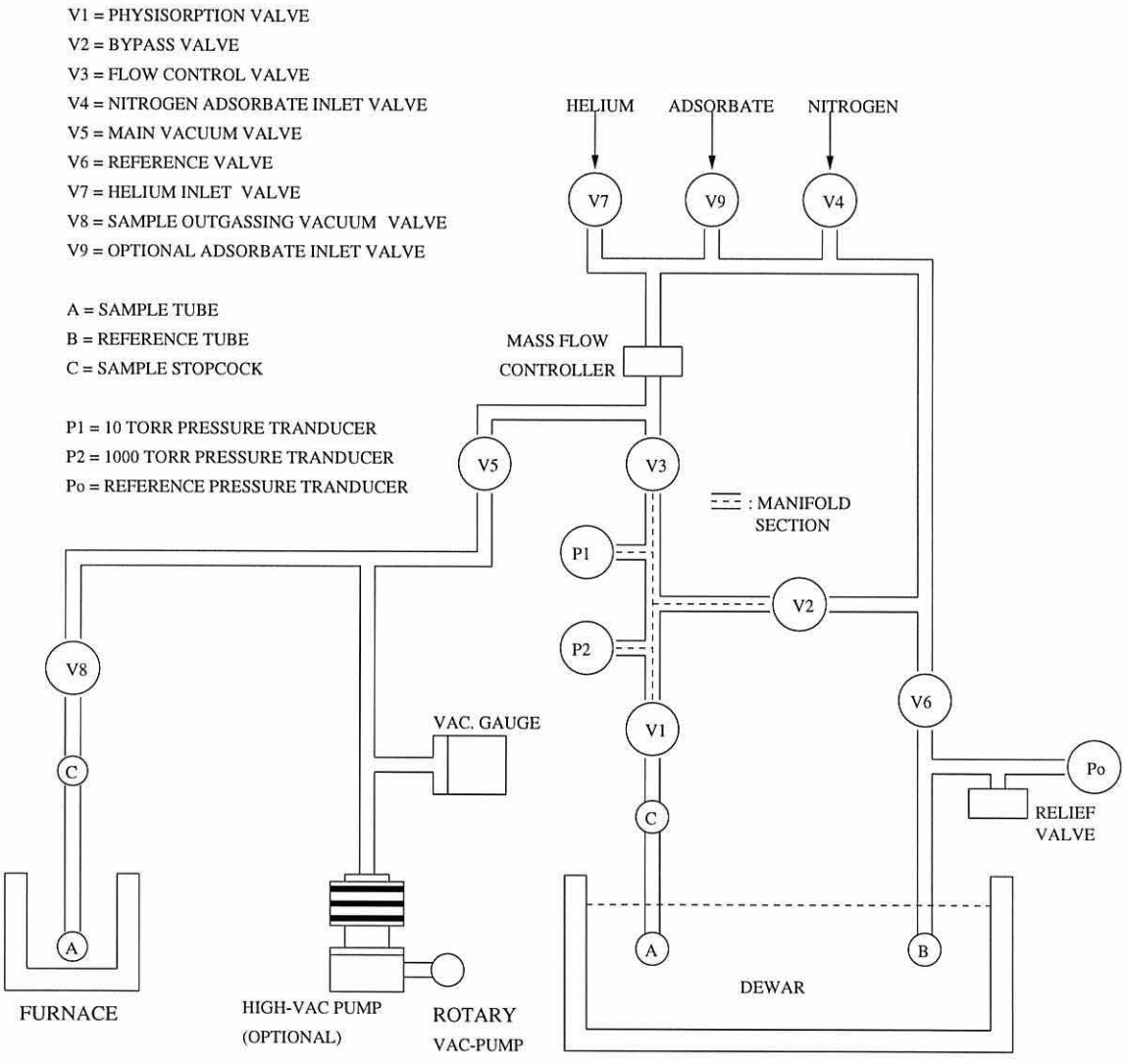

3.1.1 The Omnisorp 100 Instrument

Referring to Fig (3.1), the main features of the model 100 are: the sample port (sample tube connected to V8 via the sample stopcock) which is used for the preparation of a sample prior to measurement, the furnace which heats the sample, the reference port (reference tube B connected to V6) from which the saturation vapour pressure of the adsorptive may be calculated, and the measurement port (sample tube A connected to V1 via the sample stopcock) which measures the physisorption data. The furnace and its sample port make up the 'out-gassing section'. The temperature of the furnace can be set up to 450^oC.

The valve which isolates the sample out-gassing vacuum is labelled V8. The vacuum valve (V5) is the main vacuum isolation valve for the manifold. The manifold is a section of the machine located between valves 1, 2 and 3 (see Fig 3.1) and is used to 'dose' the sample with gas during a measurement. This involves letting a known volume of gas (the manifold has a calibrated volume) at a series of stable pressure readings enter the sample tube and thus 'dose' the sample with gas. The manifold is maintained at a temperature of $40^oC \pm 0.1^oC$. The reference valve (V6) isolates the reference pressure tube from the measurement manifold. Valve 1 (V1) is the physisorption valve. It isolates the sample tube from the rest of the instrument. V1 is only ever opened just before the sample measurement is about to begin i.e. once the manifold and upper sample tube spaces have been evacuated to a pressure value equal to that achieved during the out-gassing procedure.

The gas dosing occurs through the flow control valve (V3), and the adsorbate

admittance valves are V4 for nitrogen, and V9 for an optional adsorbate gas. The helium gas inlet, which is used for the dead space helium calibration (Section 3.1.3) is labelled V7. The bypass valve (V2) supplies a nonrestricted path from the measurement manifold to the gas inlet valves (helium and adsorbates).

Automatic operation of the Omnisorp 100 instrument and data acquisition is achieved by means of a connected IBM computer. Two interface cables connect the instrument to the computer; one is used for process control, the second connects the pressure transducers to the data acquisition system.

3.1.2 Preparation

A sample tube is cleaned in an ultra-sonic bath with water and detergent, and rinsed first with distilled water and then with isopropyl alcohol (IPA). The sample tube is then placed on the out-gassing port i.e. in the furnace and evacuated until completely dry by opening V8.

Out-gassing Procedure

When dry, the mass of the sample tube is recorded on a four decimal place balance. The sample is then added to the tube, and the new mass of the sample tube with sample is recorded. The sample tube is connected to the sample stopcock (C) which is then closed, and then the sample stopcock is connected to the out-gassing port. The out-gassing vacuum valve (V8) is opened and the sample stopcock is slowly opened.

The temperature of the furnace is then set to the required out-gassing temper-

ature, and when the furnace has reached this temperature the time is recorded as the start of the out-gassing procedure. The out-gassing procedure allows any physisorbed molecules on the sample to be evacuated. After the allotted time for out-gassing, the value on the vacuum gauge is recorded, the sample stopcock is closed and the vacuum system is isolated by closing V8. The sample tube and connecting sample stopcock which is closed are removed from the furnace and allowed to cool to room temperature.

Experiments carried out at 77K are achieved by filling the dewar (Fig 3.1) with liquid nitrogen to a level of approximately 2 inches below the top of the dewar. In order to carry out an experiment at room temperature the dewar is filled with water and allowed to equilibrate with the temperature of the room. The reference tube (B) is then connected to the reference port and is evacuated for approximately 30 minutes by opening the main vacuum (V5), bypass (V2), flow control (V3) and reference (V6) valves.

Measuring the Saturation Vapour Pressure

The appropriate adsorbate valve (either V4 or V9), the bypass valve (V2), and flow control valve (V3) are all opened. The reference tube is then filled with the gas adsorbate in order to measure its saturation vapour pressure. The reading for the pressure in the manifold is monitored and when the reading is sufficiently high i.e. higher than the adsorbate's expected P_o value calculated from an equation of state [75] the appropriate adsorbate valve (V4 or V9) is closed and the reference valve (V6) is opened. After a few seconds the manifold pressure drops as the adsorbate expands

into the reference tube and then the reference valve (V6) is closed. This procedure is repeated several times until a stable reading of the saturation vapour pressure, P_o, of the adsorbate is reached whereby liquid adsorbate is produced in the reference tube. For example, nitrogen as an adsorbate gives a P_o value of approximately 780 mmHg, this value is of course sensitive to the atmospheric pressure (as atmospheric pressure decreases with height) and therefore instrument altitude above sea level.

The adsorbate (V4) and reference (V6) valves are closed, and the manifold is evacuated by opening the vacuum (V5), flow control (V3), and bypass (V2) valves. The manifold is maintained to within 0.1°C of 40°C.

The sample tube (containing the sample) which is now at room temperature is transferred to the measurement port, by lowering it into the dewar and connecting it to the sample port. The sample stopcock remains closed while the volume above is evacuated by opening the sample valve (V1). When the maximum achievable vacuum has been obtained (after about 20 minutes) all valves are closed and the sample stopcock is opened.

3.1.3 Measuring An Adsorption Isotherm

The Static Flow Method which is used to measure adsorption isotherms is preceeded by the helium calibration otherwise known as the determination of 'dead space volume'.

Calculating The Dead Space Volume

Helium is assumed not to adsorb to any appreciable extent by the sample, sample tube or manifold. High purity helium gas (99.99 per cent by volume) is therefore used to calculate the 'dead space' volume of the system i.e. the volume of the sample tube. Helium is allowed into the calibrated manifold by opening V7, V2 and V3 and when consecutive pressure readings in the manifold, taken at 5 minute intervals agree to within 0.1 Torr, the pressure is taken to be at equilibrium and is recorded as $Ph1(I)$ (units of mmHg).

The sample valve (V1) is opened and helium is allowed to expand from the manifold into the sample tube. Once the new pressure has equilibrated it is recorded $Ps(I)$ (mmHg), V1 is closed, and the equilibrium pressure in the manifold is re-measured and recorded as $Ph2(1)$ (mmHg). Repeating the above cycle, when four or more sets of data have been recorded, the dead space volume, V_h (m^3) is calculated as follows:

$$V_h\,(1) = \left(\frac{273.2}{760}\right) \text{x} \left(\frac{V_m}{T_m + 273.2}\right) \text{ x } Ph1\,(1) \quad 1st\ Point \tag{3.1}$$

$$V_h\,(2) = V_h\,(1) + \left(\frac{273}{760}\right) \text{ x } \left(\frac{V_m}{T_m + 273.2}\right) \text{ x } [Ph1\,(2) - Ph2\,(1)]\ 2nd\ Point \tag{3.2}$$

Repeating the calculation for all data points, the general equation is:

$$V_h\,(I) = V_h\,(I-1) + \left(\frac{273.2}{760}\right) \text{ x } \left(\frac{V_h}{T_m + 273.2}\right) \text{ x } [Ph2\,(I) - Ph2\,(I-1)] \tag{3.3}$$

Where $V_h(I)$ is the volume of helium in the system, V_m is the volume of the manifold (cm^3) [58], and T_m is the temperature of the manifold (^oC). The temperature of the manifold is kept constant ($40^oC \pm 0.1^oC$) and therefore a constant called the volume factor V_f, may replace part of the general equation in (3.3).

$$V_f = \frac{273.2}{760} \text{ x } \left(\frac{V_m}{273.2 + T_m}\right) \tag{3.4}$$

The volume factor is calculated during the calibration of the manifold volume [58]. Therefore, substituting Equation (3.4) into Equations (3.1 through to 3.3) the values of V_h are calculated as follows:

$$V_h\,(1) = V_f \text{ x } Ph1\,(1) \tag{3.5}$$

$$V_h\,(2) = V_h\,(1) + V_f \text{ x } (Ph1\,(2) - Ph2\,(1)) \tag{3.6}$$

$$V_h\,(I) = V_h\,(I-1) + V_f \text{ x } (PhI\,(I) - Ph2\,(I-1)) \tag{3.7}$$

The volume of helium in the system $V_h(I)$ is equal to the volume of the sample tube and is calculated from the linear regression of $V_h(I)$ and $Ph2(I)$ to give:

$$V_h(I) = \frac{a+b}{Ph2\,(I)} \tag{3.8}$$

Where a is the intercept, and b is the slope. The manifold and sample holders are then evacuated and the adsorption experiment may begin.

3.1.4 Static Flow Method

In the static flow method the mass flow controller (MFC) Fig (3.1) doses the calibrated manifold with adsorbate. The adsorbate dose pressure is defined by the user. When the required manifold pressure has been reached and is stable, the MFC is switched off and the pressure equilibrates within the manifold. This pressure value is recorded $Pm1(I)$. The manifold volume is calculated from the ideal gas law [58].

The sample is then subjected to the known volume of equilibrated gas in the manifold at that pressure. The pressure is allowed to equilibrate in the sample tube. The pressure in the sample tube is measured and recorded as $Pm2(I)$, (mmHg) and the sample valve (V1) is closed. This cycle is repeated until the sample pressure equals the adsorption cut-off pressure which is programmed by the user at the start of the experiment. The adsorption cut-off pressure determines the extent of the recorded adsorption isotherm and is usually expressed as the ratio between the sample pressure and saturation vapour pressure and is therefore dimensionless.

The volume of gas adsorbed by the sample, V_{ads}, is calculated by subtracting the deadspace volume (given by the linear regression of the helium data) from the total volume, V_t:

$$V_{ads}(I) = V_t(I) - b \text{ x } (Ph2(I) - a) \tag{3.9}$$

Where the total volume $V_t(1)$ for each point along the isotherm is calculated using the volume factor, V_f:

$$V_t(1) = V_f \text{ x } Pm1(1) \tag{3.10}$$

$$V_t(2) = V_f \text{ x } (Pm1(2) - Pm2(1)) + V_t(1) \tag{3.11}$$

$$V_t(I) = V_f \text{ x } (P_{m1}(I) - P_{m2}(I-1)) + V_t(I+1) \tag{3.12}$$

Plotting the volume adsorbed divided by the dry sample weight, W against the adsorbate pressure $P_{m2}(I)$ gives an adsorption isotherm, $N(P)$.

3.1.5 Determination of The Surface Area

This section describes the method of calculating the surface area from adsorption isotherm data.

Brunauer, Emmett and Teller extended the Langmuir mechanism of adsorption [59] whereby the surface of the solid was regarded as an array of adsorption sites of uniform energy each capable of adsorbing one molecule i.e. adsorption was restricted to a monolayer. Brunauer, Emmett and Teller assumed [30] that molecules adsorbed locally in the first layer act as sites for molecules in second and higher levels and that layers above the first have evaporation and condensation properties similar to that of the liquid adsorptive. Type II isotherms describe unrestricted multilayer formation whereas Type IV isotherms describe restricted multilayer formation.

The surface area of the sample is calculated by applying the BET equation (Brunaeur, Emmett and Teller [30]) to the experimental adsorption isotherm data.

This is a widely used isotherm that deals with unrestricted multilayer adsorption:

$$\frac{P}{V\,(P_o - P)} = \frac{1}{V_m C} + \frac{C-1}{V_m C} \cdot \frac{P}{P_o} \tag{3.13}$$

Where P is the sample pressure, P_o is the saturation vapour pressure, V_m is the volume of the monolayer and V is the volume adsorbed. C is a constant and is related exponentially to the enthalpy of first layer adsorption:

$$C = e^{(E_1 - L)/RT} \tag{3.14}$$

Where E_1 is the heat of adsorption in the first layer, L is the latent heat of condensation, R is the ideal gas constant and T is the temperature. It follows that plotting $P/V(P_o - P)$ against P/P_o gives a straight line with a slope equal to $C - 1/V_m C$ and an intercept $1/V_m C$, combining the results, C and V_m can be found.

The linearity of the BET plot is restricted to a part of the isotherm [57] usually over the range P/P_o 0.05 to 0.3. Where active carbons are concerned the range is $P/P_o < 0.1$. Brunauer, Emmett and Teller state [30] that close agreement is found between the monolayer volume, V_m and the amount adsorbed at point B (monolayer formation point) for Type II and IV isotherms where $C > 100$. When the C value is < 20, point B cannot be located [57] and thus the reliability of the value of V_m is questionable. The BET surface area is then calculated as:

$$SA_{BET} = V_m \text{ x } N \text{ x } A_m \tag{3.15}$$

Where SA_{BET} is the surface area of the sample ($m^2.gm^{-1}$), V_m is the volume of

the monolayer (cm^3), N is Avogadro's number (mol^{-1}), and A_m is the cross-sectional area of an adsorbate molecule ($\mathring{A}^2$). Nitrogen at 77K has been shown to be the most suitable gas for surface area determination [57], [60], [73] with the value of $A_m = 16.2\mathring{A}^2$.

The importance of the surface area of non-porous or reference carbons in determining a microporous carbon's pore size distribution will be discussed in Chapter 4. Other methods have been developed to determine the pore size distributions of microporous carbons and these are described below.

3.2 Horvath and Kawazoe Method Of Determining Micropore Size

In 1976, Everett and Powl showed that the potential energy of interaction, ϵ, between one adsorbate molecule and 2 parallel lattice planes (that can be thought of as pore walls) whose nuclei are separated by a distance L can be expressed via the Lennard-Jones potential:

$$\epsilon = K\epsilon^* \left[-\left(\frac{\sigma}{r}\right)^4 + \left(\frac{\sigma}{r}\right)^{10} - \left(\frac{\sigma}{L-r}\right)^4 + \left(\frac{\sigma}{L-r}\right)^{10} \right] \tag{3.16}$$

Where

$$\sigma = \left(\frac{2}{5}\right)^{\frac{1}{6}} \sigma_{gs} \tag{3.17}$$

and $K = 3.07$, and σ_{gs} is the mean arithmetic value of the adsorbate-adsorbent

diameter, and r is the displacement of a molecule from a plane of surface nuclei. When more than one adsorbate molecule is concerned, ϵ^* is expressed as:

$$\epsilon^* = \frac{3}{10}\left[\frac{N_a A_a + N_A A_A}{\sigma_{gs}^4}\right] \tag{3.18}$$

Where

$$A_a = \frac{6mc^2\alpha_s\alpha_A}{\left(\frac{\alpha_s}{X_s}\right) + \left(\frac{\alpha_A}{X_A}\right)} \tag{3.19}$$

and

$$A_A = \frac{3}{2}\left(mc^2\alpha_A X_A\right) \tag{3.20}$$

A_a and A_A are called the Kirkwood-Muller dispersion constants. m is the mass of an electron, c is the speed of light, α_A is the polarisability of adsorbate (cm^3), α_s is the polarisability of substrate (cm^3), X_A is the magnetic susceptibility of adsorbate (cm^3), and X_s is the magnetic susceptibility of substrate (cm^3).

Using Equations (3.16) and (3.18) the potential function for a slit pore full of adsorbate molecules is written as:

$$\epsilon(r) = \frac{N_A A_A + N_a A_a}{2\sigma^4}\left[-\left(\frac{\sigma}{r}\right)^4 + \left(\frac{\sigma}{r}\right)^{10} - \left(\frac{\sigma}{L-r}\right)^4 + \left(\frac{\sigma}{L-r}\right)^{10}\right] \tag{3.21}$$

Horvath and Kawazoe equated the free energy of adsorption to the net energy of interaction between the layers to give:

$$RT\ln\left(\frac{P}{P_o}\right) = N_{Av}\frac{\int_{\sigma_{gs}}^{L-\sigma_{gs}} \epsilon(r)\ dr}{\int_{\sigma_{gs}}^{L-\sigma_{gs}} dr} \tag{3.22}$$

Substituting Equation (3.21) into Equation (3.22) Horvath and Kawazoe showed how the adsorption pressure can be correlated to the effective pore diameter of a slit-like micropore:

$$R_g T \ln\left(\frac{P}{P_o}\right) = N_{Av}\frac{N_A A_A + N_s A_s}{\sigma^4\left(L - 2\sigma_{gs}\right)}\left[\frac{\sigma^4}{3\left(L-\sigma_{gs}\right)^3} - \frac{\sigma^{10}}{9\left(L-\sigma_{gs}\right)^9} - \frac{\sigma^4}{3\sigma_{gs}^3} + \frac{\sigma^{10}}{9\sigma_{gs}^9}\right] \tag{3.23}$$

The model that the Horvath and Kawazoe model is based on is shown in Fig (3.2).

Figure 3.2: *Diagram of Horvath and Kawazoe Model.*

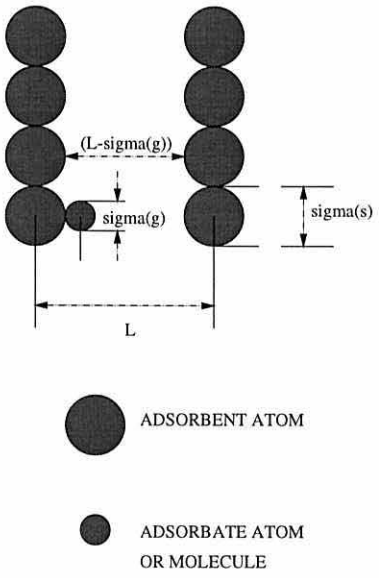

Where L is the distance between the nuclei of 2 pore walls, σ_g is the diameter of an adsorbate molecule, σ_s is the diameter of an adsorbent molecule.

If we let W_o represent the maximum volume of gas adsorbed and assign its value to the corresponding highest experimental pressure obtained we can correlate the volume of gas adsorbed, W, to the effective pore diameter (L- σ_g);

$$\frac{W}{W_o} = f(L - \sigma_g) \tag{3.24}$$

A plot of the normalised volume adsorbed (W/W_o) against the effective pore diameter, ($L - \sigma_g$) gives in essence the effective pore size distribution. The Horvath and Kawazoe method has been extended to cylindrical pores by Saito and Foley [35] and has also been extended by Venaro and Chiou [66] and Seifert and Emig [36] [37] to zeolites and other oxide-type microporous materials.

3.3 The t-plot Method

The t-plot method was developed by Lippens and deBoer [62] to detect the type of porosity present in carbons. This method is based upon the concept of a 'standard isotherm' of nitrogen at 77K on a non-porous material such as Vulcan. A plot of the amount of nitrogen adsorbed against the statistical thickness, t, of the adsorbed layers is linear and passes through the origin (A, Fig 3.3).

The adsorbate thickness, t, is derived from the Harkins and Jura adsorption equation [83] and standard isotherm data:

$$t = [\frac{13.99}{log\frac{P_o}{P} + 0.34}]^{\frac{1}{2}} \tag{3.25}$$

Where P is the sample pressure and P_o is the saturation vapour pressure of the adsorbate.

The presence of micro and mesoporosity within carbons introduce deviations into t-plots, as illustrated in Fig (3.3).

Micropores cause enhanced adsorption at low pressures and this is reflected as a reduced slope (B, Fig 3.3). Extrapolation to the Y-axis yields the micropore volume.

A mesoporous material passes through the origin and then deviates upwards (C, Fig 3.3) indicating capillary condensation after which the slope of the line decreases. A material in which both micropores and macropores are present gives a t-plot which has a positive Y-axis intercept and the characteristics of a mesoporous material (D, Fig 3.3).

The t-plot when presented over a wide thickness range e.g 0 to 1nm shows 2 linear regions Fig (3.4).

The first linear region corresponds to the filling of micropores and the surface coverage of any large pores present. The first linear region extrapolates to the origin and the gradient (multiplied by 15.47 which is the ratio of the gas and liquid densities

Figure 3.3: *t-plots.*

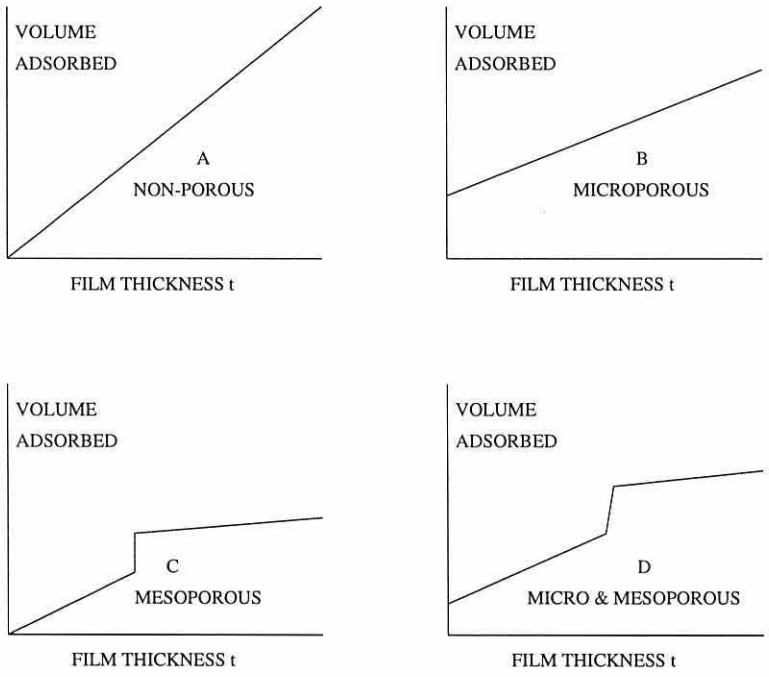

of the adsorbate) gives the value of the total surface area of the material ($m^2.g^{-1}$) (i.e contribution from pores of all sizes).

3.3.1 Surface Area of Mesopores and Macropores

The second linear region corresponds to the adsorption process occurring on the meso and macropores. The surface area provided by the meso and macropores i.e. the external surface area, is obtained by multiplying the gradient of the second linear region by 15.47 to give a value in units of $m^2.g^{-1}$.

Compared to the surface area calculated from the Brunauer, Emmett and Teller equation it is usually within 10-15 percent. However, it is difficult to locate the first linear slope in a t-plot and so the total surface area is calculated from the BET (Section 3.1.5) or MP method (Section 3.4).

Sing et al [73] normalised the isotherms by dividing the amount adsorbed, n at

Figure 3.4: *A Typical t-plot.*

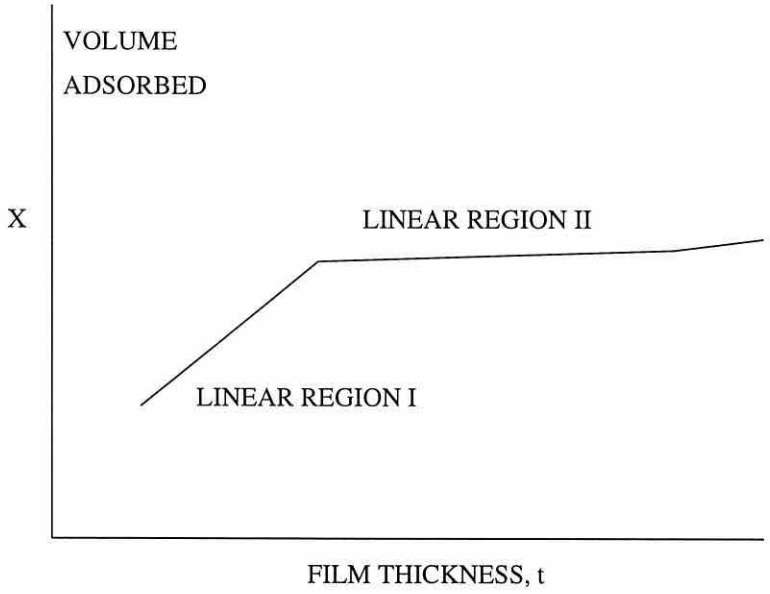

a pressure p by the amount adsorbed, n_s at some fixed pressure ($P/P_o = 0.4$). This reduced amount adsorbed $n/n_s = \alpha_s$ is set equal to 1 at $P/P_o = 0.4$. Using the α_s method the number of molecular layers adsorbed becomes irrelevant. From a plot of the amount adsorbed against α_s the surface area can be calculated from the gradients of the linear regions using a normalising factor obtained from a standard isotherm e.g nitrogen on Vulcan at 77K which has a known surface area.

3.4 MP Method For Calculating The Micropore Size Distribution

An extension of the t-plot method (Section 3.3), the MP method was introduced by Mikhail, Brunauer and Bodor [38] to calculate the micropore volume, micropore surface area and micropore size distribution. The MP method is based upon the thickness plot or 't-plot':

$$t = \frac{Volume\ adsorbed\ (liquid)}{Surface\ Area\ (BET)} \tag{3.26}$$

According to Equation (3.26) all non-porous solids should give the same t-plot assuming that t has the same value at a given relative pressure irrespective of the adsorbent. Deviation from the standard curve (plot of volume adsorbed vs thickness, t) in Fig (3.5) is due to the presence of pores.

The type of pores present is detected by the degree of change in the slope in the following way:

1) The total surface area (SA1) is calculated from the initial slope of the first linear section.

2) A larger pressure range is then assessed, on a slope adjacent to the first, and a surface area value is calculated (SA2) (the total surface less the current pore area contribution).

A larger pressure range is assessed until the sample is saturated; there is no further reduction in gradient and all the micropores have been filled.

The micropore volume is calculated as:

$$MP_{vol} = SA1 - SA2 \text{ x } \left(\frac{t_1 + t_2}{2}\right) \tag{3.27}$$

Thus, calculating MP_{vol} (m^3) for each pressure range or slope yields the micropore volume distribution.

Figure 3.5: *MP Method Calculation Procedure.*

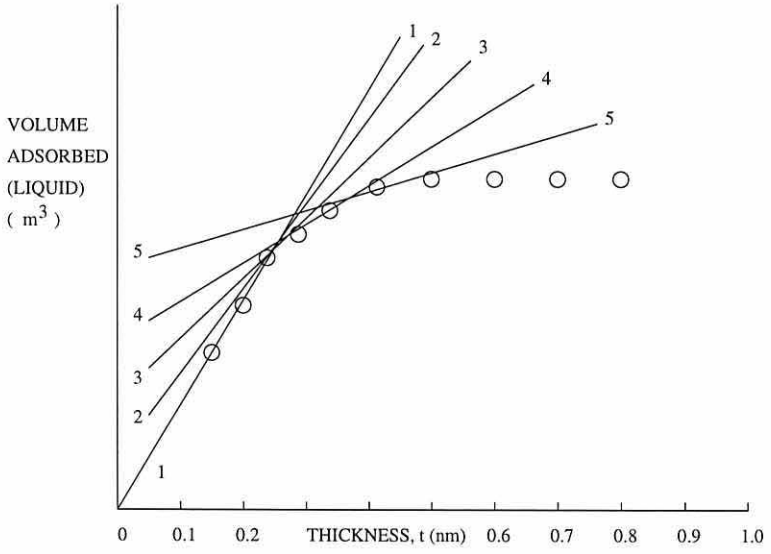

3.5 Dubinin-Radushkevich (DR) Equation

Dubinin used a slit-shaped pore model and assumed that the distribution of pore sizes for an active carbon followed a Gaussian distribution. Unlike the BET and Langmuir equations which use a model process to describe physisorption, Dubinin instead considered the energies of adsorption mathematically for Type I isotherms [55] and showed how the characteristic curve of adsorption is a measure of the pore size or pore energy distributions:

$$W = W_o \, exp[-B \left(\frac{T}{\beta}\right)^2 . \, log^2 \left(\frac{P_o}{P}\right)] \tag{3.28}$$

Where W is the volume of adsorbate filling micropores ($cm^3.g^{-1}$) at relative pressure P/P_o and temperature $T(K)$. W_o is the total volume of micropores ($cm^3 g^{-1}$), P_o is the saturation vapour pressure, β is the adsorbate affinity coefficient and B is known as the structural constant, it can be determined from the slope of a plot of $logW$ against $log^2 \left(\frac{P_o}{P}\right)$.

Plotting $logW$ against $log^2 (P_o/P)$ (Fig 3.6), the micropore volume is taken from where the line intercepts the x=0 axis.

The steeper the gradient the wider the distribution of pore sizes. The DR equation gives information on the relative pore size distributions, extents of micropore volume capacity and deviations of adsorption energies from a Gaussian distribution (Fig 3.7).

The DR equation can also be used over low ranges of pressure (< 0.03) to obtain values for micropore volumes. The DR method assumes that the adsorption

Figure 3.6: *D-R Plots.*

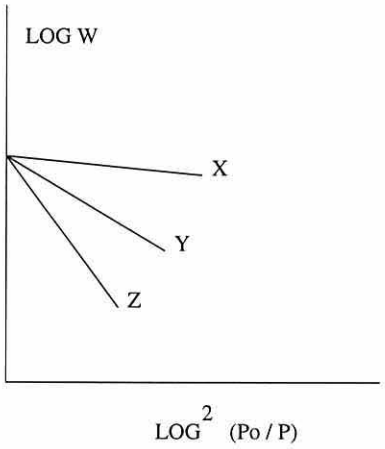

Figure 3.7: *Distribution of Adsorption Energy.*

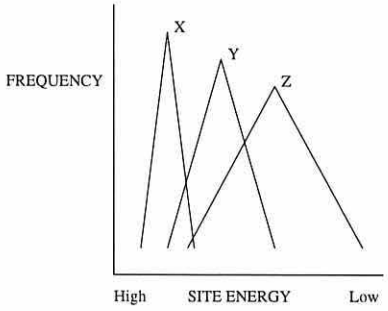

curve is independent of temperature (Van der Waal's forces are also independent of temperature). However, where polar adsorbates are concerned this is not always true. It was proposed by Dubinin and Serpinski [67] that water adsorption occurs at specific hydrophilic sites giving Type III isotherms whereas the DR equation is intended for Type I isotherms. Polar species which adsorb to specific centres therefore only represent a fraction of the available surface area.

3.6 Summary

In summary, the Brunauer, Emmett and Teller method is used to determine the surface area of materials which yield Type II (non-porous or macroporous) or Type IV isotherms provided that the C value is > 100 and point B on the isotherm can be located. Nitrogen (at 77K) has been found to be the most suitable adsorptive for surface area determination.

The adsorption process occurring in porous carbons is not accounted for in the model used for the Brunauer, Emmett and Teller equation. It follows that problems arise when porous carbons are considered as the linear BET plots are usually given at $P/P_o < 0.1$ and point B is difficult to locate thus giving a questionable surface area value. The Brunauer, Emmett and Teller method can be used to determine the surface area of microporous solids provided that the monolayer volume is located in the relative pressure range 0.05 to 0.3. However, the Brunauer, Emmett and Teller method does not allow the determination of the micropore volume. When BET areas of porous carbons are quoted the experimental conditions and range of

linearity should also be quoted.

The Horvath and Kawazoe method is most suited to carbons and zeolites and was developed to determine the effective pore diameters of microporous solids ($< 20\mathring{A}$) and thus the effective micropore size distributions.

The t-plot method is used to detect the type of porosity present in a material and is used to check the consistency of BET areas. The surface area provided by meso and macropores may be calculated from the slope of the second linear region.

For ungraphitised carbons the α_s method gives surface area values which are in excellent agreement with those obtained using the BET equation but this is not true with graphitised carbons. This is because the first part of the isotherm is influenced by microporosity and surface structure [63] which the α_s method does not account for. The distribution of pore sizes may not necessarily be restricted to definite IUPAC ranges and small contributions from different ranges are not easily detected by simply looking at the shape of an isotherm. The α_s method however is useful in detecting such contributions e.g. from micropores to the mesopore range. The advantage of the α_s method over the t-plot method is that it can be used for Type II and Type III isotherms [64] using adsorbates other than nitrogen. The α_s method therefore allows the determination of the total surface area, the external surface area and the micropore volume.

The MP method is most suited to micropore and mesoporous materials for analysing volume, surface area and distributions. However, the Horvath and Kawazoe method would be chosen for a more detailed description of the micropore distribution.

The DR equation corresponds to Type I isotherms [65] which are characteristic of active carbons. At low pressures adsorption on the external surface is negligible and plotting $logW$ against $log^2\left(\frac{P_o}{P}\right)$ gives a straight line from which B, E_o and limiting micropore volume W_o can be evaluated.

Dubinin claims that the micropore volume is filled by condensed adsorbate. However, relatively large micropore systems without molecular sieve effects give similar values of W_o using the limiting amounts absorbed, N_{a0}, and the molar volume of the liquid adsorbates. This suggests the adsorbed state is similar to the liquid state at the same pressure and temperature. With narrow micropores where geometrical constraints are present the density of the adsorbate may be different. As long as molecular sieve effects are absent the adsorption data can be fitted over wide pressure and temperature ranges for different vapours.

Dubinin's theory for the volume filling of micropores does not apply when water acts as an adsorbate; the weak interaction between the non-polar surface and water molecules results in micropore filling occurring at higher relative pressures than those for organic compounds.

In the following Chapter 4 the experimental adsorption isotherms of low surface area carbons will be interpreted and their surface areas calculated using the BET method outlined above.

Chapter 4

Non-Porous Carbons

4.1 Introduction

This chapter examines the behaviour of gases adsorbing on low surface area (non-microporous) carbons at constant temperature. The aim of this section was to determine the values of the non-local density functional interaction parameters for various gases at 77K and 293K for later use in determining the pore size distributions of porous carbon surfaces (Chapter 5).

Experimentally determined isotherms of the amount of nitrogen, argon and methane adsorbed onto non-microporous carbons were measured volumetrically at 77K [16] (gas adsorption is easily measurable at 77K and is commonly used). Similar isotherms for the adsorption of nitrogen, carbon-dioxide and methane onto non-microporous carbons were also measured at 293K. The Coulter Omnisorp 100cx apparatus described in Chapter 3 was used in all the experiments. Experimental adsorption isotherm data for argon on Vulcan at 87K was supplied by Coulter [84].

Theoretical isotherms were calculated using non-local density functional theory (Chapter 2) on a model non-porous surface at 77K and 293K (Fig 2.3) for comparison with the experimental data. These isotherms will also be used as a basis for predicting the behaviour of gas uptake on porous carbons in Chapter 5.

4.2 Experimental Adsorption Isotherms

4.2.1 Adsorbates and adsorbents

Vulcan 3-G-2700-Graphitised Carbon Black (No. M11-02, Batch S6), and Sterling FT-G-2700-Graphitised Carbon Black (No. M11-01, Batch S5) are certified reference materials and were supplied by the Laboratory of the Government Chemist for use as adsorbents [80]. Carbon blacks: Vulcan and Sterling have been shown to possess relatively uniform surfaces for gas adsorption [81]. This is achieved by graphitisation whereby three dimensional atomic structure begins to develop in the carbon on heating to temperatures near 1700^{o}C. Graphite (supplied by Aldrich) was also used as an adsorbent. The extent of graphitisation of Vulcan and Sterling is revealed by their x-ray diffraction patterns (Section 4.2.7). The adsorbates: nitrogen, methane, argon, and carbon-dioxide were of ultra high purity gases (99.999 percent by volume) [81].

Experimental adsorption isotherms were measured by the static flow method using the Omnisorp apparatus described in the previous chapter. Measurements were made at 2 temperatures: liquid nitrogen was used to cool the samples to 77K for some experiments, other experiments were done at room temperature (293K).

4.2.2 Saturation Vapour Pressures, P_o

The pressure of a fluid which is at equilibrium and is compressed isothermally (below its critical temperature) will rise until the saturation vapour pressure is reached and the first drop of liquid is formed. The saturation vapour pressure, P_o^{EXP} of

nitrogen, argon and methane at 77K were determined experimentally and compared with values calculated from an equation of state [75], P_o^{EQS}. The values are listed in Table 4.1.

Table 4.1: *Saturation Vapour Pressure Parameters.*

	Nitrogen	**Methane**	**Argon**	**Argon**
Adsorption Temperature (K)	77	77	77	87
Critical Temperature (K)	126.20	190.55	150.86	150.86
P_o^{EQS} **(mmHg)**	785.0	8.67	187.69	728.70
P_o^{EQS} **(Bar)**	1.05	0.01	0.25	0.97
P_o^{EXP} **(mmHg)**	780.0	11.0	208.0	776.0
P_o^{EXP} **(Bar)**	1.04	0.01	0.28	1.03

Exact agreement is not to be expected between the experimental and calculated values of the saturation vapour pressure because the ideal gas laws have been used in determining P_o^{EQS}. The saturation pressures are different for nitrogen, argon and methane due to the dissimilar molecular shape and intermolecular forces between the molecules of each gas.

4.2.3 Gas Adsorption onto Vulcan at 77K

The adsorption of nitrogen, argon and methane onto Vulcan was measured at regular intervals up to a cut-off pressure of approximately 0.32 Bar, 0.08 Bar and 0.01 Bar respectively. The experiments were repeated several times in order to ensure

reproducibility and to calculate the mean amount of gas adsorbed at each pressure value to give the mean adsorption isotherms.

Measurements were taken up to different maximum pressures for each gas to ensure that the monolayer formation was complete for each adsorbate. The maximum pressures then provided enough data for the surface area to be calculated using the BET method (Section 4.2.4).

The mean saturation vapour pressure for each experiment is given in Table 4.1.

The total time taken to measure an adsorption isotherm i.e. the cumulative time to measure the amount adsorbed at each pressure value was approximately 4 hr, with between 5 and 20 hr for sample preparation (out-gassing at high temperature). There was no appreciable difference in the amount of gas adsorbed onto Vulcan using an out-gassing temperature of 573K or 673K, neither from out-gassing for 5 hr or 16 hr. However, differences were noted for out-gassing times of less than 5 hr so this was taken to be the minimum amount of time required. The adsorption dose (Section 3.1.1) was set to 5 Torr in all the experiments. The adsorption dose is programmed by the user and determines the incremental increase in pressure. At each interval the amount of gas adsorbed is measured until the adsorption cut-off pressure is reached and the experiment stops. The adsorption dose therefore determines the number of data points in the isotherm.

An average number of 35 data-points were recorded along each isotherm. In each experiment a new sample of Vulcan is used but it is taken from the same batch (Section 4.2).

The mean adsorption isotherms of nitrogen, argon and methane onto Vulcan are

shown in Fig 4.1. The amount of vapour adsorbed (y-axis) has units of cc (STP) per gram of Vulcan, and a logarithmic scale is used for the x-axis (absolute pressure in units of Bar) to highlight the main features of the isotherms.

Figure 4.1: *Mean Adsorption Isotherms of Nitrogen, Argon and Methane onto Vulcan at 77K on a logarithmic pressure scale.*

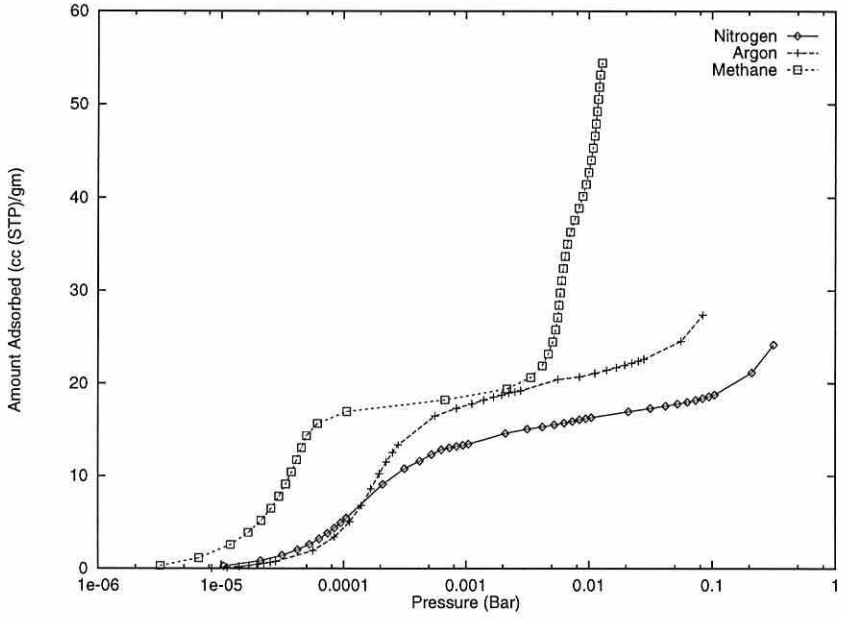

At low pressures (10^{-6} to 10^{-5} Bar), little adsorption occurs for all 3 gases. At around 10^{-5} Bar for nitrogen and argon and 10^{-6} Bar for methane, a point of inflection occurs and there is a sharp rise in adsorption with increasing gas pressure. This corresponds to the start of the formation of a monolayer of atoms on the carbon surface. The second point of inflexion of an isotherm indicates the completion of the monolayer, it's height V_B corresponds to the monolayer capacity V_m and is a measure of the volume of adsorbate molecules (STP) which covers the surface of the material in a layer one molecule thick per gram of material and is calculated using

the BET equation (Section 4.2.4). V_B was taken as the point where the two lines of best fit through the two linear regions either side of the inflexion point intersect. The ease of locating V_B therefore depends on the sharpness of the knee. Referring to Fig 4.1, V_B differs for different vapours, starting with the highest first the order is: argon (V_B=16.5 $cm^3.g^{-1}$ at 5.6x10^{-4} Bar), methane (V_B=16.3 $cm^3.g^{-1}$ at 7x10^{-5} Bar), and nitrogen (V_B=13.1 $cm^3.g^{-1}$ at 8.3x10^{-4} Bar).

The formation of the monolayer of methane occurs in a lower absolute pressure range (4x10^{-7} to 7.0x10^{-5} Bar) than that observed with nitrogen (1.1x10^{-5} to 8.3x10^{-4} Bar) and argon (8.4x10^{-6} to 5.6x10^{-4} Bar).

For the adsorption of nitrogen and argon, on completion of the monolayer a second point of inflexion occurs and is followed by a gradual increase in the amount of gas adsorbed as a multilayer is built up on the surface. The adsorption of methane gives a more pronounced layering transition in the multilayer region than that of nitrogen or argon.

At low pressures up to 2x10^{-4} Bar the nitrogen and argon isotherms are almost identical, this implies similar forces of attraction between argon and nitrogen adsorbate molecules and the Vulcan surface. A crossing point occurs at 1.4x10^{-4} Bar (corresponding to 6.82 cm^3 (STP).g^{-1} of vapour adsorbed) where the uptake of argon becomes much more rapid than that of nitrogen. This may be due to the packing arrangements of adsorbate molecules on the carbon surface; argon is cited as having a smaller diameter (3.4$\AA$) than nitrogen (3.6$\AA$) or methane (3.8$\AA$) molecules and is spherical in shape whereas nitrogen is linear. Perhaps argon molecules pack more efficiently than nitrogen molecules. There is no information at present on the

packing arrangement.

It is observed that the methane adsorption isotherms are steeper in the monolayer formation region (gradient of 2x10^5 cm^3.g^{-1}.Bar^{-1}) compared to argon adsorption isotherms (gradient of 3x10^{4}cm^3.g^{-1}.Bar^{-1}), suggesting that the force of attraction between the Vulcan surface and methane adsorbate molecules is greater than the force of attraction with argon adsorbate molecules which is in turn greater than the attraction with nitrogen molecules (gradient of 1x10^{4}cm^3.g^{-1}.Bar^{-1}). This trend has also been observed with the adsorption of argon and nitrogen on microporous zeolite at the same temperature of 77K [77].

Since similar differences in the formation of monolayers by the gases are observed on both zeolite and Vulcan, it seems likely that it is the gas-gas molecular interaction rather than the gas-solid interaction that produces the different rates of monolayer formation with increasing pressure. We confirm this hypothesis using density functional theory in Section (4.3.2).

4.2.4 The Specific Surface Area of Vulcan

In order to express the theoretical amount of gas adsorbed on a flat surface in the same units as the experimental amount of gas adsorbed on Vulcan, the surface area of Vulcan is required. In accordance with the certification experiments performed at the Laboratory of the Government Chemist, the BET function $P/V_m(P_o^{EXP} - P)$ was plotted against the relative pressure P/P_o^{EXP} for each set of isotherm data. Within the almost linear region of the BET plot, the best fit straight line was calculated. From its intercept and gradient, the monolayer capacity, V_m, per unit

mass of adsorbent was calculated (Section 3.1.5). The BET plot for the adsorption of nitrogen onto Vulcan is shown (Fig 4.2).

Figure 4.2: *BET plot from the Adsorption of Nitrogen onto Vulcan.*

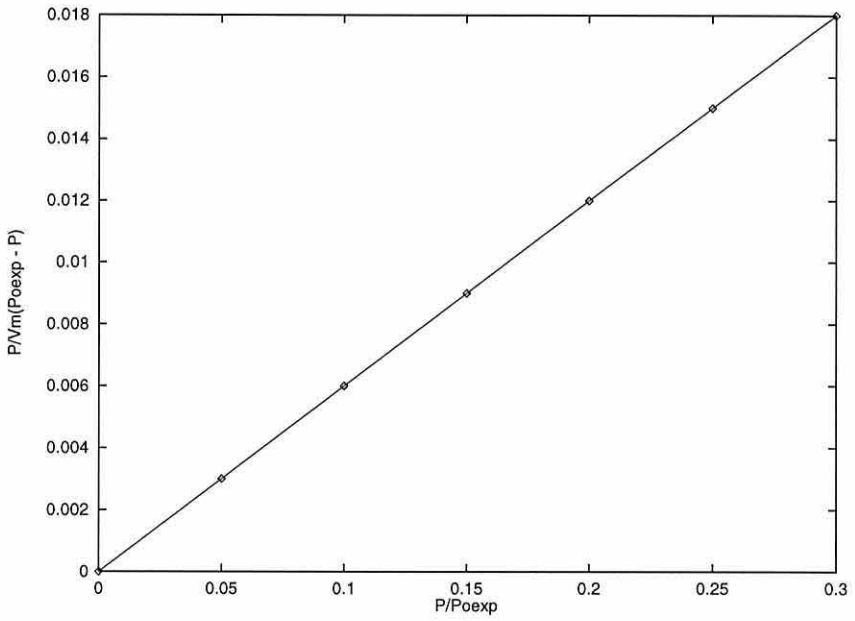

The specific surface area, SA_{BET}, ($m^2.g^{-1}$) was calculated for each set of adsorption data by multiplying ,V_m, by the cross-sectional area per molecule, σ_A and Avogadro's constant, N and then dividing over the molar volume (Molar_V):

$$SA_{BET} = (\sigma_A \; N \; V_m) \, / Molar_V \tag{4.1}$$

A value of 16.2$\mathring{A}^2$ [85] was assumed for the cross-sectional area of the nitrogen molecule, (16.6$\mathring{A}^2$ [85] for argon, and 16.7$\mathring{A}^2$ [85] for methane), a value of 6.022045x$10^{23}$$mol^{-1}$ was used for Avogadro's constant, N and a value of 22.414 L mol^{-1} for the molar volume, $Molar_V$. Specific surface area values calculated from the adsorption data plotted in the form of (Fig 4.2) are given in Table 4.2.

The arithmetic mean for the Vulcan BET specific surface area from our nitrogen measurements is 72.6 ± 0.6 $m^2.g^{-1}$, this does not depend strongly on the adsorbing gas used and lies well within the uncertainty interval of the original certification of 71.3 ± 2.7 $m^2.g^{-1}$ measured by the Laboratory of the Government Chemists (LGC) and that obtained by Lastoskie, Gubbins and Quirke (LGQ) (71.6 $m^2.g^{-1}$) [46]. The small differences between the different surface area values may be accounted for by the fact that different samples have been used for each experiment.

Table 4.2: *BET Specific Surface Areas, Monolayer Capacities, V_m, and 'Knee-point' values, V_B From The Adsorption of Nitrogen, Argon and Methane onto Vulcan at 77K.*

Adsorbate	V_m **(ml.g^{-1})**	V_B **(cm^3.g^{-1})**	SA_{BET}**(m^2.g^{-1})**
Nitrogen (Bangor)	14.0	13.13	72.64
Nitrogen (LGC (1974))	-	-	71.3
Nitrogen (LGQ [46])	-	-	71.6
Argon (Bangor)	19.656	16.5	87.26
Methane (Bangor)	15.86	16.35	70.58
Argon (Coulter) (87 K)	18.17	15.0	80.42

4.2.5 Gas adsorption on Sterling and Graphite at 77K

Adsorption isotherms of nitrogen, argon and methane on Sterling were measured up to a cut-off pressure of 0.4 Bar, 0.13 Bar, and 0.01 Bar respectively. The isotherms

were measured several times to ensure reproducibility. A different sample of Sterling was used for each experiment but each sample was taken from the same batch (Section 4.2). The mean adsorption isotherms are shown in Fig 4.3.

Figure 4.3: *Mean Adsorption Isotherms of Nitrogen, Argon and Methane onto Sterling on a logarithmic pressure scale.*

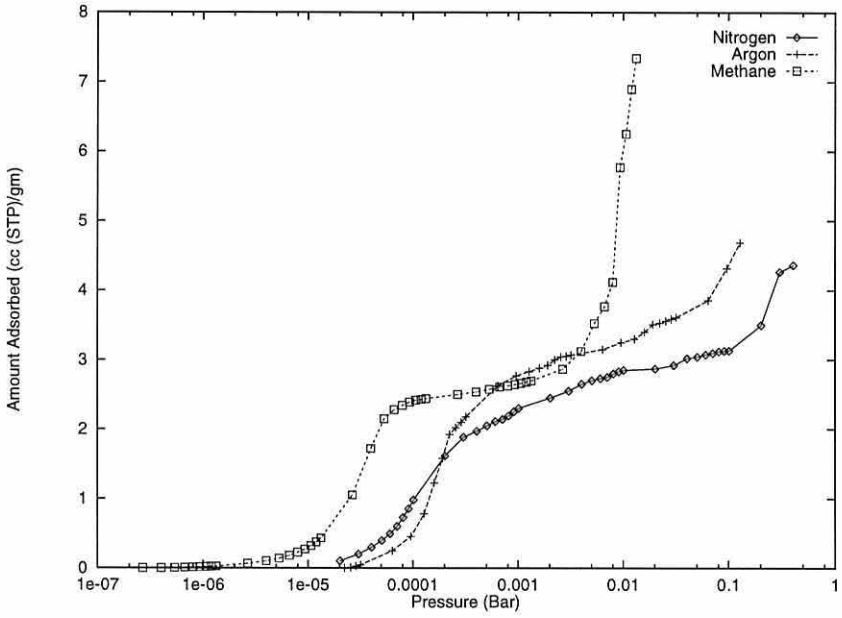

The adsorption of nitrogen and argon on graphite was measured several times to a cut-off pressure of 0.4 Bar and 0.13 Bar respectively. The mean adsorption isotherms are shown in Fig 4.4. The BET method was also applied to the Sterling and graphite isotherms and the surface area values are listed in Tables 4.3 and 4.4.

Figure 4.4: *Adsorption of Nitrogen and Argon on graphite on a logarithmic pressure scale.*

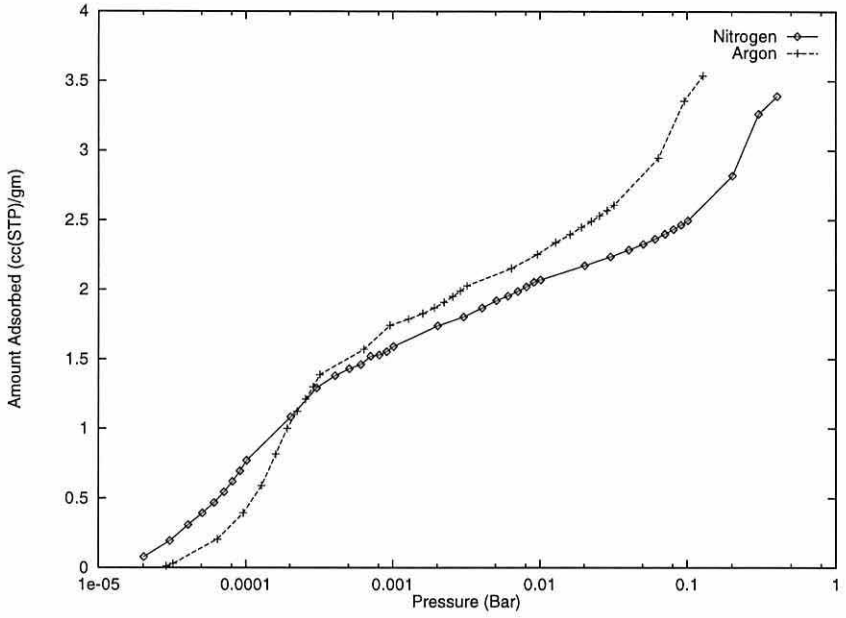

Table 4.3: *BET Specific Surface Areas, Monolayer Capacities, V_m, and 'Knee-point' Values, V_B From The Adsorption of Nitrogen, Argon and Methane onto Sterling.*

Adsorbate	V_m $(\mathbf{ml.g^{-1}})$	V_B $(\mathbf{ml.g^{-1}})$	$SA_{BET}(\mathbf{m^2.g^{-1}})$
Nitrogen (Bangor)	2.58	1.875	11.14
Nitrogen ([76])	-	-	11.10
Argon (Bangor)	2.93	2.375	12.95
Argon ([76])(87 K)	-	-	13.00
Methane (Bangor)	1.882	2.2	8.376

Table 4.4: *BET Specific Surface Areas, Monolayer Capacities, V_m, and 'Knee-point' Values, V_B, From The Adsorption of Nitrogen and Argon onto graphite.*

Adsorbate	V_m $(\mathbf{ml.g^{-1}})$	V_B $(\mathbf{ml.g^{-1}})$	$SA_{BET}(\mathbf{m^2.g^{-1}})$
Nitrogen (Bangor)	2.24	1.38	9.66
Argon (Bangor)	2.407	1.47	10.65

4.2.6 Comparison of the Adsorption of Nitrogen onto Vulcan, Sterling and Graphite

The three adsorbents (Vulcan, Sterling and graphite) are considered to have no internal surface area (i.e. no surface pores). In this case, 2 different types of isotherm are commonly found: Type II and III of the BET classification (Section 1.1) corresponding to the strong physical adsorption of vapours onto non-microporous surfaces and non-microporous surfaces which interact weakly with the adsorbate molecules respectively.

Comparing low-surface area materials; the adsorption of nitrogen onto Vulcan, Sterling and graphite on a logarithmic absolute pressure scale (Figs 4.1, 4.3, 4.4) shows that the three materials yield a Type II shaped isotherm in the BET classification (the initial uptake of gas increases rapidly until the completion of the monolayer at the first point of inflexion and then less rapidly until the second point of inflexion where the branch of the isotherm turns upwards) but they adsorb different amounts. The difference in the calculated surface area values for the three materials (Tables 4.2 to 4.4) are due to the different adsorption values.

At low pressures (less than approximately 10^{-3} Bar) the initial uptake of nitrogen is rapid on Vulcan, Sterling and graphite. Referring to Table 4.2, 4.3, and 4.4, Vulcan gives the larger monolayer capacity and knee-point values for the adsorption of nitrogen than Sterling or graphite.

After the 'knee' of the isotherm a multilayer builds up on the surface. In this multilayer region, one would expect all curves to have a similar gradient because the dominating interaction now becomes that between the adsorbate molecules (nitrogen molecules) in all cases.

From the nitrogen adsorption measurements, the mean Sterling BET specific surface area value from our measurements is 11.14 $\pm$0.4 $m^2.g^{-1}$, which is in excellent agreement with that obtained by Olivier [76] of 11.10 $m^2.g^{-1}$. The lower specific surface area of Sterling (11.14 $m^2.g^{-1}$) and graphite (9.66 $m^2.g^{-1}$) [Tables 4.3, and 4.4 respectively] compared to 72.64 $m^2.g^{-1}$ for Vulcan [Table 4.2] suggests that either graphite has the most uniform surface or that graphite and Sterling consist of particles with a larger diameter and therefore smaller specific surface area than Vulcan. The extent of graphitisation in Vulcan and Sterling is reflected in their x-ray diffraction patterns and images obtained from the scanning electron microscope which will be discussed in the next section.

4.2.7 Direct Examination of the surfaces of Vulcan, Graphite and Sterling

Scanning Electron Microscopy

Surface images of Vulcan, Sterling and graphite were taken on a scanning electron microscope (SEM) H-1500 (Hitachi) [17].

SEM images of the surface of Vulcan are shown in Figs 4.5 to 4.12. Fig 4.5 shows that individual grains can be distinguished. The size of particles is difficult to estimate directly from SEM images (Fig 4.7). Fig 4.6 shows an amazingly regular surface defect resembling a shallow volcano like crater of 4μm in diameter. A 'lid' possibly from this defect is also visible. Inside the 'crater', elemental particles forming the mesoporous structure of graphitised Vulcan are revealed.

A typical low resolution SEM image of Sterling shows a flat surface with many cracks (Fig 4.8), which at higher resolution reveals small particles (Fig 4.9), elementary building blocks of this material. Their particle size distribution seems to be quite narrow. The average particle diameter is approximately 200 to 300nm.

Graphite is shown (Fig 4.10) to consist of flat sheets of various thickness forming well observable disintegrated flakes (Fig 4.11). There is no indication of discrete particles at very high magnification (Fig 4.12). The graphite flakes are damaged probably due to the preparation process of the commercial 'graphite powder' product. High resolution images of an individual sheet shows a flat surface with very limited extent of surface defects. This structure corresponds to the low surface area of graphite calculated from gas adsorption.

Figure 4.5: *SEM Image of Vulcan Surface [2.5cm=86μm]*

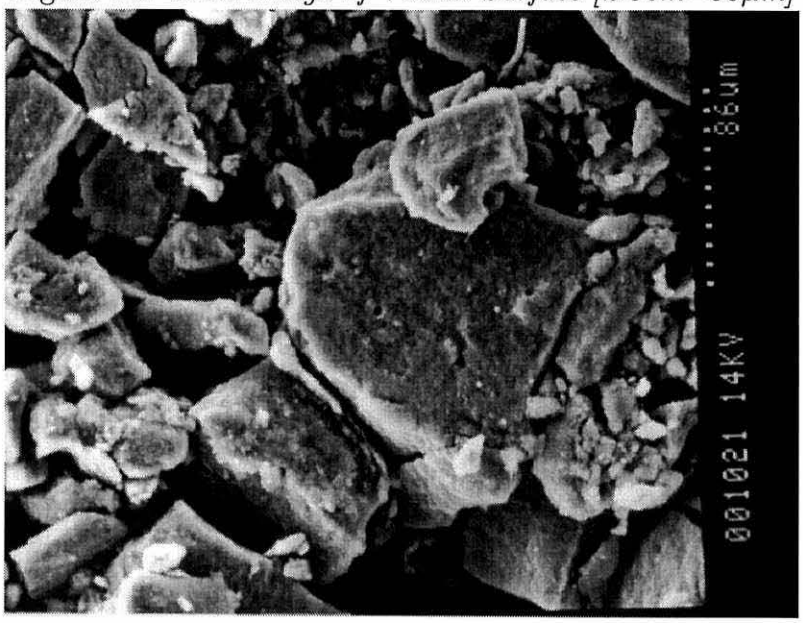

Figure 4.6: *SEM Image of Vulcan Surface [2.5cm=3.0μm]*

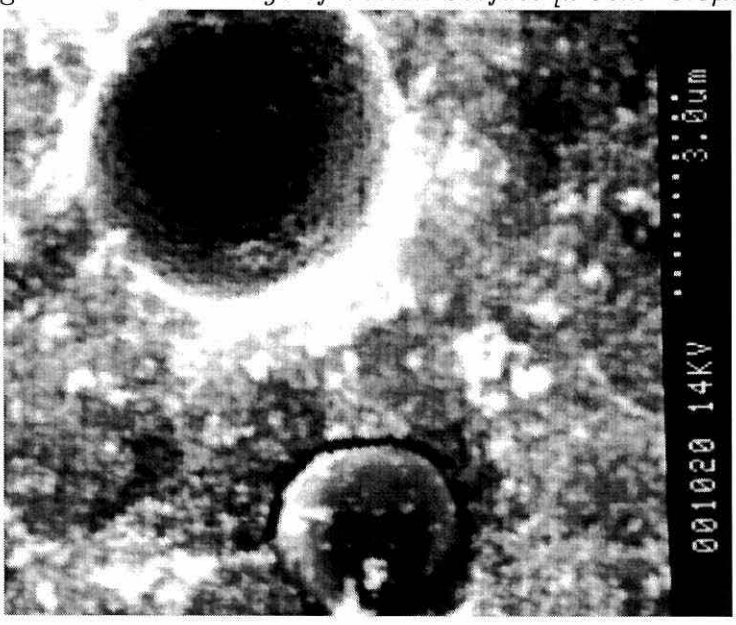

Figure 4.7: *SEM Image of Vulcan Surface [2.5cm=15.8μm]*

Figure 4.8: *SEM Image of Sterling Surface [2.5cm=15.0μm]*

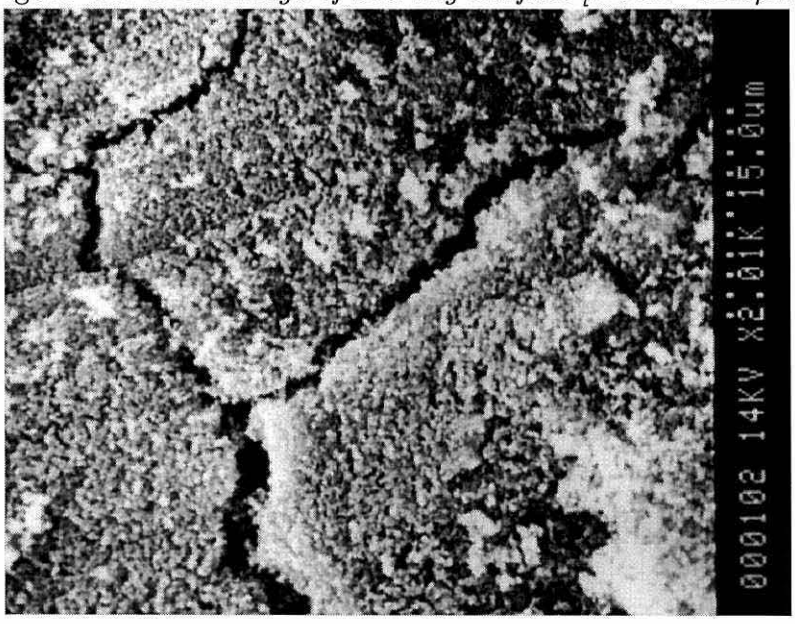

Figure 4.9: *SEM Image of Sterling Surface [3.0cm=5.0μm]*

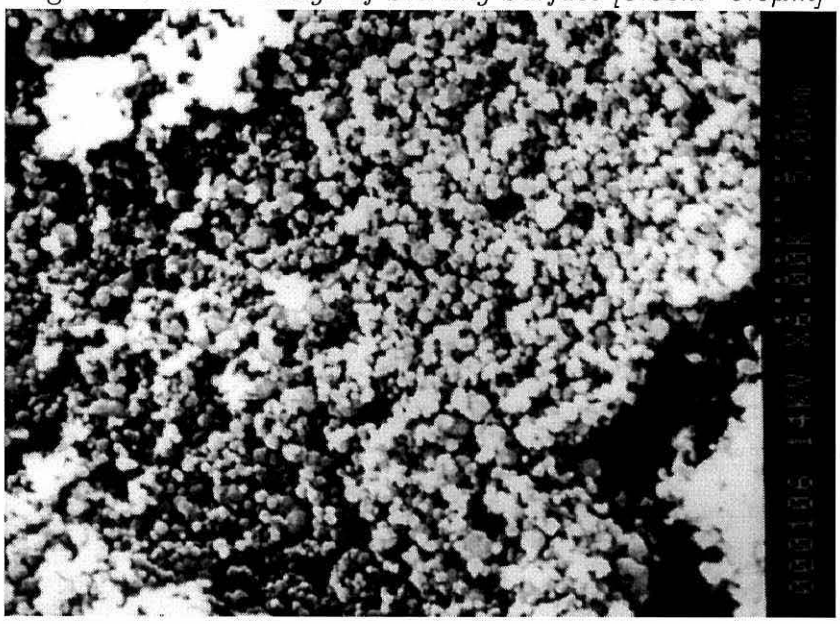

Figure 4.10: *SEM Image of Graphite Surface [2.5cm=2.48μm]*

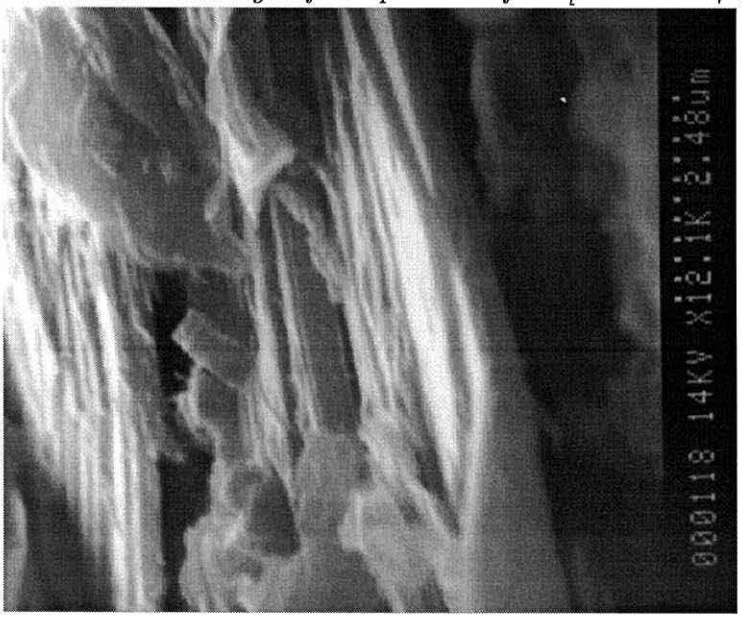

Figure 4.11: *SEM Image of Graphite Surface [3.0cm=15.0μm]*

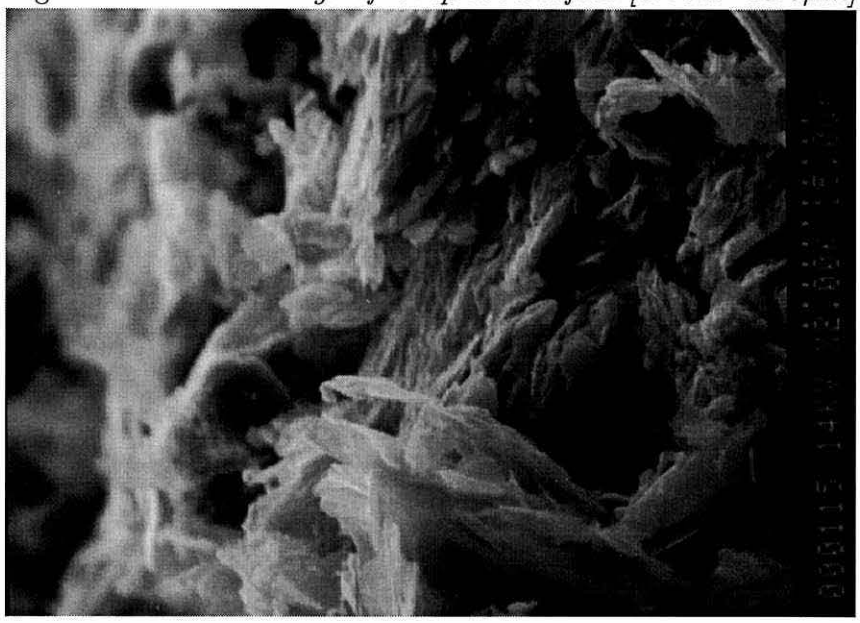

Figure 4.12: *SEM Image of Graphite Surface [3cm=2.7μm]*

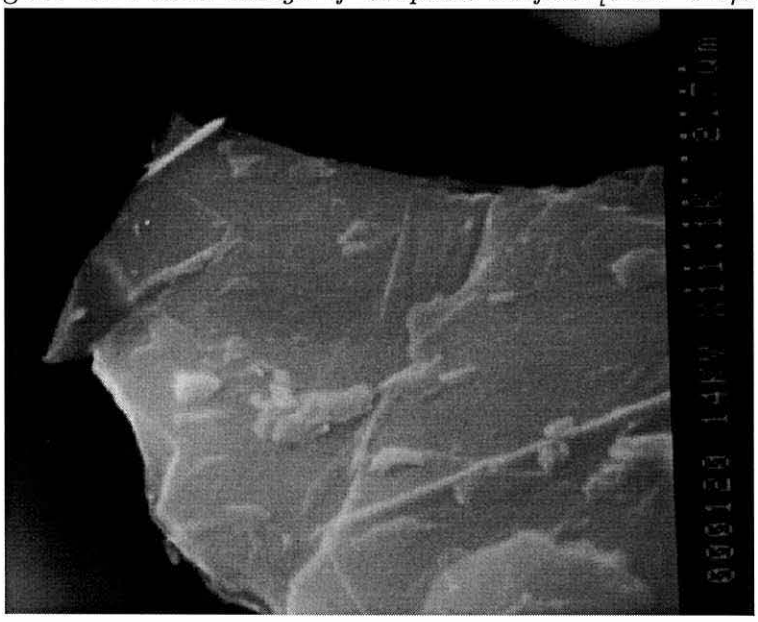

X-Ray Diffraction Patterns from Vulcan, Sterling and Graphite

X-ray diffraction patterns of the samples were studied on a PW1010 apparatus (Phillips) with a CuKα radiation source and iron filter [17]. Diffractograms were recorded from 5 to $120^0 2\theta$ and a single run took 14 hours. The diffractograms obtained were compared with a database diffraction pattern [70] for graphite in order to assess the extent of graphitisation in each material.

The common graphitic nature of the materials is clearly shown by their diffraction line patterns listed in Table 4.5. However, there are differences amongst them. The diffractogram of natural graphite shows a well-developed crystallographic structure with intense and sharp lines corresponding to X-ray diffraction from all major crystallographic planes of the crystal of graphite. Graphitisation was assessed by comparison with referential Sri Lanka graphite [68], [69] and the database reference pattern. Good agreement in occurrence and location of the 10 major planes was found.

Sterling exhibits less intense peaks than graphite. The intensity of diffraction from the plane (0,0,2) is still quite intense however its location does not coincide perfectly. The diffraction line from the plane (1,0,1) at 2.03$\mathring{A}$ is very diffuse and the line from (0,0,1) is absent. The d-spacings corresponding to the line (1,1,0) coincides well (1.23$\mathring{A}$) however presence of the last 3 planes is indicated only by an increased background.

Vulcan's patterns display only a few lines which are of much lower intensity than those observed with graphite. The main bands are very diffuse which indicates much

smaller elemental particle size. The d-spacing corresponding to the line (0,0,2) is shifted to 3.49$\mathring{A}$. The most intensive plane for all 3 materials is (0,0,2) [Table 4.5]. Thus Vulcan particles are shown to be smaller than Sterling particles which are smaller than graphite particles.

Table 4.5: *d-spacings and crystal diffraction planes (Cr.Pl) of Vulcan, Sterling, Graphite, Sri Lanka Graphite (S.L.G) and Database Reference Pattern (13-0477), (Ref-Patt).*

Cr.Pl.	**Graphite**($\mathring{A}$)	**Sterling**($\mathring{A}$)	**Vulcan**($\mathring{A}$)	**S.L.G**($\mathring{A}$)	**Ref.Patt** ($\mathring{A}$)
0,0,2	3.38	3.41	3.49	3.36	3.35
1,0,0	2.13	2.14	2.13	2.13	2.13
1,0,1	2.03	2.03	2.03	2.03	2.04
0,0,1	1.80	-	-	1.80	1.80
0,0,4	1.67	1.70	1.69	1.67	1.67
1,0,3	1.54	1.49	-	1.54	1.54
1,1,0	1.23	1.23	1.22	1.23	1.23
1,1,2	1.16	1.16	-	1.15	1.15
0,0,6	1.12	1.13	-	1.15	1.15
1,0,5	1.01	1.02	-	1.06	1.01

4.2.8 Comparison of the Adsorption of Argon onto Vulcan, Sterling and Graphite

From the BET Type II shapes of the adsorption isotherms (with 2 steps in the isotherm) in Figs 4.1, 4.3 and 4.4 we infer that from the adsorption of argon onto Vulcan, Sterling and graphite there is a strong interaction between the surface and adsorbate molecules.

In Figs 4.1, 4.3, and 4.4 the mean uptake of argon onto Vulcan occurs at a lower starting pressure (8.4×10^{-6} Bar) than Sterling (2.2×10^{-5} Bar) and graphite (2.9×10^{-5} Bar) and then increases rapidly up to a pressure of 5.6×10^{-4} Bar (Vulcan), 1.6×10^{-4} Bar (Sterling), 2.8×10^{-4} Bar (graphite). Indicating that an argon monolayer will form most readily on Vulcan than with Sterling, as observed with nitrogen (Section 4.2.3). The appearance of the well-defined second point of inflection indicates the completion of monolayer coverage and the onset of multilayer adsorption.

In Figs 4.1, 4.3 and 4.4 the height of the 'knee', V_B, corresponds to 16.5 $cm^3.g^{-1}$ (Vulcan), 2.4 $cm^3.g^{-1}$ (Sterling) and 1.5 $cm^3.g^{-1}$ (graphite). The mean BET monolayer capacity, V_m was 19.6 $m^2.g^{-1}$ [Table 4.2], 2.9 $cm^3.g^{-1}$ for Sterling [Table 4.3] and 2.4 $cm^3.g^{-1}$ for graphite [Table 4.4].

The volumetric adsorption of argon onto Sterling and Vulcan has not previously been measured. This is possibly due to the common assumption that argon will solidify in pores. However, there is substantial evidence that adsorption into pores involves a decrease in the liquid-solid transition temperature [78], [79] and also an increase [12]. Studies of the adsorption of argon at liquid nitrogen temperature (Figs

4.1, 4.3 and 4.4) show that the data is reproducible.

The mean BET specific surface area value for Vulcan with argon as the adsorbate at 77K is 87.3 $\pm$0.8 $m^2.g^{-1}$ [Table 4.2] and the specific surface area of Sterling is 13.0 $\pm$ 0.2 $m^2.g^{-1}$. This is in excellent agreement with the value obtained by Olivier of 13.0 $m^2.g^{-1}$ at a temperature of 87K [76]. The mean BET specific surface area for graphite was calculated as 10.65 $m^2.g^{-1}$.

4.2.9 Comparison of the Adsorption of Nitrogen and Argon onto Sterling and graphite

Adsorption of nitrogen and argon onto Sterling (Fig 4.3) starts at the same absolute pressure value of approximately 2x10^{-5} Bar, an order of magnitude higher than that obtained with Vulcan as the adsorbent. The isotherms are of Type II as found for Vulcan.

The argon and nitrogen isotherms crossover at 1.4x10^{-4} Bar. This also occurred for adsorption onto Vulcan at 1.4x10^{-4} Bar and graphite at 2x10^{-4} Bar. At low pressure nitrogen is preferentially adsorbed over argon whereas at higher pressures the uptake of argon is greater than that of nitrogen and the gradient is somewhat steeper; 1.3x10^4 $cm^3.g^{-1}$ Bar^{-1} for argon compared to 6.9x10^3 $cm^3.g^{-1}$ Bar for nitrogen. Adsorption of nitrogen and argon onto graphite (Fig 4.4) starts at the absolute pressure value 2.0x10^{-5} Bar and 2.9x10^{-5} Bar respectively, similar to that observed with Sterling. As observed with the adsorption isotherms of Vulcan and Sterling, graphite yields Type II isotherms with the uptake of nitrogen greater than

argon at pressures below approximately $2x10^{-4}$ Bar. After this crossing point, the uptake of argon is greater than nitrogen. This suggests that the interaction between argon molecules is stronger than that between nitrogen molecules. Indeed, theory has shown that the potential energy of interaction between argon fluid molecules is greater than that between nitrogen fluid molecules (Section 4.3.1) and the larger the value of the potential energy between fluid molecules the steeper the gradient of the isotherm in the monolayer formation region (see Section 4.3.2).

4.2.10 Temperature dependence of the Adsorption of Argon onto Vulcan

Finally, since all our measurements were carried out at 77K, we show the effect of changing the ambient temperature on adsorption. The mean adsorption of argon onto Vulcan at 77K is compared with the adsorption of argon onto Vulcan at 87K (data supplied by Coulter) (Fig 4.13).

The data clearly shows that the isotherms are both of Type II of the BET classification but differ in magnitude. The pressure at which adsorption occurs increases with temperature. At low pressure the gas molecules approach ideality and therefore [13]:

$$\rho_{ads} = \rho_{id} e^{-\epsilon_{sf}/kT} \tag{4.2}$$

Where ρ_{ads} is the amount of gas adsorbed, ρ_{id} is the amount of adsorbate adsorbed for an ideal gas, ϵ_{sf} is the potential energy for the solid-fluid interaction, k is

Boltzmann's constant and T is the temperature. Therefore, the ratio of adsorption at two different temperatures is [13]:

$$\frac{\rho_{ads,77}}{\rho_{ads,87}} = \frac{87}{77} e^{-\epsilon_{sf}(1/k77 - 1/k87)} \tag{4.3}$$

At low pressures we would expect the adsorption to start at a lower pressure value at a lower temperature. Fig 4.13 shows that this is the case.

Figure 4.13: *Adsorption of Argon onto Vulcan at 77K and 87K.*

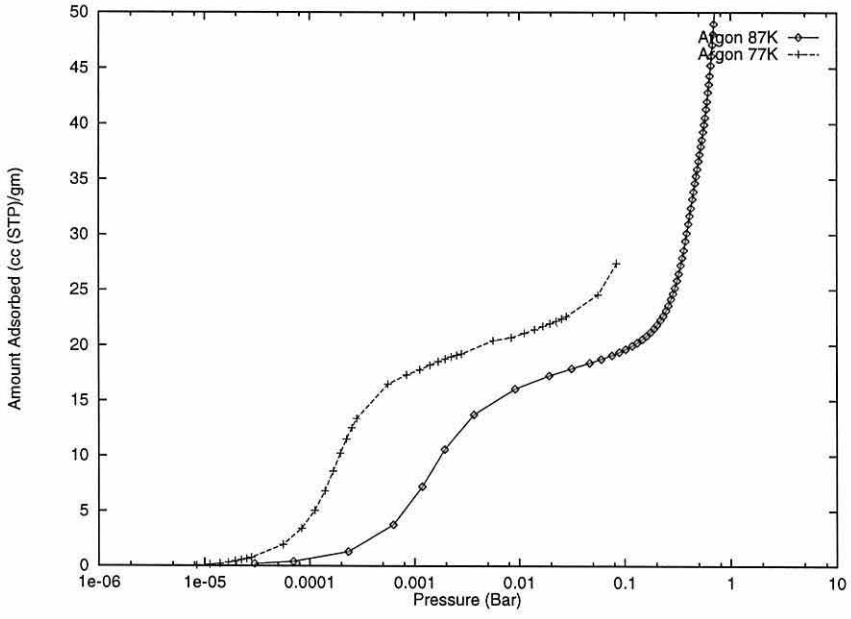

4.3 Theoretical Adsorption Isotherms

Theoretical adsorption isotherms of nitrogen, argon and methane for a model non-porous surface were calculated at 77K using non-local density functional theory (Section 2.3). The adsorption of nitrogen, argon and methane in a single pore with a physical width [Appendix B] of H^*_{phys}= 100 (357.2Å for nitrogen, 341Å for argon, 381Å for methane) was calculated. With a pore width of this size there is no appreciable interaction from opposite pore walls and the adsorption isotherm is therefore representative of a flat carbon surface as found in Vulcan, Sterling or graphite.

A Grand Canonical Ensemble (Section 2.2.5) describes this system. The adsorption isotherms are calculated for a specified volume (the physical pore width, H^*_{phys}= 100), temperature, T =77K and a series of pressures, P. The pressure values are chosen so as to cover the same range recorded in the experimental isotherm. The pressure is related to the chemical potential via the *virial equation of state* for the compression factor of a gas as an infinite series expansion in the density:

$$\frac{P}{\rho RT} = 1 + B_2^T\rho + B_3^T\rho^2 + \cdots \tag{4.4}$$

Where P is the pressure, R is the ideal gas constant, T is the temperature, ρ is the molar density and B_n^T is the n_{th} virial coefficient.

The virial coefficients depend only on temperature and the gases intermolecular forces. The second virial coefficient is related to the interactions between isolated pairs of molecules:

$$B_2^T = -2\pi N_A \int_0^\infty [exp(-U(r)/kT) - 1]r^2 dr \tag{4.5}$$

Where $U(r)$ is the intermolecular potential, N_A is Avogadro's constant, k is Boltzmann's constant, T is the temperature and r is the separation between the atomic centres.

Re-writing (4.5) in reduced units [Appendix B]:

$$B_2^{*^T} = -2\pi \int_0^\infty [exp\{-\frac{4}{T^*}\left(\frac{1}{r^*}\right)^{12} - \left(\frac{1}{r^*}\right)^{6}\} - 1]r^{*2} dr^* \tag{4.6}$$

Where $T^* = kT/\epsilon_{ff}$, $r^* = r/\sigma_{ff}$ and σ_{ff} is equal to the molecular diameter. The chemical potential μ is related to the second virial coefficient:

$$\mu^* = T^* ln\Big[\frac{\rho^*}{exp(2B_2^{*T}\rho^*)}\Big] \tag{4.7}$$

The density, ρ^* is expressed in reduced units and is dimensionless. The second virial coefficient for each gas at the specified temperature, and the chemical potentials corresponding to a series of pressure values (covering the range recorded in the experimental adsorption isotherms) were calculated. The ideal density, non-ideal density, ideal chemical potential and non-ideal chemical potential can also be calculated as they are related to $B_2^{*^T}$.

The chemical potentials and their corresponding pressure values are used to calculate the equilibrium density profile, $\rho_{eq}(r)$ of a Lennard-Jones fluid confined within a carbon slit-pore (Section 2.3). The density of adsorbate in the pore is calculated at each specified pressure value to give an adsorption isotherm.

The specific surface areas calculated by the BET method earlier are used to convert the specific density of adsorbate to a specific volume at STP [Appendix C]. This allows comparison between the theoretical and experimental adsorption isotherms.

4.3.1 Fitting Procedure

The solid-fluid and fluid-fluid interaction parameters were adjusted until the theoretical and experimental isotherms for the adsorption of nitrogen, argon and methane onto Vulcan at 77K crossed in the middle. The resulting parameters are listed in Table 4.6.

We first investigate the dependence of the monolayer completion pressure and the knee point, V_B on these parameters. Several adsorption isotherms were calculated where the value of one parameter was varied in turn whilst all other parameter values remained constant.

Table 4.6: *Interaction potential parameters of Non-Local Density Functional Theory model.*

Parameter	N-N	Ar-Ar	CH_4-CH_4
$\sigma_{ff}(\AA)$	3.572	3.410	3.810
$\sigma_{sf}(\AA)$	3.486	3.405	3.605
$\epsilon_{ff}/k(\mathbf{K})$	93.98	119.8	148.1
$\epsilon_{sf}/k(\mathbf{K})$	53.46	54.86	57.96

4.3.2 Dependence of Methane Monolayer Completion Pressure on ϵ_{sf}/k, ϵ_{ff}/k, R_c and σ_m

The parameters; ϵ_{ff}/k, R_c and σ_m were set to constant values of 148.1K, 5.0σ, and 3.81 $\mathring{A}$ respectively. An adsorption isotherm was then calculated for several values of ϵ_{sf}/k in the range 51 to 58K. This range of values was chosen as it covers the range of values for the parameter ϵ_{sf}/k for all three gases [Table 4.6].

The larger the value of ϵ_{sf}/k, the lower the pressure at which the monolayer is completed. When ϵ_{sf}/k is large, the potential energy well is deep, and the attractive force between the solid and fluid molecules is stronger, less gas pressure is therefore required for the fluid molecules to adsorb onto the surface and form a monolayer. The strength of the solid-fluid interaction has little affect on the steepness of the gradient in the monolayer formation region (Fig 4.14).

With $\epsilon_{sf}/k = 50.12$, $R_c = 5.0\sigma$, and $\sigma_m = 3.81\mathring{A}$, (i.e. values listed in the literature for methane) the value of ϵ_{ff}/k was varied between 100 and 150K and an adsorption isotherm was calculated for each set of parameters. This range covers the values listed in the literature for adsorbates nitrogen, argon and methane. The parameter, ϵ_{ff}/k, has no significant affect on the pressure at which the monolayer completes, this point being at 10^{-4} Bar in all cases. However, the parameter does affect the steepness of the gradient in the monolayer formation region. The larger the value the steeper the gradient (Fig 4.15). This can be explained qualitatively as the greater the value of ϵ_{ff}/k the stronger the interaction between fluid molecules on the surface of the material to form a monolayer.

Figure 4.14: *Dependence of Gradient of Methane Monolayer on* ϵ_{sf}/k.

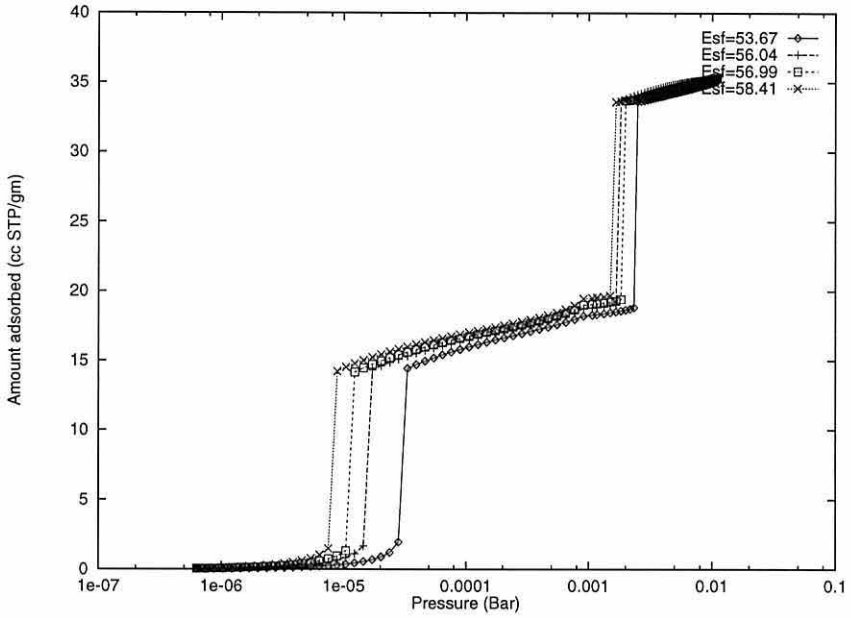

Figure 4.15: *Dependence of Gradient of Methane Monolayer on* ϵ_{ff}/k.

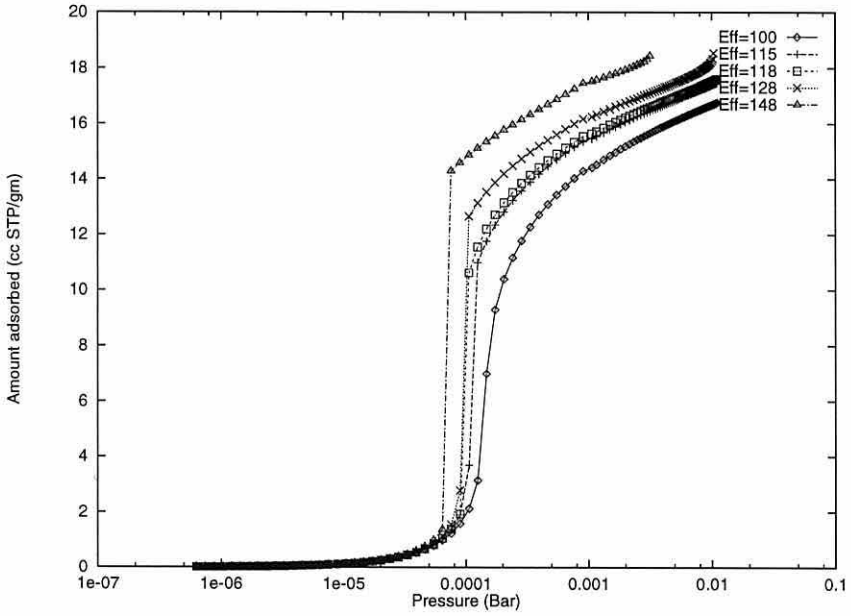

With ϵ_{sf}/k = 53.67K, ϵ_{ff}/k = 148.1K, and σ_m = 3.81$\mathring{A}$, adsorption isotherms were calculated for a series of different cut-off distances (2.5σ, 3.0σ, 4.0σ, 5.0σ, 6.0σ, and 1 x10$^{12}\sigma$). The cut-off distance has no appreciable affect on the pressure region over which the monolayer is formed and confirms that our standard choice of 5σ for the maximum range at which molecules interact is large enough not to adversely affect the results.

With ϵ_{sf}/k set constant at 57.94K, ϵ_{ff}/k = 148.1K, and R_c = 5.0σ, the molecular radius σ_m was varied between 3.4$\mathring{A}$ and 4.0$\mathring{A}$ and an adsorption isotherm was calculated in each case. The larger the value of the molecular diameter the lower the pressure at which the monolayer is completed. The monolayer completion pressure is almost proportional to the reciprocal of the molecular radius squared (Fig 4.16), as might be expected since the molecular cross section and hence the amount of area it occupies on the surface will be proportional to σ_m^2.

Figure 4.16: *Dependence of Methane Monolayer Completion Pressure on* $1/\sigma_r^2$.

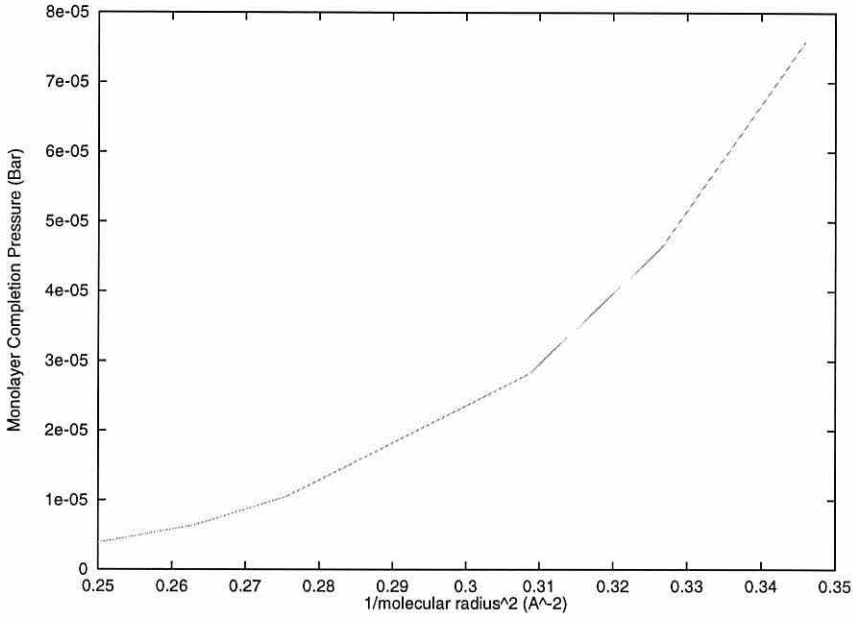

4.3.3 Dependence of 'knee-point', V_B, on ϵ_{sf}/k, ϵ_{ff}/k, R_c and σ_m

Using the same values for the parameters outlined in Section 4.3.2 where ϵ_{sf}/k is varied, the knee-point value marking the monolayer volume was measured on each isotherm.

The value of ϵ_{sf}/k has no systematic effect on the monolayer volume. This is to be expected since the solid-fluid interaction produces a force normal to the surface and once the monolayer has formed it is only forces tangential to the surface that can affect the separation between neighbouring molecules and hence the surface molecular density and monolayer volume.

The parameter ϵ_{ff}/k was varied between 100 and 148K whilst the other param-

eters remained constant. As the value of ϵ_{ff}/k increases so does the volume of the monolayer (Fig 4.17). It follows that the interaction between the fluid molecules is an important factor in the formation of the monolayer. The larger the value of ϵ_{ff}/k, the greater the attractive forces between the fluid molecules and therefore the molecules in the monolayer are packed closer together resulting in more adsorption and a higher knee-point value. The monolayer volume is close to proportional to ϵ_{ff}/k over this range of values. The intermolecular forces are proportional to ϵ_{ff}/k.

Fractional differences in average monolayer volume due to changes in the cut-off distances are small. However, the monolayer volume increases monotonically with increasing R_c up to a value of 5.0σ or so (Fig 4.18). Interactions at distances greater than 5.0σ contribute little to the potential energy and as a result the difference in the monolayer capacity becomes negligible for greater cut-offs. This is consistent with a lack of dependency of monolayer completion pressure for our choice of R_c (Section 4.3.2).

In order to minimise computing time, any interactions at distances greater than 5.0σ are not reported below. Also, changing the molecular diameter does not systematically affect the value of the calculated monolayer volume to any appreciable extent (Fig 4.19).

Figure 4.17: *Dependence of V_B on ϵ_{ff}/k.*

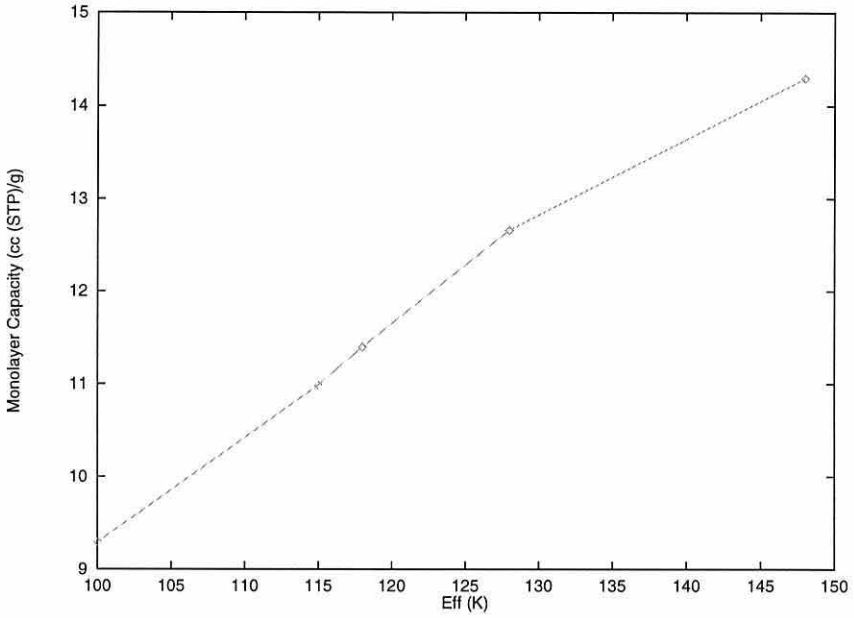

Figure 4.18: *Dependence of V_B on R_c.*

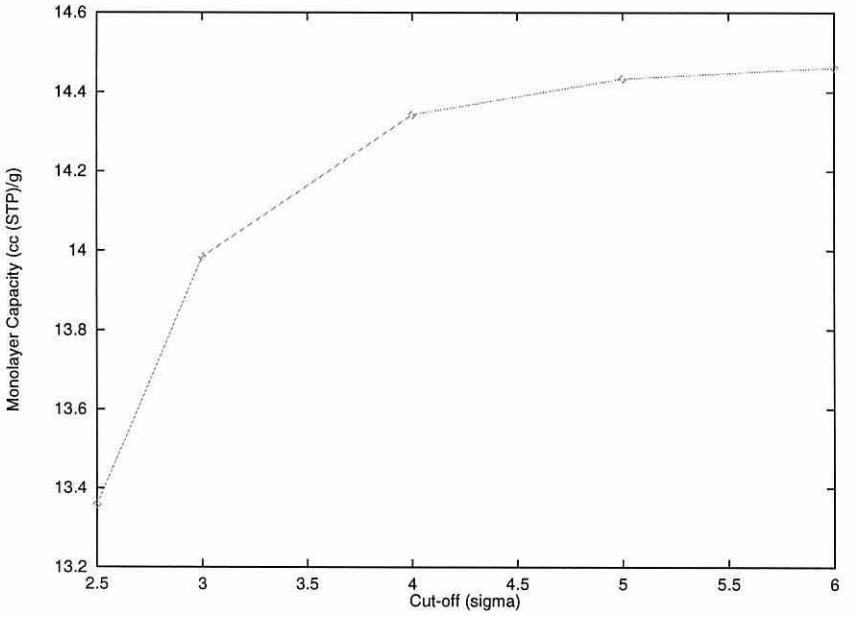

Figure 4.19: *Dependence of V_B on σ_m.*

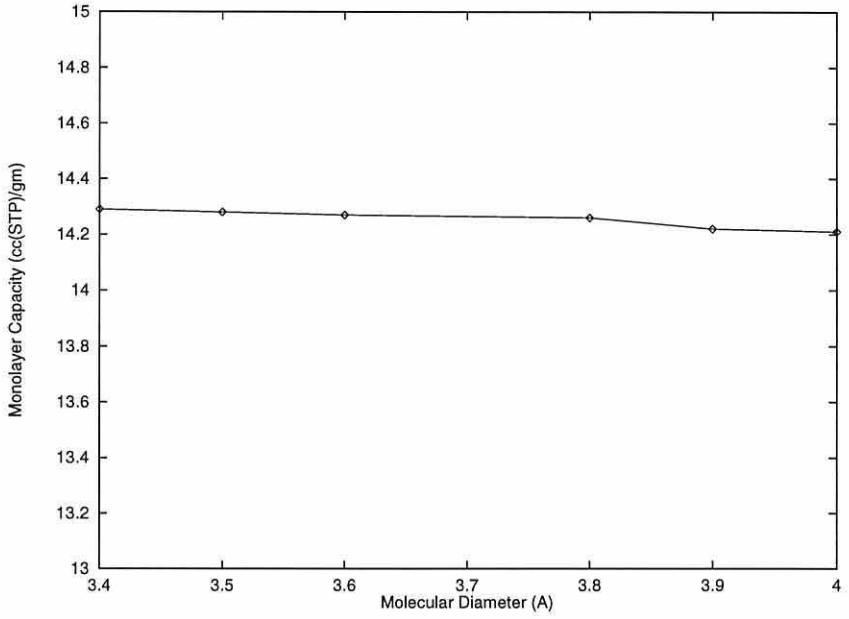

4.3.4 Semi-empirical adsorption isotherms from non-local density functional theory

The best fit to the nitrogen adsorption isotherm using non-local density functional theory is shown in Fig 4.20 with error-bars on the experimental data. Over most of the isotherm the non-local theory gives an isotherm with adsorption within 10 per cent of the observed amount over the pressure range the experimental isotherm covers. Lastoskie showed [83] a similar fit to the adsorption of nitrogen on Vulcan using non-local theory, obtaining a value of 53.22K for the parameter ϵ_{sf}/k.

The interaction potential parameters for the fitted non-local density functional theory isotherms to Vulcan for argon and methane adsorption at 77K have not previously been calculated. The best fits to the Vulcan isotherms for argon and methane adsorption are shown in Figs 4.21 and 4.22 respectively.

The same solid-fluid and fluid-fluid interaction parameters [Table 4.6] are used for the fits to the 3 different materials (when the adsorbate molecule is the same). The 3 materials are all low surface area carbons as they yield Type II isotherms but they adsorb different amounts.

The non-local density functional isotherms obtained from using the parameters in [Table 4.6] were also compared with the experimental isotherms for nitrogen, argon and methane adsorption on Sterling and nitrogen and argon on graphite (Fig 4.23 to Fig 4.27), including error-bars on the experimental data. The fits follow the shape of the experimental isotherms, however there is a clear difference in magnitude as a result of the lower surface areas of Sterling and graphite which act as a scaling factor (the value of the surface area is used in converting the excess density into appropriate units [Appendix C]). Independent sets of potential parameters were also evaluated by a similar fitting individually for Sterling and graphite. However, it was shown that those parameters found for gases adsorbing on the surface of Vulcan already represent the best possible choice. Thus the same solid-fluid interaction parameters have been used for the fit to the three different materials. This finding supports the notion that despite different amounts adsorbed, the surfaces do not significantly differ in their microstructure approximated as a flat graphite sheet with no defects. In this respect the relatively large surface area of Vulcan compared with Sterling or graphite has an added advantage in the lower experimental error, however, this does not affect the quality of the fitting scheme (the same parameters are used) on Sterling or graphite. Despite physical differences (surface area, x-ray diffraction patterns (Section 4.2.7), surface images (Section 4.2.7) Vulcan is already a good

approximation of a flat graphite surface and its general utilisation for potential parameters evaluation is well justified.

For this choice of parameters there is a region at low pressures where DFT underpredicts and at high pressures where it overpredicts the amount of gas adsorbed. Although we can predict a single part of the curve we lose on the fit in the other regions. The low pressure region of an isotherm for a microporous adsorbent corresponds to the filling of micropores and is therefore primarily of interest in this thesis for prediction of the surface pore size distributions (see Chapter 5).

Figure 4.20: *Fit To Vulcan for Nitrogen Adsorption.*

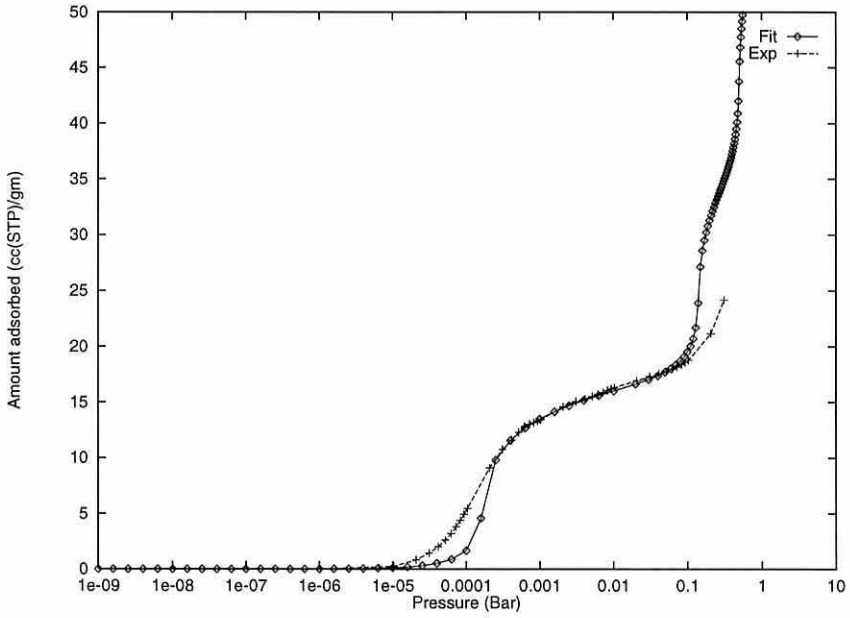

Figure 4.21: *Fit To Vulcan for Argon Adsorption.*

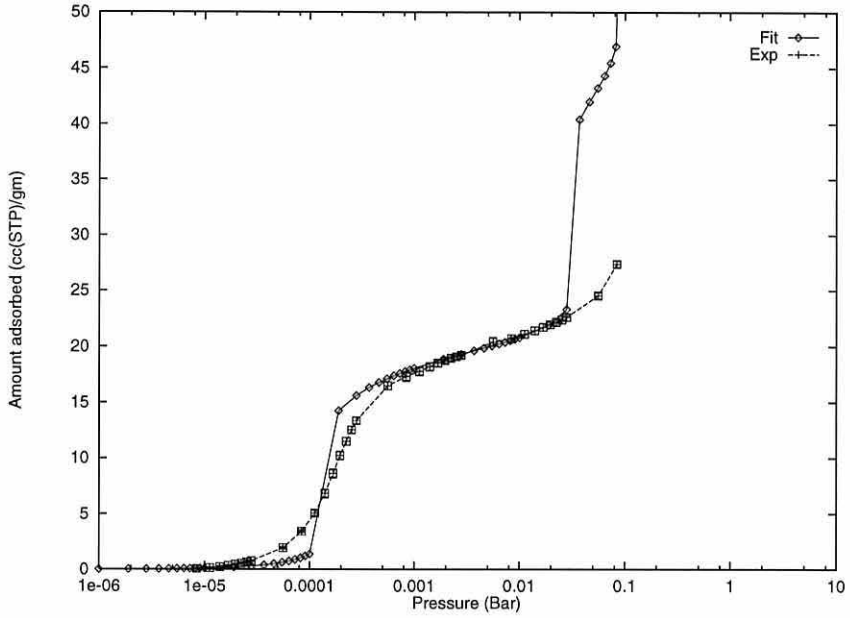

Figure 4.22: *Fit To Vulcan for Methane Adsorption.*

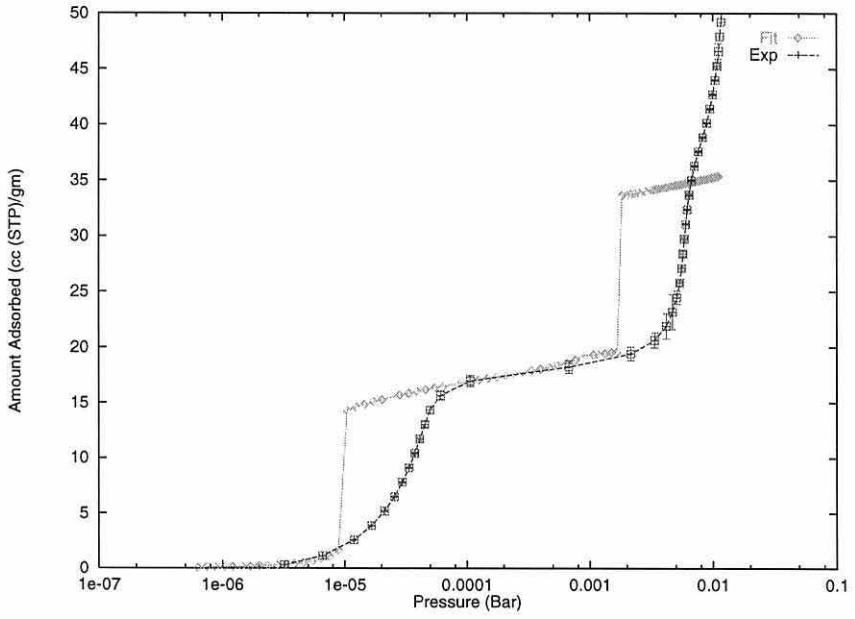

Figure 4.23: *Fit To Sterling for Nitrogen Adsorption.*

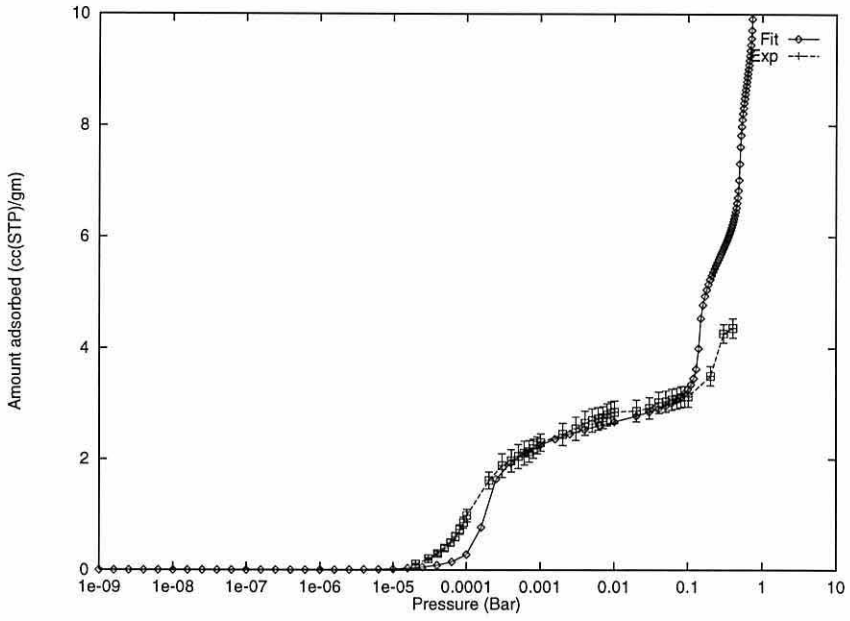

Figure 4.24: *Fit To Sterling for Argon Adsorption.*

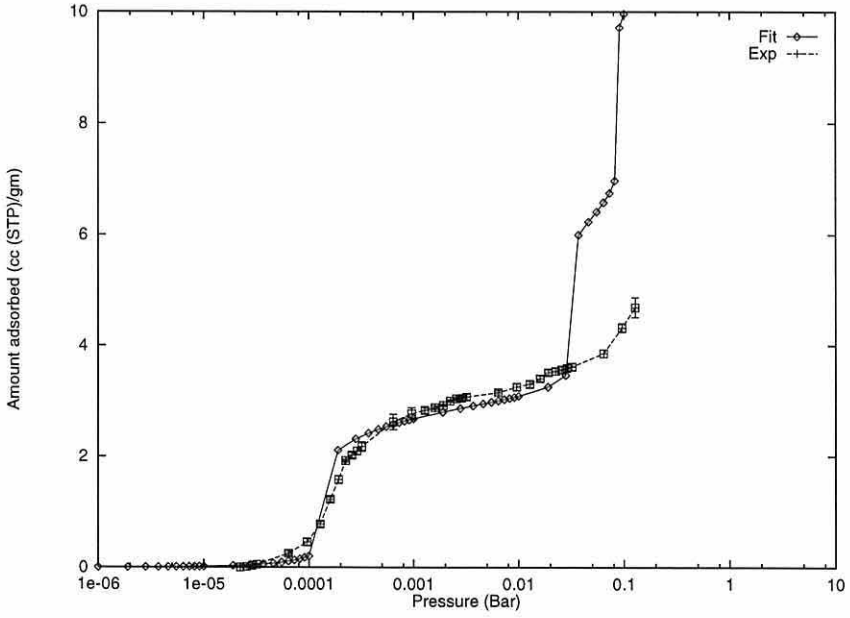

Figure 4.25: *Fit To Sterling for Methane Adsorption.*

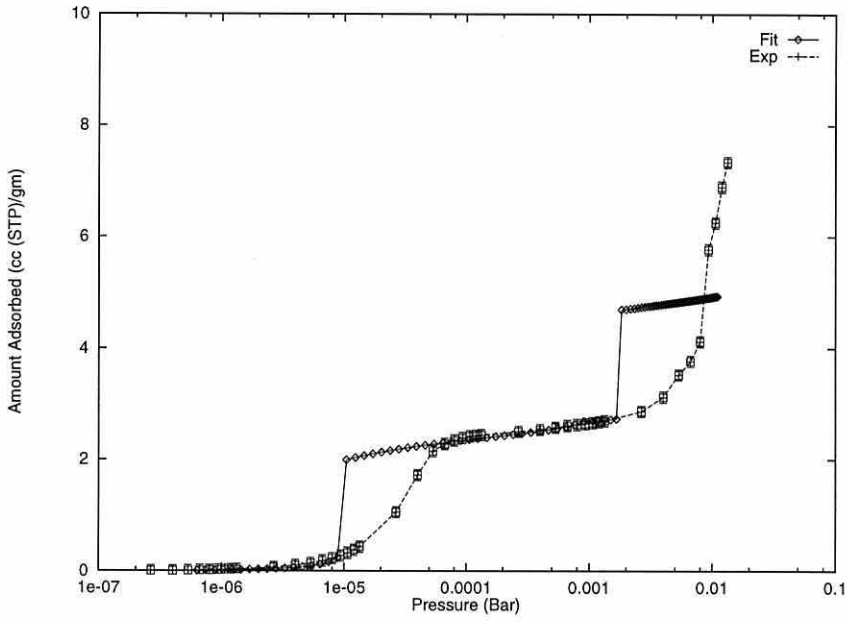

Figure 4.26: *Fit To Graphite for Nitrogen Adsorption.*

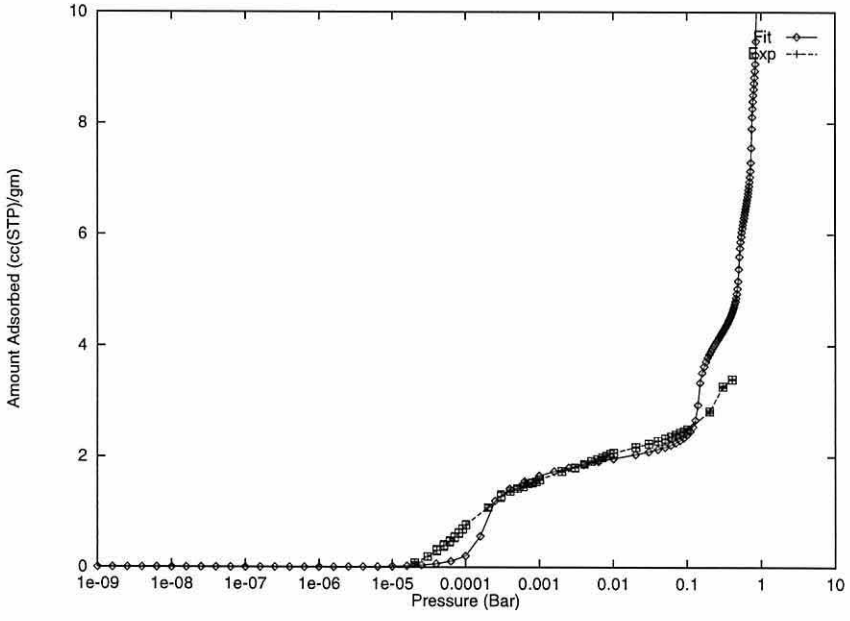

Figure 4.27: *Fit To Graphite for Argon Adsorption.*

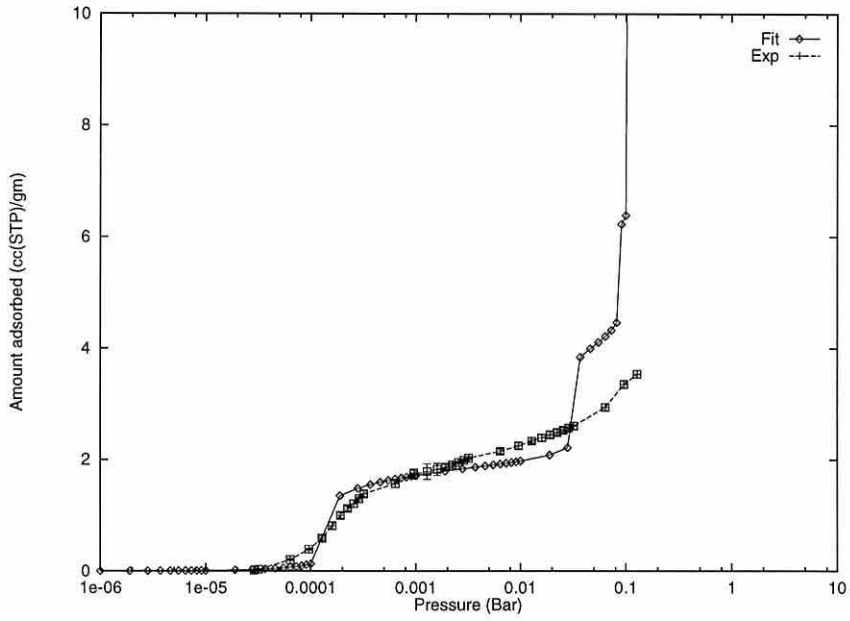

4.4 Adsorption Measurements at Room Temperature

Experimental adsorption isotherms of nitrogen, methane, and carbon-dioxide onto Vulcan were measured at room temperature using the static flow method. A constant temperature of 293K was maintained throughout the measurements by immersing the sample and reference tubes in a temperature controlled water bath.

The saturation vapour pressure for the adsorbates nitrogen, carbon-dioxide and methane are not measurable at room temperature because measurements are limited to pressures less than 1 Bar and these molecules remain in the gas phase at this temperature and pressure.

The adsorption of nitrogen, carbon-dioxide and methane onto Vulcan has not

previously been measured at room temperature over this pressure range. Here we show adsorption measurements over the pressure range $1.9x10^{-2}$ to 1.0 Bar. The experiments were repeated several times, for each adsorbate, in order to ensure reproducibility and to calculate mean adsorption isotherms. A fresh sample of Vulcan was used in each experiment but each sample was taken from the same batch (Section 4.2) and degassed at 573K for approximately 20 hours. An adsorption dose of 5 Torr was used throughout.

The mean adsorption isotherms of nitrogen, carbon-dioxide and methane onto Vulcan at 293K are compared in Fig 4.28.

Figure 4.28: *Mean Adsorption of Nitrogen, Carbon-Dioxide and Methane onto Vulcan at 293K.*

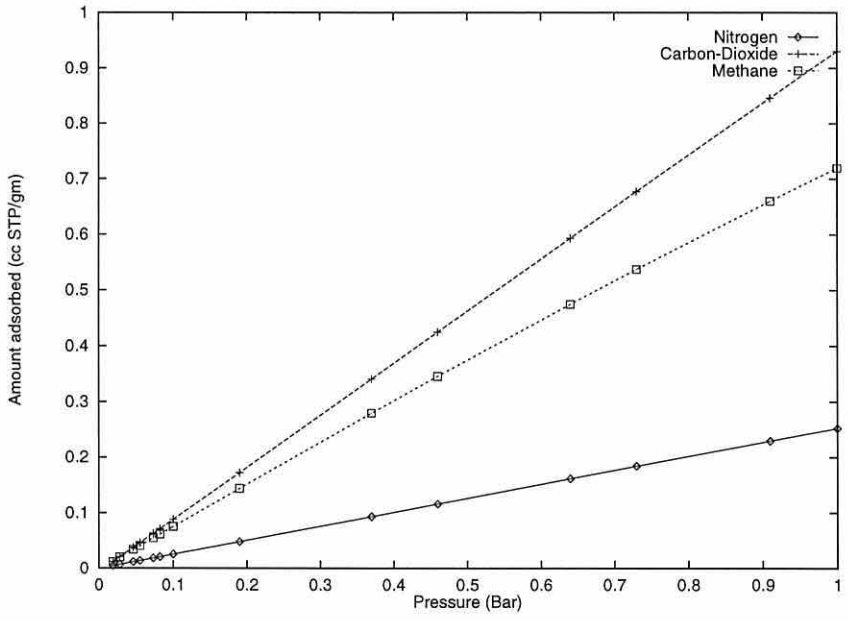

On a logarithmic pressure scale, the isotherms are convex to the pressure axis but on a normal pressure scale the adsorption is almost linear with pressure (Fig 4.28).

The amount of adsorption varies between the 3 gases. Carbon-dioxide is most readily adsorbed, nitrogen is least readily adsorbed and the differences increase with the amount adsorbed. Over this pressure range and at this temperature a monolayer is not able to form. Instead, the vapour evaporates from the surface before a monolayer is formed because the greater kinetic energy of the molecules at this temperature is greater than the potential energy needed to escape the solid surface.

4.5 Theoretical Adsorption Isotherms

Theoretical adsorption isotherms of nitrogen, carbon-dioxide and methane on a model non-porous surface were calculated at 293K using non-local density functional theory. A single pore with a physical width of $H^*_{phys} = 100$ (357.2$\AA$ for nitrogen, 391$\AA$ for carbon-dioxide, and 381$\AA$ for methane) was used in the model to represent a non-porous carbon surface such as Vulcan.

As discussed in (Section 2.2.5), a Grand Canonical Ensemble describes the system, and the densities were calculated over the pressure range of the experimental isotherm.

4.5.1 Fitting Procedure

The solid-fluid and fluid-fluid interaction parameters (ϵ_{sf}/k and ϵ_{ff}/k) were adjusted until the closest least squares fit was attained between the theoretical and experimental adsorption of nitrogen, carbon-dioxide and methane on Vulcan at 293K (Fig 4.29), with error-bars on the experimental data. The interaction potential parame-

Figure 4.29: *Fit to Vulcan for Nitrogen, Carbon-Dioxide and Methane Adsorption.*

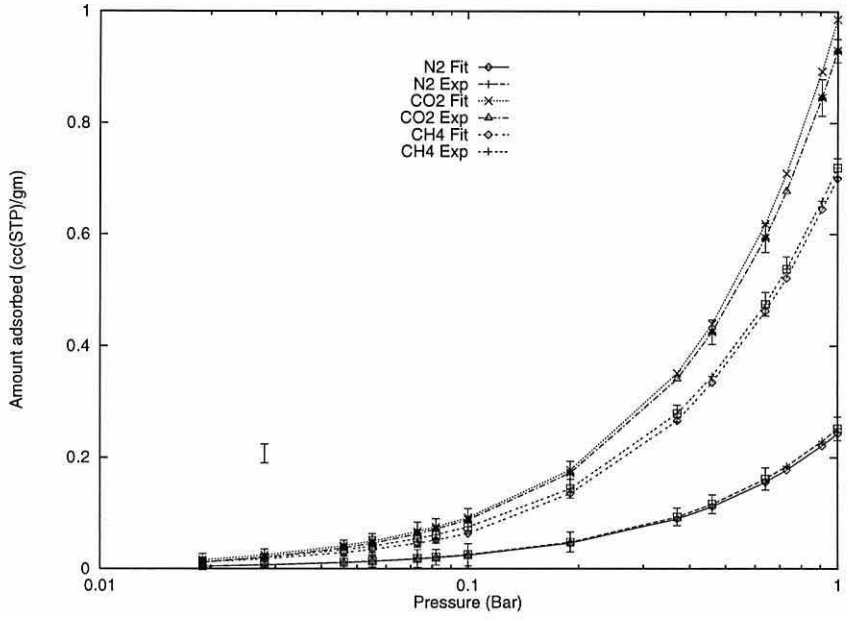

ters are listed in Table 4.7. A comparison of the amount of nitrogen and methane adsorbed at 293K shows that although the amount of nitrogen is much lower, the parameter ϵ_{sf}/k has a similar value (to within 9 per cent).

Table 4.7: *Interaction potential parameters of non-local density Functional Theory model.*

Parameter	N-N	CO_2-CO_2	CH_4-CH_4
$\sigma_{ff}(\AA)$	3.572	3.910	3.81
$\sigma_{sf}(\AA)$	3.486	3.66	3.605
$\epsilon_{ff}/k(\mathbf{K})$	105.0	165.0	148.1
$\epsilon_{sf}/k(\mathbf{K})$	54.47	67.97	64.4

σ_{ff} is the fluid-fluid molecular diameter (Angstroms) and σ_{sf} is the solid-fluid molecular diameter (Angstroms).

At the same pressure values, the experimentally measured uptake of carbon-dioxide was greater than the uptake of methane which in turn was greater than the uptake of nitrogen on Vulcan (Fig 4.28). The relative differences between the amounts adsorbed for different gases increases as the pressure increases.

Interactions between adsorbing molecules are strongly affecting the amount of adsorption. The relative magnitudes of the interaction parameters for the 3 gases in Table 4.7 may explain the experimental differences in adsorption. Both the surface fluid interaction (ϵ_{sf}/k) and the fluid-fluid interaction (ϵ_{ff}/k), are largest for molecules which produce the larger amount of adsorption.

We investigate whether similar changes in ϵ_{sf}/k and ϵ_{ff}/k alone can produce similar differences in adsorption. The parameter ϵ_{sf}/k was set at values between 50 and 70K, with ϵ_{ff}/k=165.0K, R_c= 5.0σ and σ_m= $3.91\mathring{A}$ and an adsorption isotherm was calculated in each case (Fig 4.30). It is evident that the larger the value of ϵ_{sf}/k the greater the density of adsorbate at a particular pressure value - suggesting that the solid-fluid interaction can play an important role over this pressure region.

Figure 4.30: *Effect of ϵ_{sf}/k on Adsorption.*

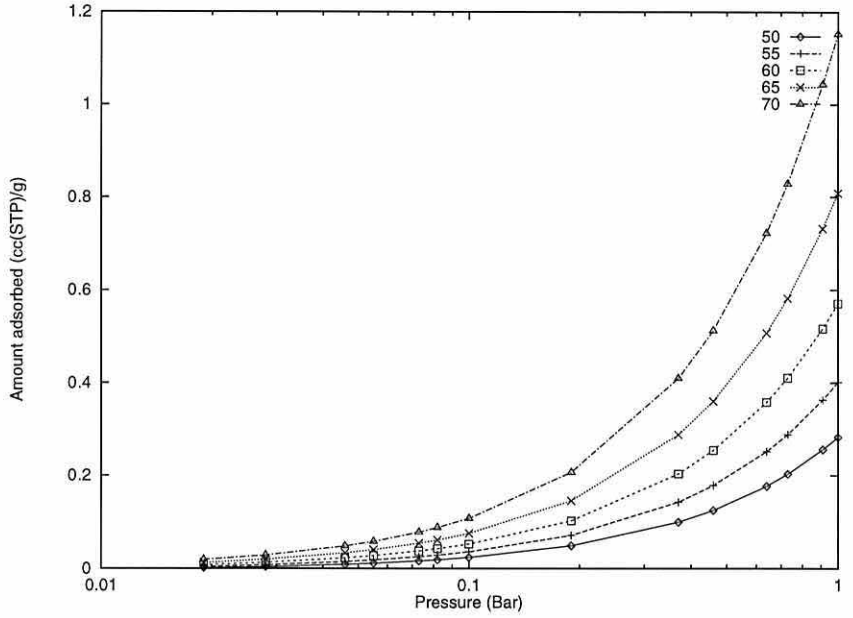

With ϵ_{sf}/k set at a value of 67.97K, R_c= 5.0σ, and σ_m=3.91$\mathring{A}$, ϵ_{ff}/k was set at values between 100 and 150K, and an adsorption isotherm was calculated in each case (Fig 4.31).

The parameter ϵ_{sf}/k is related to the density through Equation (4.2). ϵ_{ff}/k has no significant effect on the gas uptake at high temperatures and pressures below 1 Bar.

Figure 4.31: *Effect of ϵ_{ff}/k on Adsorption.*

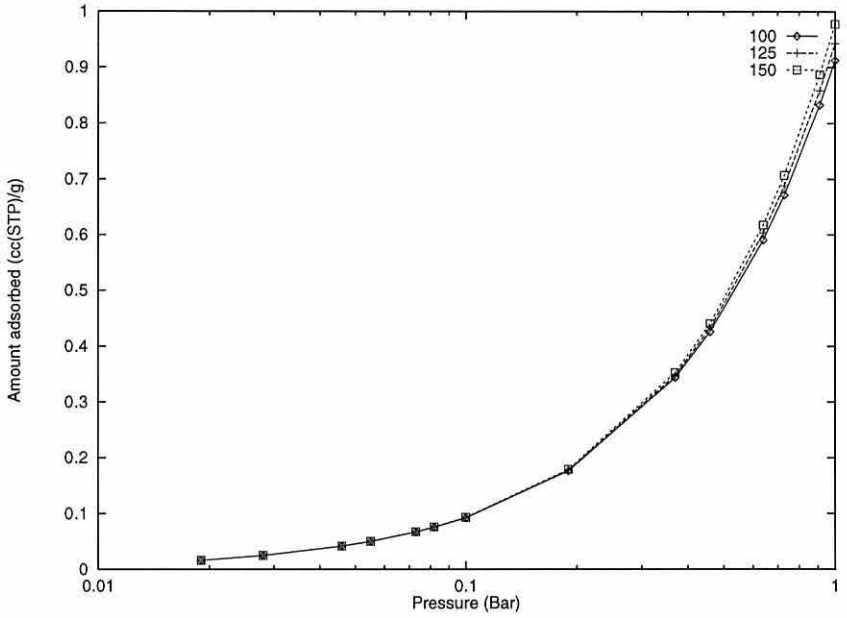

4.5.2 Conclusions

The non-local density functional theory fits to the experimental Vulcan isotherms for nitrogen, argon and methane at 77K are generally a good approximation. For pressures less than 0.1Bar the fit is semi-quantitative.

Although it predicts a monolayer at about the right pressure, the non-local theory gives the worse fit in the region where the monolayer is formed. This is more apparent the steeper the gradient of the curve in the monolayer formation region i.e. the sharper the transition to the monolayer state as pressure is increased.

The non-local theory isotherms obtained from fitting to Vulcan are compared with the experimental isotherms for nitrogen, argon and methane adsorption on Sterling (Figs 4.23 to 4.25) and nitrogen and argon on graphite (Figs 4.26 and 4.27). As observed with the fits to Vulcan, the region over which the monolayer forms is the

most difficult to model accurately, although here again DFT successfully predicts the monolayer formation.

As observed experimentally on Vulcan (Fig 4.1) the uptake of methane as predicted by DFT is greater than that for nitrogen and argon. At low pressures, the predicted uptake of argon is lower than that of nitrogen. This is also observed in the experimental uptake of argon and nitrogen onto Vulcan (Fig 4.1), Sterling (Fig 4.3) and graphite (Fig 4.4). A crossing point occurs at $1x10^{-4}$ Bar in the nonlocal theory, $1.4x10^{-4}$ Bar on Vulcan, $1.3x10^{-4}$ Bar on Sterling and $2x10^{-4}$ Bar on graphite. The DFT therefore successfully predicts crossing points of the isotherms.

The differences between the experimental adsorption curves at 77K can be explained largely in terms of the magnitude of the fluid-fluid and solid-fluid interaction parameters obtained [Table 4.6] for the theoretical isotherms.

The larger the value of ϵ_{sf}/k the lower the pressure at which the monolayer forms (Fig 4.14). The parameter ϵ_{sf}/k is determined from the Lorentz-Berthelot combining rules [Appendix A]. As the value of the parameter ϵ_{ss}/k is the same in all three cases (they are all carbons) the difference in the determination of ϵ_{sf}/k lies in the values of the parameter ϵ_{ff}/k which are taken from the literature and determined from molecular beam experiments and equations of state [19].

Methane adsorption occurs much more readily than adsorption of argon or nitrogen onto Vulcan. Referring to [Table 4.6] the magnitude of the ϵ_{sf}/k parameter values reflect this behaviour; the methane monolayer completes at much lower pressures than monolayers of argon or nitrogen. The solid-fluid interaction parameter values for nitrogen and argon differ by less than 50percent. The larger value of

ϵ_{sf}/k for methane implies that the attractive forces between the methane and carbon molecules are stronger than those between the argon and carbon or nitrogen and the carbon surface. Hence, less gas pressure is required to force methane molecules to adsorb onto the surface of Vulcan.

The pressure at which the monolayer forms is also related to the molecular diameter of the adsorbate molecule (Fig 4.16); the larger the molecular diameter the lower the pressure. This corresponds to the observed experimental results for the three adsorbates on Vulcan (Fig 4.1). The size of the molecular diameter and magnitude of the ϵ_{sf}/k parameter are therefore both important in determining the pressure at which the monolayer forms.

Experimental adsorption isotherms at room temperature and up to atmospheric pressure are difficult to measure. The adsorption is linear (Fig 4.28) and a monolayer cannot form under a combination of low pressures (below 1.0 Bar) and a high temperature (293K). These conditions are analogous to the low pressure part of an isotherm measured at 77K. Adsorbate molecules at 293K have a greater kinetic energy and therefore evaporate from the surface of the adsorbent before a monolayer can properly form.

Although Vulcan and Sterling are commonly referred to as non-porous materials they do possess some degree of porosity. The experimental uptake of adsorbates at low pressure ($1x10^{-4}$ Bar and below for nitrogen and argon on Vulcan) and ($1x10^{-5}$ Bar and below for methane on Vulcan) corresponds to the filling of pores present on the surface of the material. However, there is no practical method of determining these very sparse pore size distributions. In the low pressure region the interaction

between the adsorbent and adsorbate (ϵ_{sf}/k) is more significant than the adsorbate - adsorbate interactions (ϵ_{ff}/k) which become more important to the formation of the monolayer (Section 4.3.3). The difference in surface area values for the three adsorbents is at least partly explained by their relative particle sizes, determined from SEM and X-ray diffraction studies. Vulcan was found to have a smaller particle size than Sterling, consequently a larger BET surface area value was obtained from gas adsorption experiments for Vulcan than Sterling. Graphite was shown to be composed of large slabs also leading to a smaller surface area than Vulcan. Results from x-ray diffraction experiments confirmed that Vulcan is composed of smaller particles than Sterling or graphite.

The interaction potential parameters obtained from the non-local DFT theory and the experimental Vulcan isotherm data at 77K and 293K [Tables 4.6 and 4.7] will be used in the next chapter to generate a database of adsorption isotherms for pores of different physical width at these temperatures. The resulting database of model adsorption isotherms covering a range of physical pore widths can then be used to construct an adsorption isotherm for a porous or 'active' carbon. The heterogeneity found in a porous carbon is modelled by a collection of isotherms for a wide range of physical pore widths. A linear combination of these isotherms can then be used to reconstruct an experimental adsorption isotherm of a porous carbon. This is used to determine the pore size distribution of an active carbon and is the subject of the next chapter.

Chapter 5

Porous Carbons

5.1 Introduction

This chapter is concerned with the adsorption of gases onto micro-porous or 'active' carbons at constant temperature, and determination of their pore size distributions.

A method of pore size distribution analysis of carbon surfaces has been applied based on density functional theory. In recent years methods of pore size distribution (PSD) analysis have been used routinely at 77K from nitrogen adsorption experiments. In this work, PSD analysis of the adsorption of nitrogen on four different carbon materials was shown to give results consistent with their experimentally determined adsorption isotherms as well as results in agreement with a similar approach in the literature [46]. Therefore the method may be used as a general method for PSD determination of carbon surfaces [18]. This general approach has been extended in this thesis by considering gases other than nitrogen at 77K and also higher temperatures (293K) [17].

Experimental adsorption isotherms of nitrogen on active carbons; AX21, Norit, Pica and Supersorbon were measured [17] volumetrically at 77K. The adsorption of argon and methane onto active carbon AX21 and argon on Supersorbon were also measured at 77K. Similar isotherms for the adsorption of nitrogen, carbon-dioxide and methane onto active carbon AX21 were measured at room temperature. The Coulter Omnisorp 100cx apparatus (Fig 3.1) was used throughout. The specific surface area of the active carbons was calculated from the experimental adsorption data using the BET method (Section 4.2.4). Theoretical isotherms for active carbons are calculated from a DFT model for the adsorption of nitrogen, argon and methane at

77K and nitrogen, carbon-dioxide and methane at 293K in model slit-shaped pores ranging from 6 to 1000$\AA$.

Estimates of the surface pore size distribution (PSD) and total pore volumes of carbons are made from density functional theory.

5.2 Experimentally Measured Isotherms

5.2.1 Gas adsorption onto microporous carbons at 77K

To ensure reproducibility, the adsorption of nitrogen onto AX21, Norit, Pica and Supersorbon was measured repeatedly at regular intervals up to a cut-off pressure of 1.0 Bar. These particular carbons were used as they were available at the time. The mean adsorption isotherms are shown in (Fig 5.1). All four materials yield Type I isotherms (the filling of micropores occurs at low pressures <0.1 Bar and the adsorption process is complete at approximately 0.5 Bar where the isotherm branch flattens) suggesting that they are microporous in nature.

The initial uptake of nitrogen at low pressures, in the monolayer formation region is largest for AX21. The other 3 isotherms are similar in this region. The magnitude of adsorption in the monolayer formation region is most similar for adsorbents Pica and Supersorbon. The pressure at which the monolayer completes is located at approximately $4x10^{-4}$ Bar for all four adsorbents.

Figure 5.1: *Adsorption isotherms of Nitrogen onto AX21, Norit, Pica and Supersorbon on a logarithmic pressure scale.*

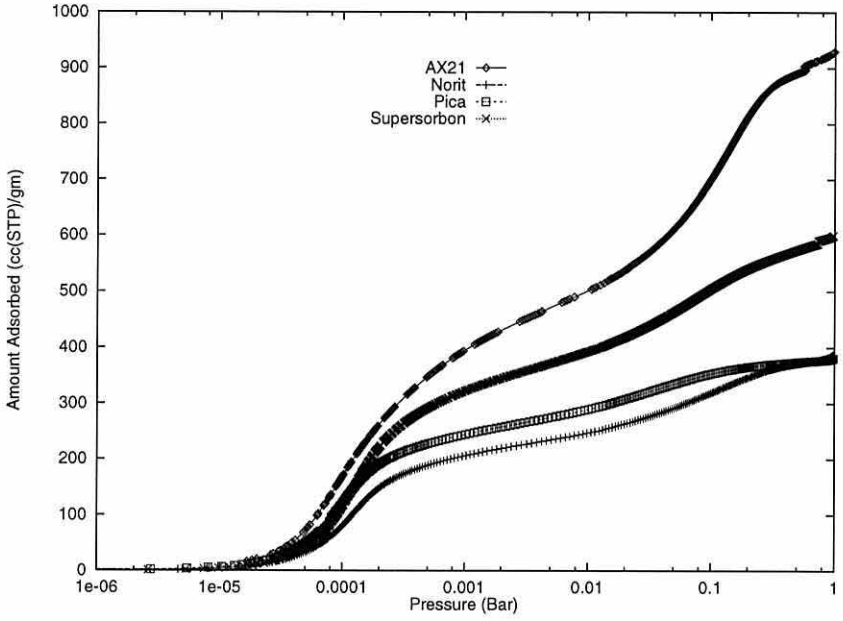

The mean adsorption isotherms of argon on AX21 and Supersorbon are shown (Fig 5.2). Experiments were also repeated to ensure reproducibility, and as with nitrogen adsorption, the isotherms are Type 1.

There is a greater uptake of argon on AX21 than on Supersorbon at the same pressure, this difference was also observed with the adsorption of nitrogen (Fig 5.1) and suggests that AX21 is more microporous than Supersorbon.

Figure 5.2: *Adsorption isotherms of Argon on AX21 and Supersorbon on a logarithmic pressure scale.*

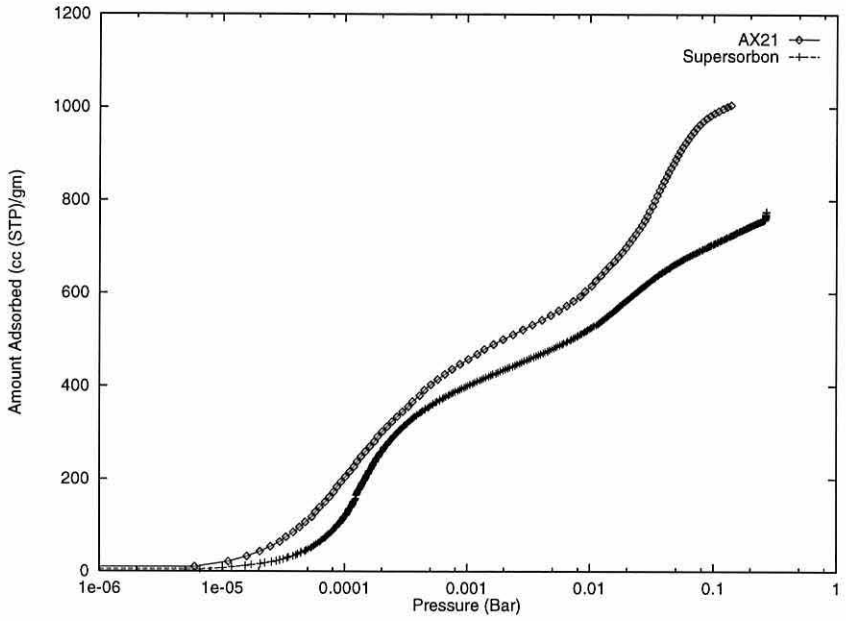

Adsorption of 3 gases onto AX21 is shown in Fig 5.3. All three adsorption isotherms have a similar shape, although methane is adsorbed at the lowest pressures.

At low pressures (10^{-6} to 10^{-5} Bar) there is little adsorption for all three gases and then there is a sharp increase in adsorption with pressure increase at approximately $5x10^{-5}$ Bar.

Figure 5.3: *Gas Adsorption onto AX21 on a logarithmic pressure scale.*

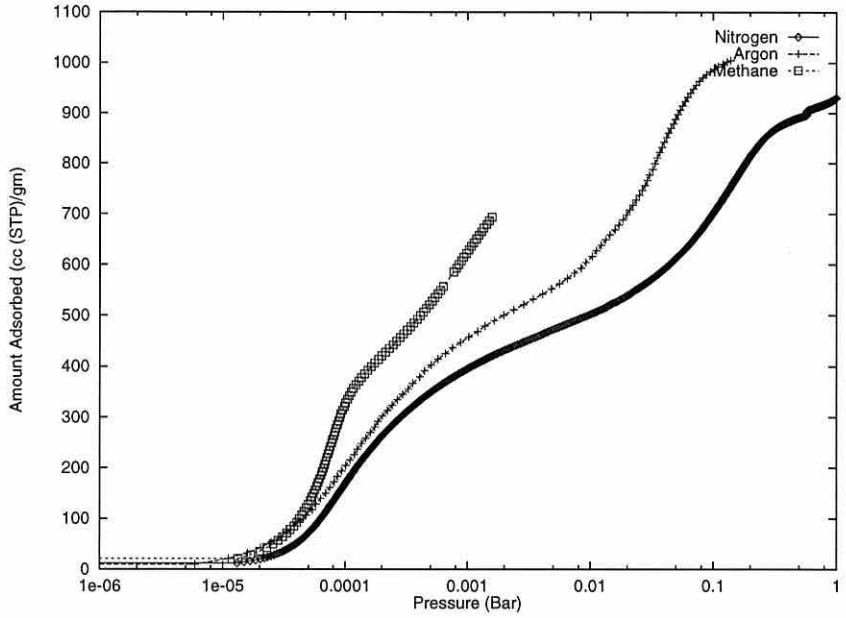

At corresponding pressure values the amount of methane adsorbed is always greater than that of nitrogen and argon. This trend was also observed for the adsorption onto the non-porous carbon, Vulcan (see Section 4.2.3). At low pressures (below $1x10^{-4}$ Bar) the magnitude of the nitrogen and argon isotherms are almost identical, with the amount of argon adsorbed slightly greater than nitrogen.

5.2.2 Gas Adsorption on AX21 at 293K

The adsorption of nitrogen, carbon-dioxide and methane on AX21 was measured repeatedly [18] over the pressure range $5x10^{-3}$ to 1 Bar at 293K. At the same pressure values, the experimentally measured uptake of carbon-dioxide was greater than the uptake of methane which in turn was greater than the uptake of nitrogen on AX21 (Fig 5.4).

The relative differences between the amounts adsorbed for the three different gases also increases as the pressure increases; more so in the case of carbon-dioxide and methane. The amount adsorbed on AX21 at 1 Bar for nitrogen was $16.1 cm^3.g^{-1}$ with larger values of $75 cm^3.g^{-1}$ and $44.7 cm^3.g^{-1}$ for carbon-dioxide and methane respectively. The sequence of carbon-dioxide adsorbing more than methane, which adsorbs more than nitrogen relates to the magnitude of the corresponding parameters ϵ_{ff}/k and ϵ_{sf}/k [Table 4.7].

Figure 5.4: *Adsorption Isotherms of Nitrogen, Carbon-Dioxide and Methane on AX21 at 293K.*

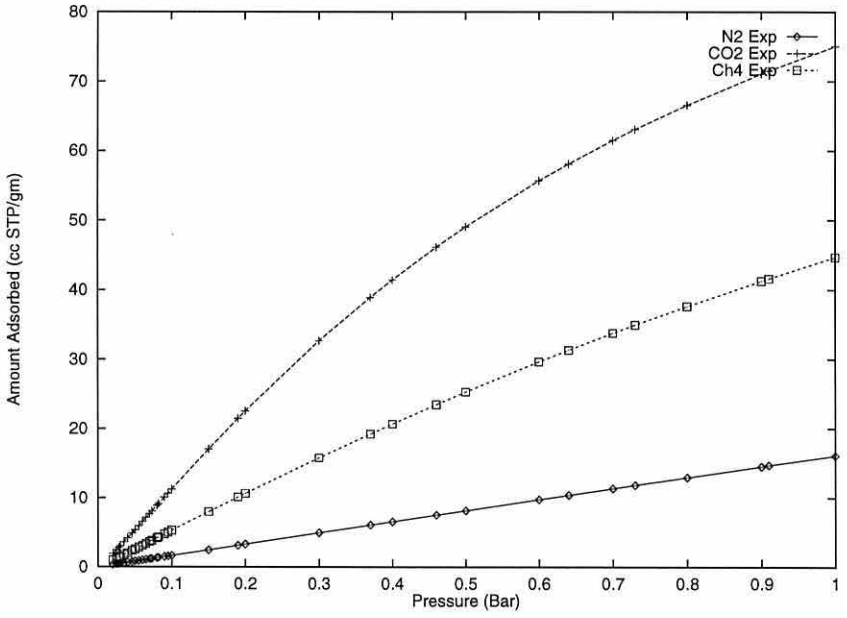

5.3 Isotherms from a DFT model

The non-local theory interaction parameters [Tables 4.6 and 4.7] [16] obtained from fitting the theoretical isotherm of a model flat surface to the experimental isotherm of a real non-microporous surface were used to generate a database of theoretical isotherms, $\rho_{P,H}$ for a range of physical pore widths, H ($6\mathring{A}$ to $1000\mathring{A}$) for the adsorption of nitrogen, argon and methane at 77K and nitrogen, carbon-dioxide and methane at 293K. The pressure range over which the isotherms are generated is $1x10^{-7}$Bar to 1.0 Bar at 77K and 0.19 Bar to 1 Bar at 293K (see Section 2.4.2).

5.3.1 Estimates of the Pore Size Distribution (PSD) of Carbons AX21, Norit, Pica and Supersorbon from Nitrogen Adsorption at 77K

In order to solve Equation (2.76) for $f(H)$, a minimisation algorithm [8] which uses Equation (2.78) was employed. The algorithm minimises a general function $F(x)$ of n independent variables $X = (x_1, x_2, \cdots, x_n)^T$ by the Simplex method. Initial starting values were assigned to the parameters α, β and γ. The number of modes was set equal to 2 as there are 2 steps in the experimental adsorption isotherms (Fig 5.1) [83]. When r (Section 2.4.1) converged to a minimum, the best fit to the experimental adsorption was attained and consequently the best fit pore size distribution.

The sensitivity of the pore size distribution to the extent of data in the database was studied. A database containing isotherms ranging from $6\mathring{A}$ to $1000\mathring{A}$, with an

incremental increase in physical pore width of $1\mathring{A}$ was used in conjunction with experimental data for the adsorption of nitrogen on AX21. The resulting PSD (PSD1) is shown in Fig 5.5. The pore width on the x-axis has units of angstroms and the pore size distribution $f(H)$ on the y-axis has units of cc of pore space per angstrom of pore per gram of adsorbent. This bimodal PSD shows that AX21 is a predominantly microporous material with some mesoporosity and that AX21 consists of pores ranging from $6\mathring{A}$ to $50\mathring{A}$. The location of the peak maxima indicate the greatest proportion of pores have widths of $13\mathring{A}$ and $19.5\mathring{A}$ [Table 5.1].

The database was then reduced by increasing the step size in physical pore width to $2\mathring{A}$ and the PSD (PSD2) then obtained is shown for comparison in (Fig 5.5). By eliminating every other isotherm in the database, the distribution changes; the first peak is reduced in height and becomes broader. Further reduction of the database by increasing the step size to $4\mathring{A}$ is shown in (Fig 5.5) as PSD3 which is broader than PSD2 and the second peak has merged into the first peak.

A fourth experiment was conducted where the original database with a pore width step size of $1\mathring{A}$ was reduced to cover the range 1 to $50\mathring{A}$ (step size remaining at $1\mathring{A}$) and the PSD obtained (PSD4) is also shown in (Fig 5.5). PSD1 and PSD4 are identical; implying that the contribution from pores greater than $50\mathring{A}$ in width is negligible and that AX21 is predominantly microporous. Thus, for this particular porous carbon the extent of the database at pore widths greater than $50\mathring{A}$ has no affect on the shape or magnitude of the PSD. The resolution of the pore widths in the database does however effect the shape of the PSD quite clearly At a step size of $4\mathring{A}$ only one peak appears on the PSD, for a step size of $2\mathring{A}$ the second peak

becomes resolved and it is not until at a step size of $1\mathring{A}$ that a clear distinction between two peaks is observed. Ideally, we would like to use smaller step sizes but this would involve further calculations.

All 4 distributions give a total pore volume of $1.6 cm^3 g^{-1}$ [Table 5.1]. The pore volumes covering the range 6-16$\mathring{A}$ and 6-50$\mathring{A}$ are also shown [Table 5.1] as the trough of each distribution is situated at approximately $16\mathring{A}$.

Table 5.1: *PSD Details for the Adsorption of Nitrogen on AX21 using 2 modes.*

	$PSD1$	$PSD2$	$PSD3$	$PSD4$	$PSD5$
Peak1($\mathring{A}$)	13.0	13.5	15.5	13.0	12.4
Peak2 ($\mathring{A}$)	19.5	19.5	-	19.5	21.4
Peak1 f(H) (cc/$\mathring{A}$/gm)	0.351	0.223	0.124	0.351	0.229
Peak2 f(H) (cc/$\mathring{A}$/gm)	0.070	0.070	-	0.070	0.074
Pore Volume (6-16$\mathring{A}$)	0.747	0.755	0.656	0.747	0.690
Pore Volume (16-50$\mathring{A}$)	0.854	0.855	0.94	0.854	0.825
Pore Volume (Total, cc/gm)	1.601	1.601	1.601	1.601	1.514
r	9.91	12.65	18.4	9.91	20.4

In a previous study by Lastoskie [83] the PSD of carbon AX21 was determined at 77K from nitrogen adsorption. A database containing 33 isotherms was used with an unequal step size in pore width that covered the range 6$\mathring{A}$ to 357.2$\mathring{A}$. After correcting a scaling error in Lastoskie's work [83], the new PSD (PSD5) is in good agreement to that obtained in this work (PSD1), (see Fig 5.6) and gave a total pore volume of 1.5cm^{3}g^{-1} [Table 5.1]. However due to the smaller database the resulting PSD5 has a first peak which is reduced in height and broader (see Table 5.1).

Figure 5.5: *PSD of AX21 Resulting From Nitrogen Adsorption at 77K.*

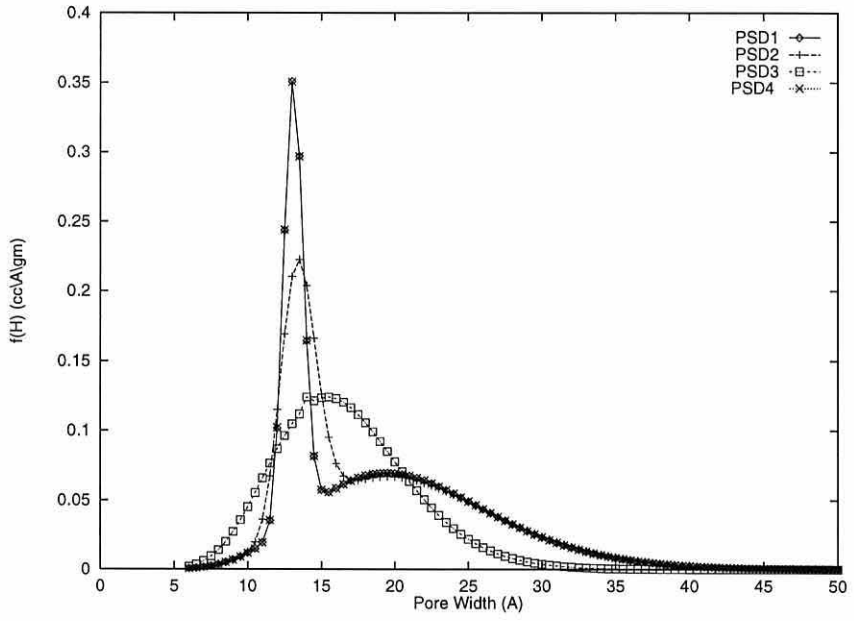

Figure 5.6: *PSD of AX21 Resulting From Nitrogen Adsorption at 77K.*

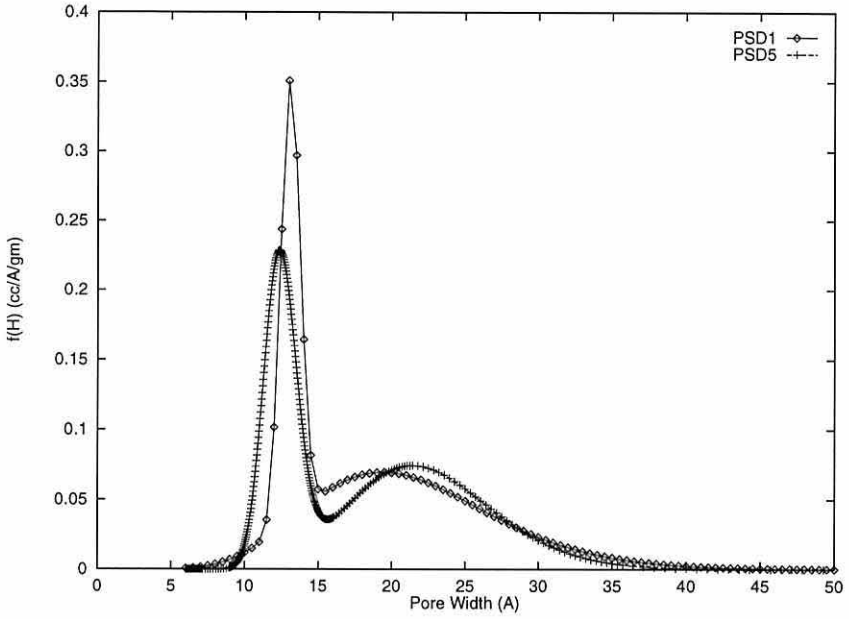

The sensitivity of the PSD to the range of data in the experimental isotherm was also studied. For example, PSD1 is a result of using the full experimental isotherm from adsorption of nitrogen on AX21 (pressure up to 0.1 Bar i.e 224 datapoints). Restriciting the experimental isotherm to pressures below 0.02Bar results in a unimodal PSD (PSD6), the second peak as observed in PSD1 is now absent from the PSD6 in (Fig 5.7). A similar r value (9.92) to that obtained from PSD1 (9.91) was obtained and the first peak is of the same height and width as PSD1. This indicates that the second peak of the PSD corresponds to the second step in the experimental isotherm (Fig 5.1), at pressures above 0.02Bar and so the smallest pores fill first to give the first 'step' in the isotherm.

Figure 5.7: *PSD of AX21 Resulting From Nitrogen Adsorption at 77K.*

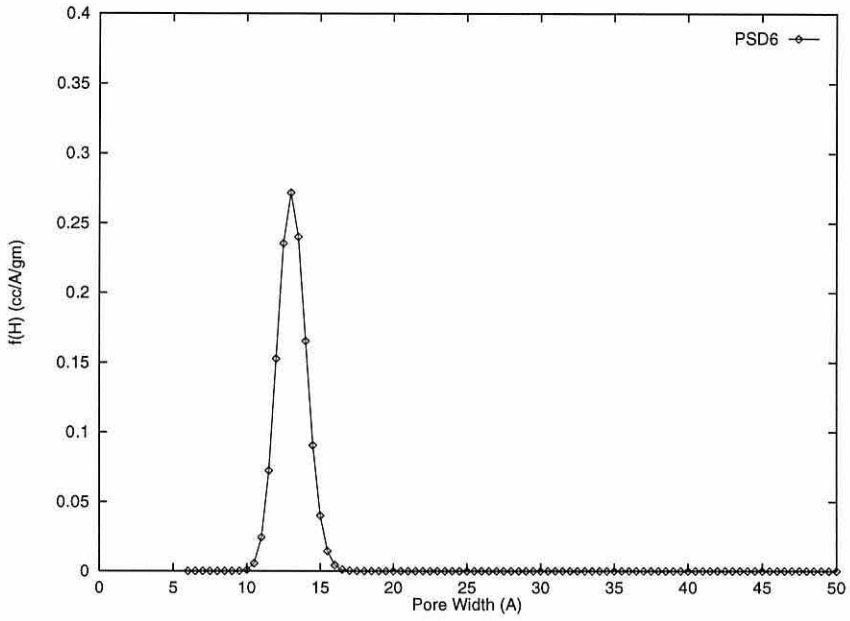

The PSDs of carbons Norit, Pica and Supersorbon were evaluated from the nitrogen database and the corresponding experimental adsorption data for nitrogen. The resulting PSDs are shown in Fig 5.8 along with the PSD of AX21 (PSD1). The peak maxima locations are listed in Table 5.2.

The first peak of the PSDs of all 4 carbons corresponds to the second point of inflexion or 'first step' in the experimental isotherms (Fig 5.1). The greatest uptake of nitrogen is on AX21, followed by Supersorbon, Pica and Norit. These observations are reflected in the relative heights of the first peak in the corresponding PSDs: this peak is highest for AX21 followed by Supersorbon, Pica and Norit. The first peak of the Pica and Supersorbon's PSDs are similar in height and width with the peak of Supersorbon slightly higher than Pica which explains the relative amounts of nitrogen adsorbed (Fig 5.1). The uptake of Supersorbon is greater than that of

Pica on completion of the monolayer and the step is also more more distinct on Supersorbon.

Referring to Fig 5.1, the Pica and Supersorbon isotherms are almost identical at low pressure, up to the first step. The second step in the Pica isotherm is much flatter than that of the Supersorbon isotherm and consequently the second 'peak' of the Pica PSD is lower than that of Supersorbon in Fig 5.8. The second step of the AX21 isotherm is sharper than all 3 other isotherms and the resulting second peak in the PSD is highest for AX21.

The second peak of the PSDs of Norit and Supersorbon are closest in shape and magnitude and in (Fig 5.1) after the completion of the monolayer the Norit and Supersorbon isotherms are more similar in shape than any other pair of adsorbents.

The PSD of AX21 is bimodal. Norit, Pica and Supersorbon give a well defined

Figure 5.8: *PSDs of AX21, Norit, Pica and Supersorbon from N_2 Adsorption.*

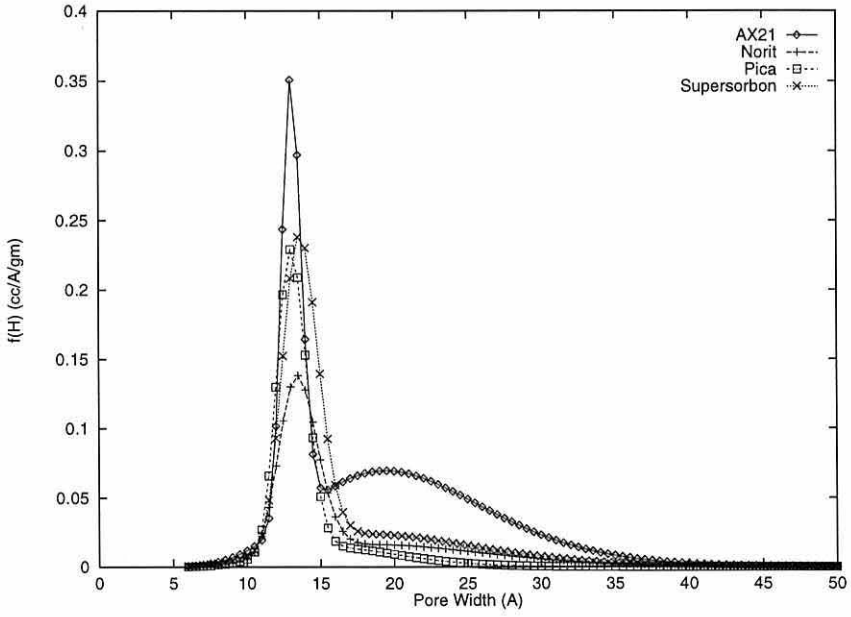

peak in the micropore region and a less well defined peak in the mesoporous region. All 4 materials are predominantly microporous and mesoporous i.e they contain both micro and mesopores. The relative contribution of the microporous region to the total pore volume is greatest for AX21, followed by Supersorbon, Norit and Pica.

The best fit to the experimental uptake of nitrogen on AX21, Norit, Pica and Supersorbon are shown in (Figs 5.9 to 5.12) on a logarithmic pressure scale, with error-bars on the experimental data. The r values are listed in Table 5.2.

Table 5.2: *PSD Details for the Adsorption of Nitrogen on AX21, Norit, Pica and Supersorbon using 2 modes.*

	$AX21(PSD1)$	$Norit$	$Pica$	$Supersorbon$
Peak1($\AA$)	13.0	13.5	13.0	13.5
Peak2($\AA$)	19.5	-	-	-
Peak1 f(H) (cc/$\AA$/gm)	0.351	0.138	0.230	0.238
Peak2 f(H) (cc/$\AA$/gm)	0.747	-	-	-
Pore Volume (6-16$\AA$)	0.854	0.462	0.611	0.744
Pore Volume (16-50$\AA$)	1.196	0.219	0.086	0.31
Pore Volume (Total, cc/gm)	1.601	0.681	0.696	1.054
r	9.91	10.2	9.98	10.1

Figure 5.9: *Fit to AX21 for Nitrogen Adsorption at 77K.*

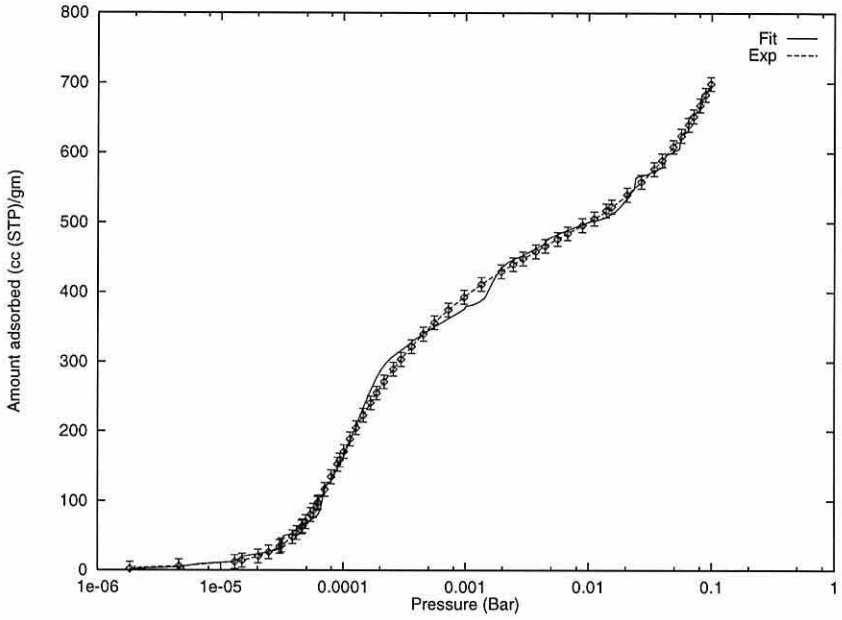

Figure 5.10: *Fit to Norit for Nitrogen Adsorption at 77K.*

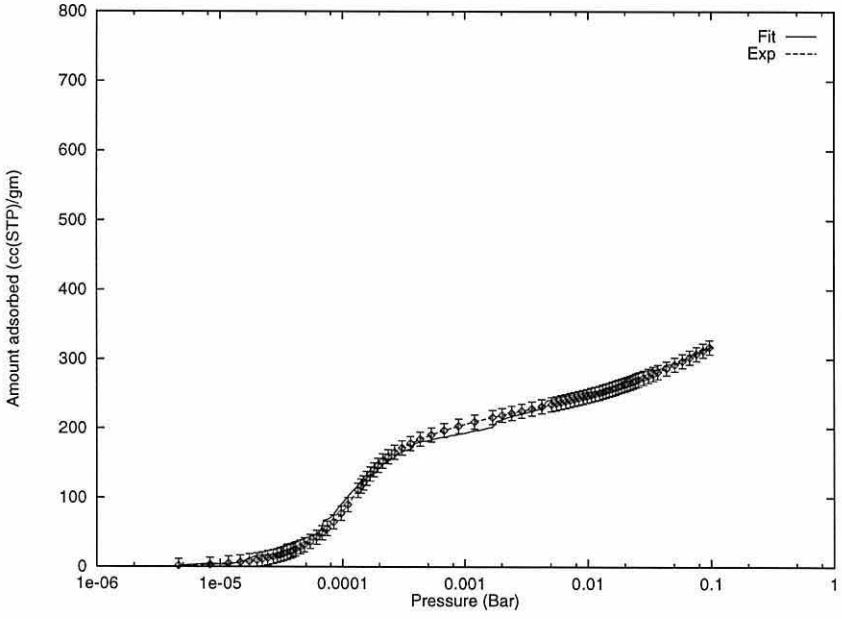

Figure 5.11: *Fit to Pica for Nitrogen Adsorption at 77K.*

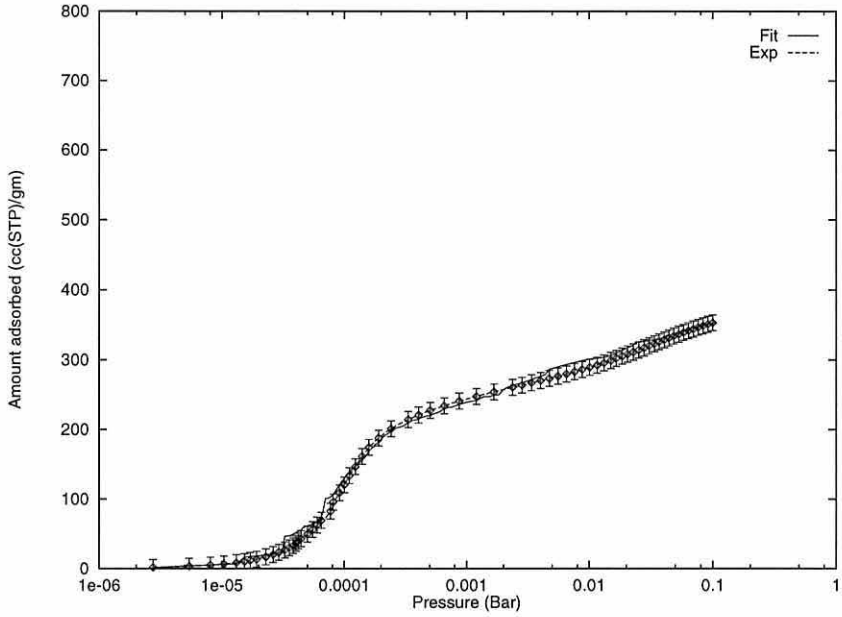

Figure 5.12: *Fit to Supersorbon for Nitrogen Adsorption at 77K.*

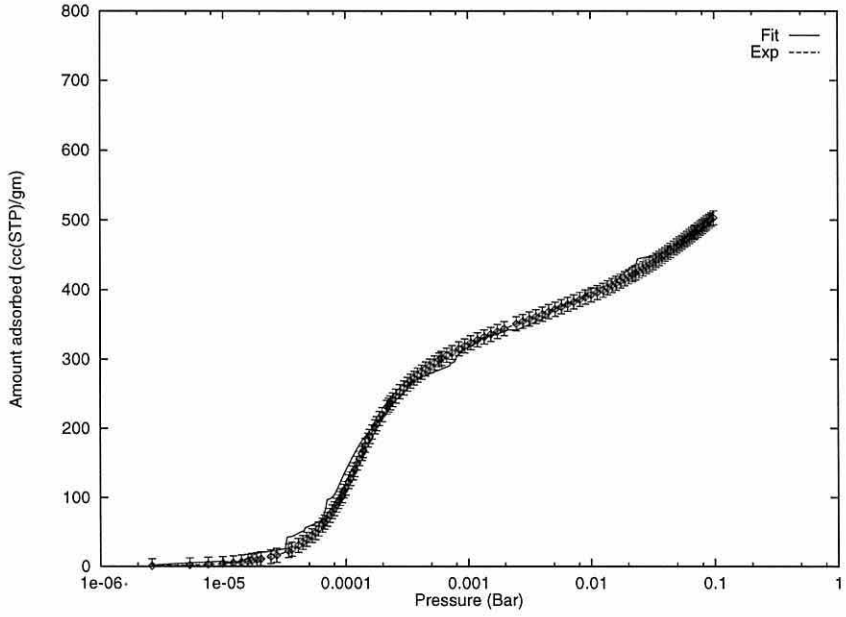

A single set of parameters was also used for the evaluation of the PSDs of AX21, Norit, Pica and Supersorbon from nitrogen adsorption and the results are shown in Fig 5.13.

It is clear that the second peak of each distribution which was evident when a bimodal function was used is now absent and the PSDs are now unimodal. The first peak of each PSD is reduced slightly in height and is broadened [Table 5.3]. The distributions extend over the pore ranges: 6-30$\AA$, 6-39$\AA$, 6-22$\AA$, and 6-36$\AA$ for AX21, Norit, Pica and Supersorbon respectively. The r values obtained from using 1 mode [Table 5.3] are slightly higher than those obtained using 2 modes [Table 5.2] and 1 mode alone cannot reproduce the experimental adsorption isotherm including the second step. Therefore, r is a sensitive measure of the fit to the experimental adsorption isotherm.

Figure 5.13: *PSDs of AX21, Norit, Pica and Supersorbon using 1 mode.*

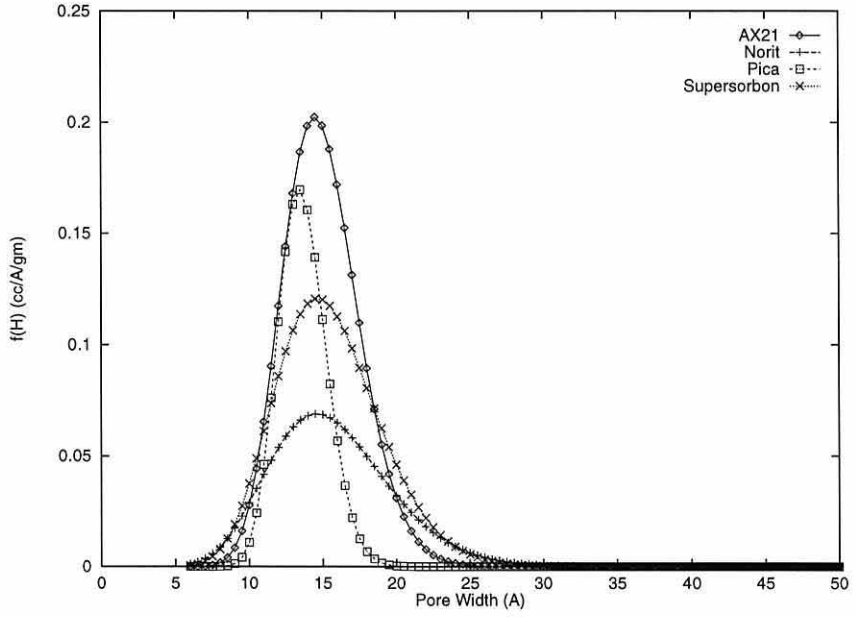

5.3.2 Estimates of the Pore Size Distribution (PSD) of carbons AX21 and Supersorbon from Argon Adsorption at 77K

Using the argon database and mean experimental data for the adsorption of argon on AX21 and Supersorbon, Equation (2.76) was solved for $f(H)$ using 2 modes and the resulting PSDs are shown in Fig 5.14. The 2 PSDs are bimodal. The first peak of the Supersorbon PSD is higher and narrower than that of AX21. However, the total micropore volume of AX21 (1.3) is greater than Supersorbon (1.0) as expected from the greater adsorption of argon on AX21 (Fig 5.2). The first step of the AX21 isotherm (Fig 5.2) is less pronounced than the first step in the Supersorbon isotherm and this is reflected in the narrower distribution of the first peak of the PSD of Supersorbon. The total pore volume of AX21 is approximately 20 per cent higher than that of Supersorbon [Table 5.4].

Table 5.3: *PSD details for the Adsorption of Nitrogen on AX21, Norit, Pica and Supersorbon using 1 mode.*

	$AX21(PSD1)$	$Norit$	$Pica$	$Supersorbon$
Peak1($\AA$)	14.5	14.5	13.5	14.0
Peak1 f(H) (cc/$\AA$/gm)	0.202	0.069	0.169	0.118
Pore Volume (Total, cc/gm)	1.30	0.684	0.692	1.05
r	11.1	11.6	11.4	11.5

Table 5.4: *PSD Details for the Adsorption of Argon on AX21 and Supersorbon using 2 modes.*

	*AX*21	*Supersorbon*
Peak1($\AA$)	12.5	14.0
Peak2 ($\AA$)	33.5	34.0
Peak1 f(H) (cc/$\AA$/gm)	1.038	1.551
Peak2 f(H) (cc/$\AA$/gm)	0.431	0.028
Pore Volume (6-16$\AA$)	0.578	0.578
Pore Volume (16-50$\AA$)	0.685	0.430
Pore Volume (Total, cc/gm)	1.262	1.008
r	11.1	12.4

The PSDs resulting from argon adsorption show that AX21 consists of micropores and mesopores but that the micropores dominate the distribution. With argon acting as the adsorbate, the pore size distribution of AX21 covers the range 6 to 63 $\mathring{A}$.

The second peak of the AX21 distribution from argon adsorption (Fig 5.14) is much broader than that observed with nitrogen adsorption on AX21 (Fig 5.8): the peak maximum is located at 12.5$\mathring{A}$ and 33.5$\mathring{A}$ compared to 13$\mathring{A}$ and 19.5$\mathring{A}$ for nitrogen. With argon adsorption, the AX21 PSD there has no contribution from pores greater than 63$\mathring{A}$.

The resulting best fit adsorption isotherms are shown below in Figs 5.15 and 5.16 with error-bars on the experimental data. It was not possible to obtain a fit from solving Equation (2.76) with the methane database.

Figure 5.14: *PSDs of AX21 and Supersorbon from Argon Adsorption.*

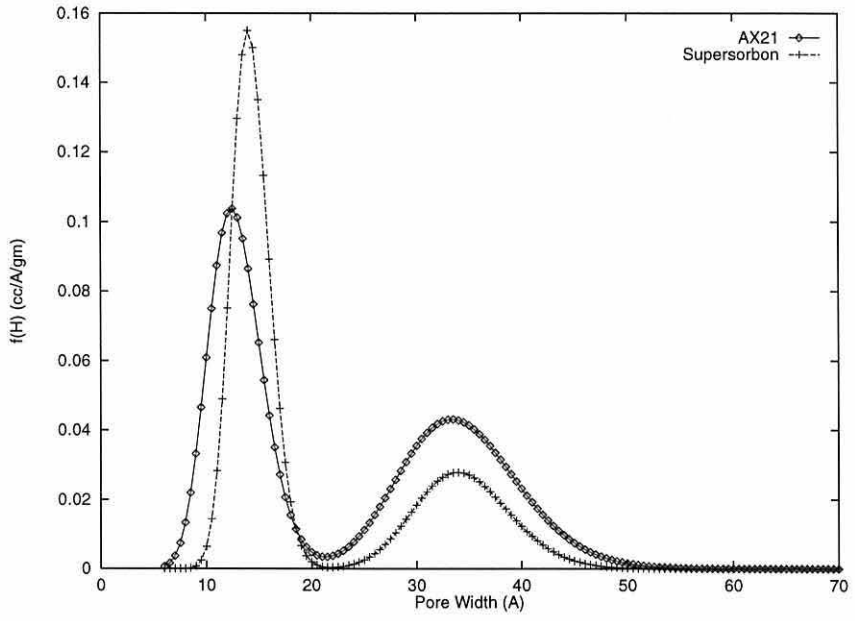

Figure 5.15: *Fit to AX21 for Argon Adsorption at 77K.*

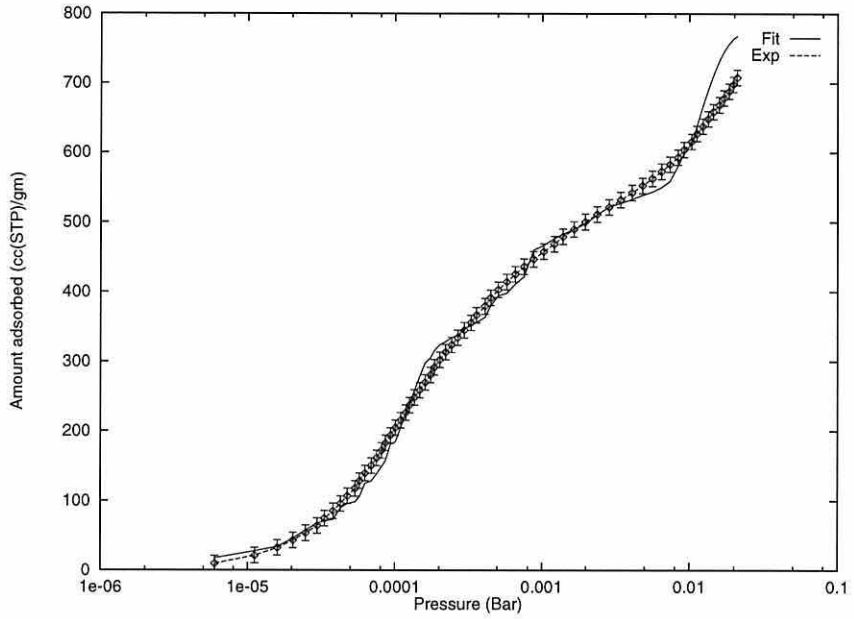

Figure 5.16: *Fit to Supersorbon for Argon Adsorption at 77 K*

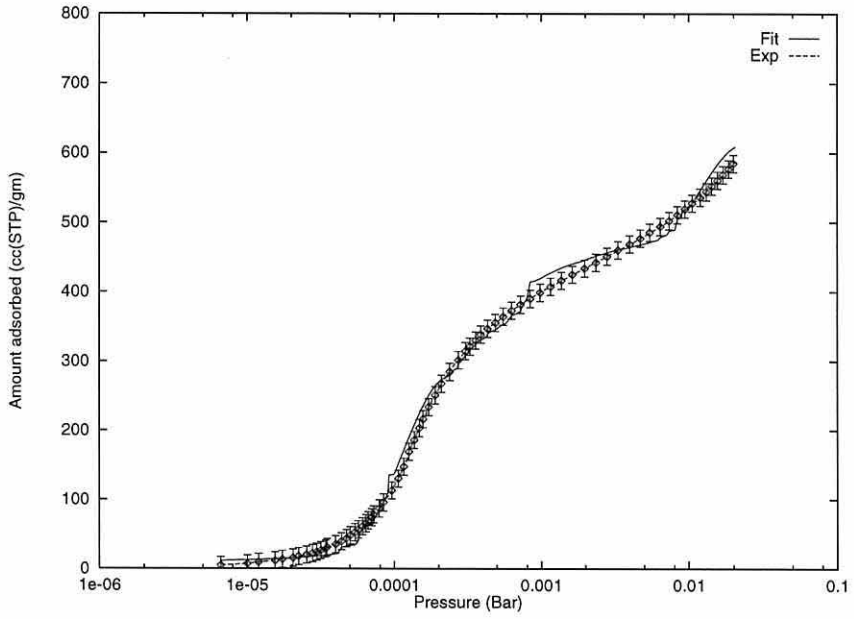

5.3.3 Estimates of the Pore Size Distribution (PSD) of Carbon AX21 at 293K.

Databases were also constructed from theoretical isotherms calculated using non-local density functional theory for the adsorption of nitrogen, carbon-dioxide and methane at 293K. The fits to the experimental isotherms of AX21 for nitrogen, carbon-dioxide and methane adsorption are shown in Fig 5.17, with errorbars on the experimental data.

The PSD's obtained from the 77K data cannot be used to predict carbon-dioxide uptake at room temperature; the larger pore sizes lead to a substantial underestimation of the adsorbed gas volumes. However, the carbon-dioxide distribution can be used to predict the behaviour of nitrogen on AX21 at 293K. As there is only one steeply rising part in the experimental isotherm (Fig 5.4), 1 mode was used and an r of 0.11 was found for the carbon-dioxide fit which is well within the experimental error. Small changes in the parameters describing the carbon-dioxide PSD were made in order to predict the pore size distributions from nitrogen and methane adsorption. The resulting pore size distributions from the minimisation algorithm using 1 mode are shown in (Fig 5.18).

Figure 5.17: *Fits to AX21 for Nitrogen, Carbon-Dioxide and Methane Adsorption at 293K.*

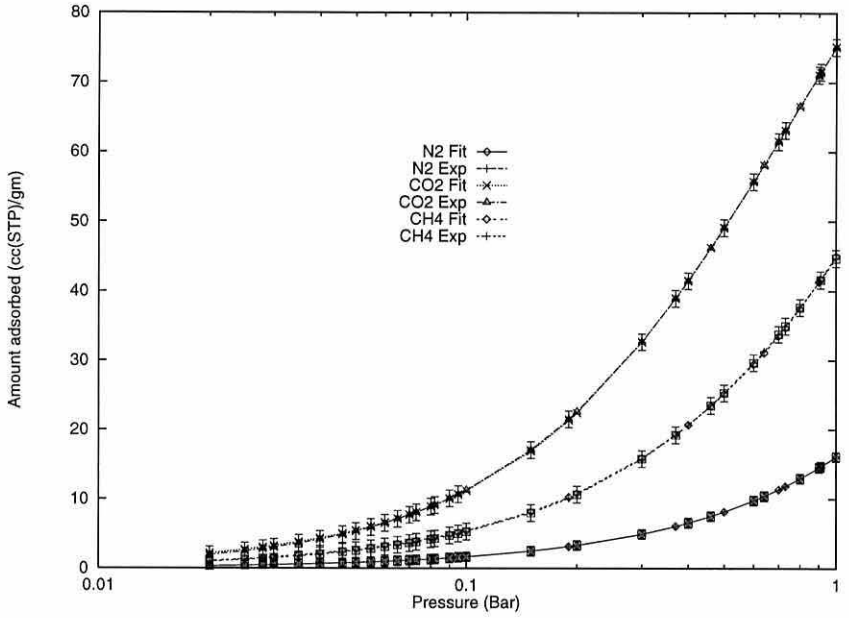

Figure 5.18: *PSD of AX21 from Nitrogen, Carbon-Dioxide and Methane Adsorption at 293K.*

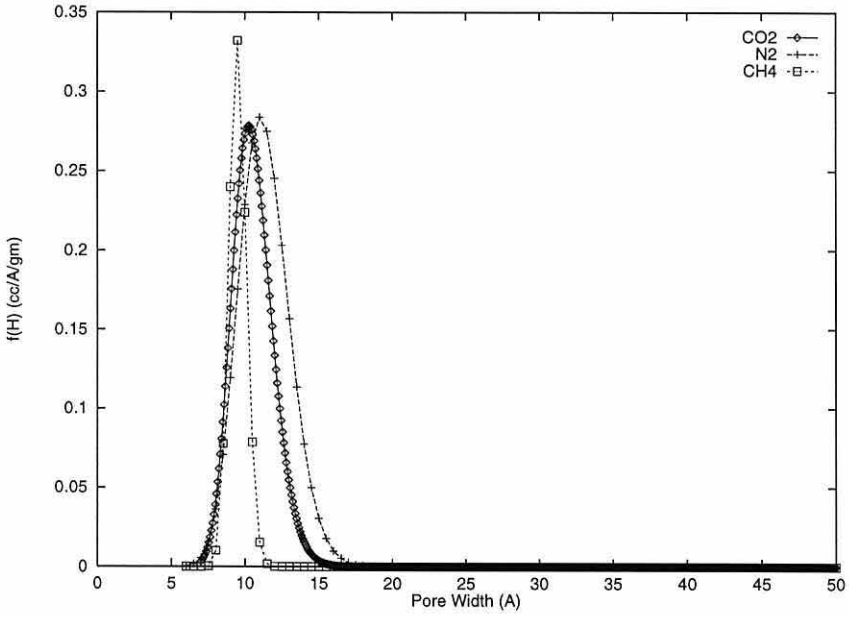

Since the experimental error for carbon-dioxide is 1.2 the root mean square deviation of 0.11 is well within the experimental error [17]. The peak maxima for nitrogen is located at $11\mathring{A}$ and the carbon-dioxide and methane peaks are located at $10.3\mathring{A}$ and $9.5\mathring{A}$ respectively [Table 5.5]. The PSDs are very similar in width and height. Therefore at 293K, AX21 exhibits micro and mesoporosity.

Table 5.5: *PSD Details for the Adsorption of Nitrogen, Carbon-Dioxide and Methane on AX21.*

	N_2	CO_2	CH_4
Peak1($\mathring{A}$)	11.0	10.3	9.5
Peak1 f(H) (cc/$\mathring{A}$/gm)	0.284	0.278	0.332
Pore Volume (Total, cc/gm)	1.19	0.931	0.59
r	0.001	0.11	0.04

Comparing the PSD of AX21 from carbon-dioxide adsorption at room temperature with the PSD of AX21 from the adsorption of nitrogen at 77K, the carbon-dioxide peak is centred at $10.3\mathring{A}$ rather than $13.0\mathring{A}$, and the total pore volume is $1cm^3g^{-1}$ rather than $1.6cm^3g^{-1}$. The carbon-dioxide PSD was used to predict the behaviour of nitrogen and methane on AX21 at 293K and gave r values of 0.001 and 0.04 respectively where the experimental errors are 0.7 and 1.2 respectively. The carbon-dioxide PSD is therefore an acceptable solution for prediction of the other gases.

Figure 5.19 compares the PSDs resulting from nitrogen adsorption at 77K and

293K. At 293K pores of smaller width become more accessible to nitrogen than at 77K [17].

Figure 5.19: *PSD of AX21 from Nitrogen Adsorption at 293K and 77K.*

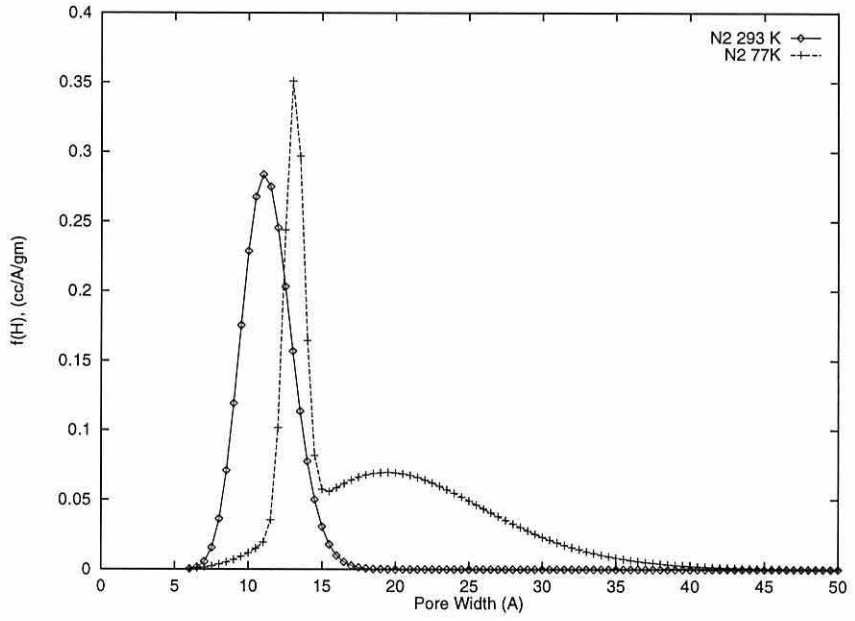

We suggest the following explanation for the shift in the distribution to pores of smaller width with increasing temperature. Let a pore (A) of width $10\mathring{A}$ contain 100 molecules and a pore (B) of width $30\mathring{A}$ contain 300 molecules. As the temperature is increased from 77K to 293K, more molecules will evaporate from the larger pore (B) than pore (A) due to the potential well of pore B being shallower than that of A. The distribution will therefore shift to the smaller pores. The shift will also be greater for larger pores so the difference in peak maxima location will be greater between the peaks positioned in the highest pore width range. For nitrogen adsorption, the difference between the micropore peak at 293K and 77K is $2.0\mathring{A}$ and for the mesopore peak the difference is $3.5\mathring{A}$.

The total pore volume, found by integrating the limits of the PSD on the x-axis from nitrogen adsorption is $1.6cm^3.g^{-1}$ and $1.2cm^3.g^{-1}$ at 77K and 293K respectively. The total pore volume from nitrogen adsorption at the two temperatures compare well.

5.4 Conclusions

Experimental adsorption of nitrogen and argon on the surface of microporous carbons were measured at 77K. Despite their different adsorption properties, nitrogen and argon formed 2 distinct layers at comparable monolayer completion pressures on all 4 surfaces.

The DFT model is successful in modelling the adsorption of nitrogen and argon on microporous carbons at 77K and 293K however the predicted uptake of methane was not obtainable.

At constant temperature, the PSDs of AX21 are shown to be different for the adsorption of different gases. Argon, when used as an alternative surface probe under the same conditions, revealed a higher sensitivity to ultra micropores than nitrogen.

The extent of the non-local density functional theory database and incremental increase in pore width have been shown to influence the calculated PSDs, and a step of $1\mathring{A}$ for the pore widths of each isotherm is required to attain an accurate description of the surface. It has also been shown that the number of inflexion points in the experimental isotherm is a good indication of the number of modes to be used

in calculating the pore size distribution.

Apart from our suggested explanation, the fact that greater numbers of smaller pores are detected at room temperature than at 77K could be due to simple kinetic effects as the measurements at 77K may not have had time to equilibriate at the lowest pressures ($< 1x10^{-5}$ Bar). Alternatively, it is possible that pores with widths of less than approximately $10\mathring{A}$ are not detected due to the freezing of nitrogen in the pore junctions [12] and pores connecting them [14]. Calculation [15] of freezing points for nitrogen in slit-graphitic pores show that at 77K, pores smaller than approximately $13\mathring{A}$ are frozen solid. It follows that if pores with widths of $10\mathring{A}$ are accessed via pores with widths of $13\mathring{A}$ (as detected by nitrogen at 77K, (Fig 5.8)) the smaller pores will not contribute to the adsorption isotherm and will not be observed at 77K.

The fact that the carbon-dioxide PSD is capable of predicting the room temperature adsorption of other gases (methane and nitrogen) is of considerable importance in the design of materials for separation processes since it implies that one PSD may be used to predict separation factors for gas mixtures [17]. This is the subject of the next chapter.

Chapter 6

Selectivity of Porous Carbons

6.1 Introduction

Industrial processes based on the adsorption of gases on carbonaceous surfaces play an important role in many fields [87]. Selective adsorption of the main green-house gas, carbon dioxide, from gaseous mixtures is a promising method of limiting the amount released into the atmosphere [88]. There are authors [89] who claim that a combination of the adsorption of carbon dioxide from gaseous mixtures and its subsequent catalytic hydrogenation to oxygenates and hydrocarbons can greatly suppress the level of carbon-dioxide in the atmosphere. It is unlikely that the green-house gas problem could be solved in this way alone. Nevertheless, the separation and breakdown of carbon-dioxide from gaseous mixtures is a promising approach.

The design of industrial adsorbers is usually based on experimental evaluation of adsorption properties of adsorbents such as; mass, energy balance and scale up calculations. There are many techniques available for the evaluation of composition and surface properties of microporous materials [90]. However, few of them are able to relate this to gas adsorption in pores of a particular size. If the only requirements for effective separation are a material with a very narrow PSD, standard experiments cannot easily discover this fact. Instead, repetition of adsorption experiments for a large number of surfaces with variable PSDs is an option, however, it is an expensive and time consuming approach. If this intuitive solution is substituted by a combination of experiment and molecular simulation, the efficiency of an adsorption process could be dramatically increased. Conditions of separation (load of an adsorbent, temperature, pressure, etc.) are simpler to adjust when the separation

properties of individual pores are known. Thus, a combination of theoretical calculations and experiment should lead to the suggestion of tailor-made microporous carbon especially suitable for the type of adsorption required, at a lower cost.

In this chapter a model of a single and multicomponent adsorption equilibria for nitrogen, carbon-dioxide and methane at 293K and pressures up to 1 Bar is studied. Such data is available either from a large number of experiments on mixtures or from theoretical models optimised for the particular adsorbent and gas mixture of interest, combined with experiments on single component systems.

In this work, experimental effort [16] was substantially reduced by using the Ideal Adsorbed Solution theory [91], one of the widely used methods [92], [93], [94], [95] for prediction of multicomponent behaviour from single component adsorption isotherms.

The single component adsorption equilibria for nitrogen, carbon dioxide and methane were obtained by NL-DFT calculations (see Section 2.3) [96], [97], [98], [99] and by experiments on microporous [Chapter 5] and graphitized carbons [Chapter 4] at 293K. These data were used to predict the behaviour of gas mixtures at room temperature and pressures up to 1 Bar. Industrial adsorbents usually work either at much lower temperatures or much higher pressures than systems described in this chapter. The conditions put forward here were used to simplify the problem and to clearly illustrate the design of the microporous structure.

6.2 Ideal Adsorbed Solution Theory (IAS)

On the basis of the single component experimental and DFT generated isotherms, the behaviour of binary gas mixtures was predicted. The IAS theory is based on the assumptions that perfect mixing of adsorbates occurs and that the adsorbed mixture is an ideal solution at constant spreading pressure and temperature [91], [110], [111], [112]. It is valid for the chemical potential of the adsorbed solution:

$$\mu_i(T, \pi, x) = \mu_i^0(T, \pi) + RT \ln x_i \tag{6.1}$$

and

$$\mu_i^0(T, \pi) = \mu_{st}^0(T) + RT \ln P_i^0 \tag{6.2}$$

Where $\mu_i^0(T, \pi)$ is the chemical potential of an individual component i adsorbed on the surface at the same temperature T and spreading pressure π as the mixture. x_i is the pore mole fraction of a component i in an adsorbed state, μ_{st}^0 is the standard state chemical potential of the ideal gas of component i, and P_i^0 is the pressure of the bulk pure gas in equilibrium with the pure adsorbate when the spreading pressure is π. If the bulk mixture is also an ideal gas [91], [110], [111], [112] then the condition for equilibrium between the ideal adsorbed solution and the bulk gas mixture is:

$$RT \ln P + RT \ln y_i = RT \ln P_i^0 + RT \ln x_i \tag{6.3}$$

Where P is the total pressure of the gas-phase mixture and y_i is the bulk mole fraction. It follows (analogy with Raoult's law for vapour-liquid equilibria):

$$P\ y_i = P_i^0\left(\pi\right) x_i \tag{6.4}$$

The pressure P_i^0 and the spreading pressure, π are related [107] according to the Gibbs adsorption isotherm:

$$\pi\left(P_i^0\right) = \frac{RT}{A\int_0^{P_i^0} q_i\left(p\right) d\ln p} \tag{6.5}$$

Where $q_i\left(p\right)$ is an experimental or generated adsorption isotherm. On the basis of the above equations it is possible [22] to calculate x_i for a given P and y_i.

6.2.1 Selectivity of Adsorption

The suitability of designed adsorption systems depends on the selectivity of adsorption (separation factor) [102]. For a binary mixture it is defined as:

$$S = \left(x_1/y_1\right) / \left(x_2/y_2\right) \tag{6.6}$$

It is the ratio of the mole fractions in the pore divided by the ratio of the mole fractions in the bulk. x_i is the pore mole fraction and y_i is the bulk mole fraction. Values greater than unity imply that component 1 is more strongly adsorbed than component 2. In all calculations the bulk mole fractions of the binary mixture components were set equal ($y_1 = y_2 = 0.5$).

Two types of selectivity isotherms based on DFT adsorption raw data were studied; the dependency of the separation factor on pressure for a particular pore size and the dependency of the separation factor on pore size at a particular pressure

[113]. These isotherms could be indirectly compared with experimental data by using an average of selectivity isotherms which covered the whole pore size range of the microporous carbon under investigation.

Average Selectivity Isotherms

Average selectivities based on $S(i)$ values from IAS theory for DFT generated single component data were computed. The average selectivity is defined as:

$$S_{av.} = \left(x_1^{av.}/x_2^{av.}\right) / \left(y_1/y2\right) \tag{6.7}$$

Where $x_1^{av.}$, $x_2^{av.}$ and y_1 and y_2 are average pore mole fractions and bulk mole fractions of component 1 and 2 in a binary mixture, respectively. For $x_1^{av.}$ and $x_2^{av.}$ the following is valid:

$$x_1^{av.} = \frac{\sum_{pores} x_{1(i)} \left(N_{(i)}^{tot.}\right)}{\sum_{pores} N_{(i)}^{tot.}} \tag{6.8}$$

$$x_2^{av.} = \frac{\sum_{pores} \left(1 - x_{1(i)}\right) \left(N_{(i)}^{tot.}\right)}{\sum_{pores} N_{(i)}^{tot.}} \tag{6.9}$$

Since

$$N_1 = \sum_{pores} \left(x_{1(i)}\right) \left(N_{(i)}^{tot.}\right) \tag{6.10}$$

$$N_2 = \sum_{pores} \left(1 - x_{1(i)}\right) \left(N_{(i)}^{tot.}\right) \tag{6.11}$$

and

$$1 - x_{1(i)} = x_{2(i)} \tag{6.12}$$

Where $N_{(i)}^{tot}$ is the total number of moles in a pore. For each pore size $N_{(i)}^{tot.}$ is given by:

$$N_{(i)}^{tot.} = \frac{\left(p_{1(i)}^{pure} p_{2(i)}^{pure} V_i\right)}{\left(x_{1(i)} p_{2(i)}^{pure} + \left(1 - x_{1(i)}\right) p_{1(i)}^{pure}\right)} \tag{6.13}$$

Where V_i is the volume of a pore of a particular size.

$$p_{1(i)}^{mix} = x_{1(i)} p_{1(i)}^{pure} \tag{6.14}$$

$$p_{2(i)}^{mix} = \left(1 - x_{1(i)}\right) p_{2(i)}^{pure} \tag{6.15}$$

The pore mole fraction in each pore is calculated from selectivity values for each pore size:

$$S_{(i)} = \left(x_{1(i)}/x_{2(i)}\right)\left(y_1/y_2\right) \tag{6.16}$$

and

$$R_y = \frac{y_1}{y_2} \tag{6.17}$$

$$x_{1(i)} = \frac{\left(R_y S_{(i)}\right)}{1 + R_y S_{(i)}} \tag{6.18}$$

The $Sav.$ value can be compared with $S_{exp.}$ calculated from the AX21 experimental data.

The volumes of individual pores used in calculation of $S_{av.}$ were evaluated on the basis of the PSD of AX21 determined from adsorption of carbon-dioxide at 293K (Fig 5.18).

The experimental data for carbon-dioxide adsorption on AX21 (Fig 5.4) (Section 5.2.2) was used for prediction of the selectivity of adsorption, and is comparable with $S_{av.}$, (see Equation 6.7). Single component DFT isotherms for nitrogen, carbon-dioxide and methane adsorption in a variety of pore widths are shown in (Figs 6.1 to 6.3). In very narrow pores (around 7.0$\mathring{A}$) the isotherms are typically of the first type according to the Brunauer classification [90]. These isotherms reflect the formation of a monolayer on the surface inside the ultra narrow pores. The trend is especially clear on adsorption isotherms of carbon dioxide and methane. This phenomenon could be explained in terms of additional attractive forces which are present in very narrow micropores [46].

Figure 6.1: *DFT generated isotherms for nitrogen adsorption.*

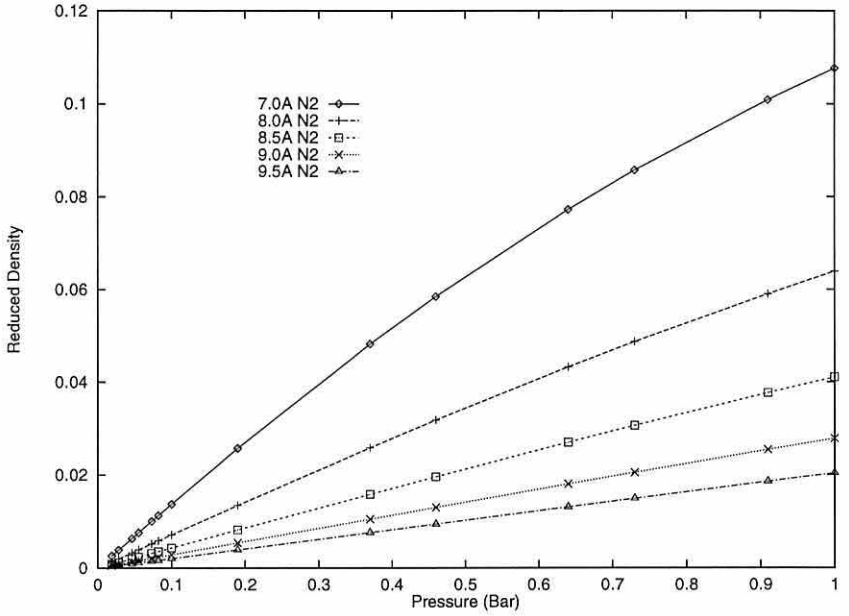

Figure 6.2: *DFT generated isotherms for carbon dioxide adsorption.*

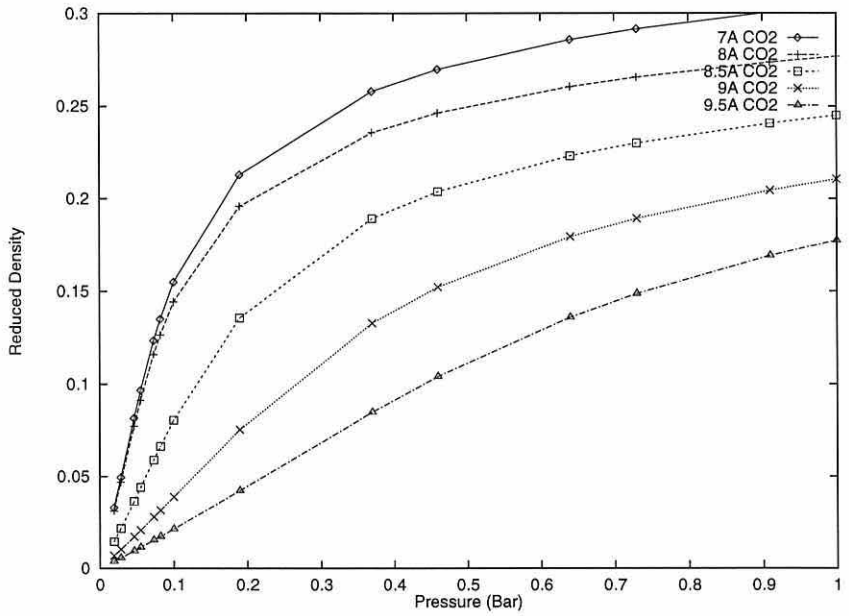

Figure 6.3: *DFT generated isotherms for methane adsorption.*

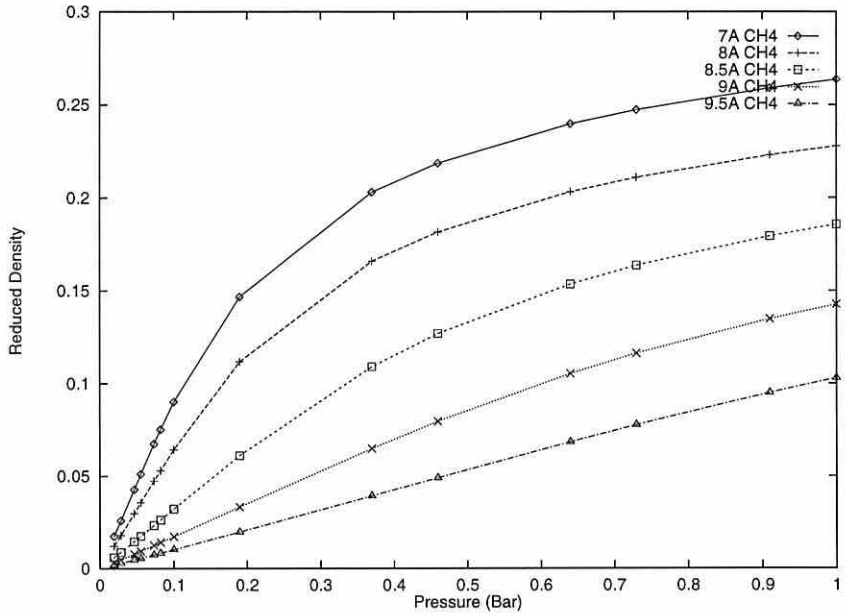

6.2.2 Prediction of multicomponent adsorption equilibria by IAS theory

The adsorption isotherm equation that fits the experimental data best must be used in calculation of the spreading pressures [112]. Several isotherms were tested, however, only three of them fit the data satisfactorily: (a) the Langmuir isotherm (L isotherm) [59]

$$q_i = \frac{q_{m,i}\ K_i\ p_i}{1 + K_i pi} \tag{6.19}$$

(b) a combination of Langmuir and Freundlich isotherms (LF isotherm) [118]:

$$q_i = \frac{q_{m,i}\,(K_i p_i)^n}{(1 + (K_i p_i)^n)} \tag{6.20}$$

and (c) Dubinin-Radushkevich isotherm (DR isotherm) [55]:

$$q_i = q_{m,i} exp\left(-K_i \left(\ln\left(p_{s,i}/p_i\right)\right)\right)^2 \tag{6.21}$$

Where $q_{m,i}$ is the monolayer capacity, $p_{s,i}$ is the saturation vapour pressure and K_i and n are adjustable parameters. The selected isotherm must fit the experimental data well, especially in the sensitive low pressure region because p_i weights the function $q_i^* = \left(q_{i(p_i)}/p_i\right)$ in Equation (6.5). Strictly speaking any adsorption isotherm used should reduce to Henry's isotherm in the low pressure regions - which is effectively Henry's law applied to a two-dimensional solution instead of a bulk solution [112]. It emerges as a special case in the low pressure limit of Langmuir's isotherm. Both the Langmuir-Freundlich and the Dubinin-Radushkevich equations have incorrect low pressure limits [112]. However, these errors are generally less than the experimental error, and they usually fit the experimental adsorption equilibria better, even in the low pressure regions.

Constants of the adsorption isotherm equations were evaluated [21] by the Levenberg-Marquardt non-linear regression method [119]. The estimated values were compared with those obtained [21] by a random walk algorithm [116]. It appeared that the regression parameters were independent of the regression method if the equation fitted the experimental data well. The quality of a fit was assessed by the correlation coefficient of determination ($r2$). This coefficient describes the variability in the response (in this case q_i) due to variation in the explanatory variable (p_i). The $r2$ value is used to pick the best curve fit from a group of fitted functions since the closer the correlation coefficient is to unity, the better the fit. DFT generated data for equilib-

rium adsorption of carbon dioxide in a pore of size $7\mathring{A}$ and the three fitted functions (LF, L, DR) are shown in (Fig 6.4). It is seen that the best fit over the whole pressure range was obtained with the Langmuir-Freundlich isotherm ($r2$=0.999), Dubinin-Radushkevich equation was slightly less accurate ($r2$=0.995), and the worst accuracy of a fit was obtained by using the Langmuir isotherm ($r2$=0.987). Despite its incorrect low pressure limit, we chose to use the LF isotherm since it shows the best fit.

Figure 6.4: *Adsorption equilibria of carbon dioxide modelled by DFT for the pore size H=7Å and different fitting functions; LF equation, DR equation and L equation.*

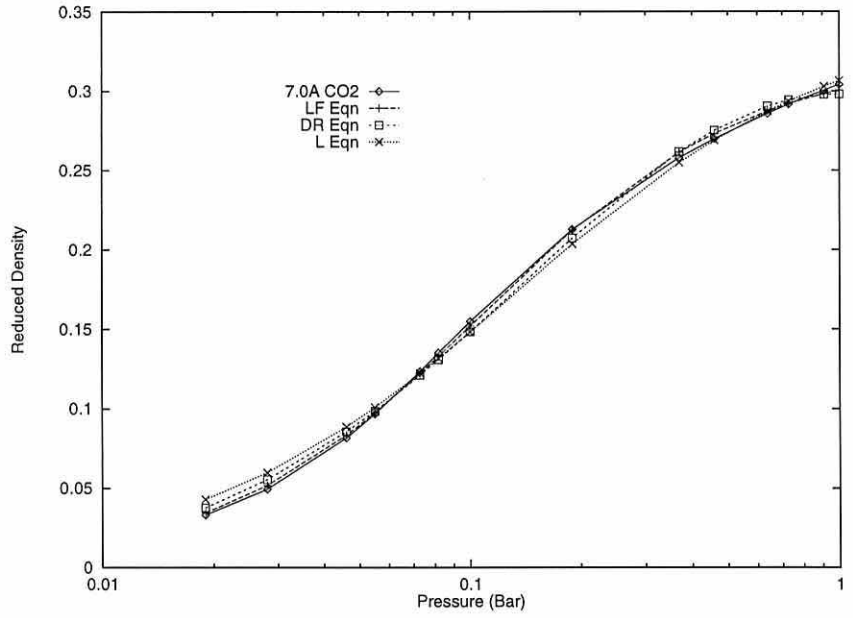

Carbon Dioxide over Nitrogen

A set of selectivity isotherms in slit micropores of different radius are given in 3D geometry in (Fig 6.5) as a 3D surface map. It shows that a variation of the separation

factor with pressure and pore size. In all inspected pores and over the whole pressure range, $S(i)$ is much greater than unity which indicates preferential adsorption of carbon dioxide. It shows that $S(i)$ is not very sensitive to the pressure in pores with a radius above $13\mathring{A}$ since $S(i)$ is almost constant when wider pores are added.

Figure 6.5: *3D surface map for dependency of selectivity on pressure and pore size for the binary mixture carbon dioxide - nitrogen.*

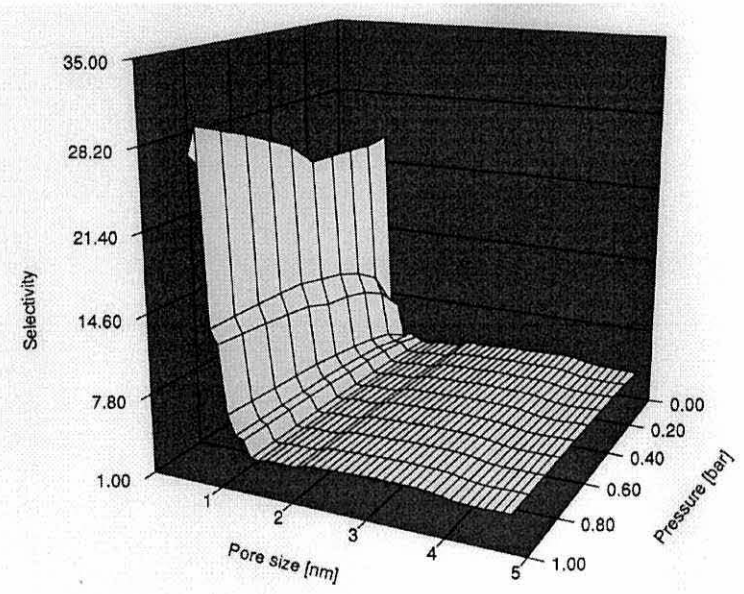

This general trend would also be expected at much higher pressures at which the majority of industrial adsorbers are used. The selectivity surface below a pore width of $13\mathring{A}$ is corrugated and reaches its maximum at the pore size of $8\mathring{A}$. The 3D image clearly illustrates that for efficient separation of carbon dioxide from nitrogen, a material with only a very narrow PSD is necessary ($7\mathring{A}$ to $11\mathring{A}$).

The 3D projection of Fig 6.5 onto constant pressure surfaces is shown in (Fig 6.6).

Figure 6.6: *Selectivity vs. pore size for the mixture carbon dioxide - nitrogen; P= 0.01 Bar, P=1 Bar.*

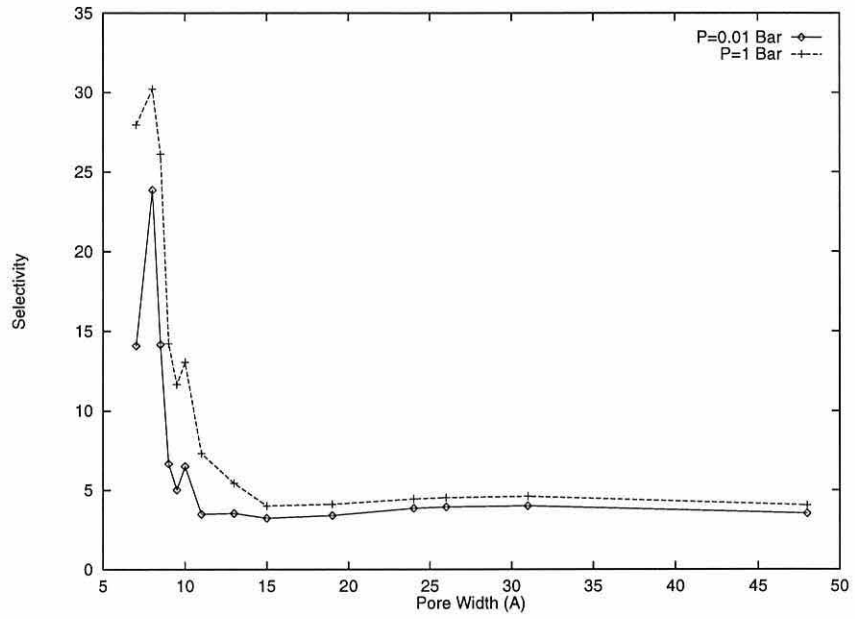

Selectivity isotherms (separation factor vs. pore size) display two maxima [30] which decay with additional pressure. The first sharp peak is located at the pore size $8\mathring{A}$, the second one at $10\mathring{A}$ and its appearance is more pronounced at higher pressures. In the model, the adsorbate molecules are treated as hard spheres with different σ_{ff} values [Table 4.7]. In ultra-narrow pores preferential adsorption of the larger carbon dioxide molecule is already reduced as shown in Figure 6.5 (where H=$7.0\mathring{A}$ and less). However, at H=$8\mathring{A}$ the peak appears, presumably due to the overlap of the potential walls. It seems that carbon dioxide molecules are particularly attracted by these additional forces. Since the additional attractive force disappears with increased pore size a selectivity minimum followed by the second maximum is observed.

Carbon Dioxide over Methane

Figures 6.7 and 6.8 are analogous to Figs 6.5 and 6.6 for the mixture carbon dioxide - methane.

Figure 6.7: *3D surface map for dependency of selectivity on pressure and pore size for the binary mixture carbon dioxide - methane.*

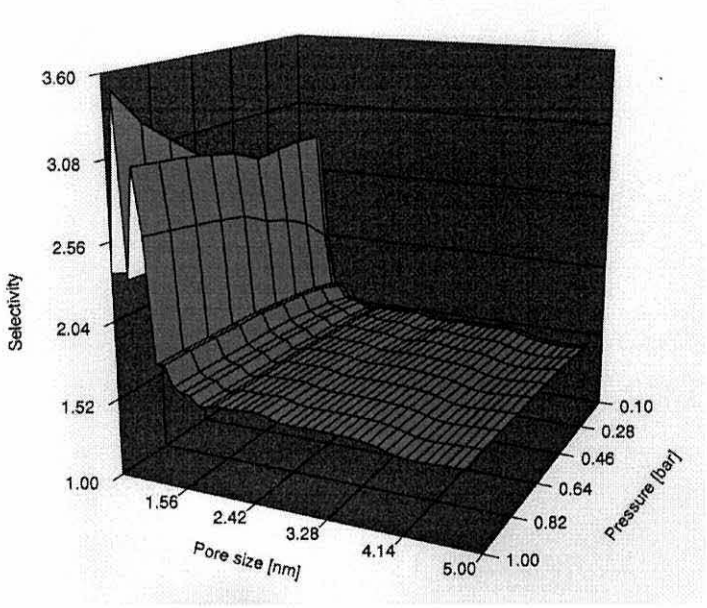

This system shows two sharp maxima separated by a pore size interval with much lower selectivity. These extremes are located at approximately the same pore sizes as found for the carbon dioxide - nitrogen mixture. Comparing Figs 6.5 and 6.7 we see that nitrogen is always less strongly adsorbed than methane, at least for the conditions studied here. The initial sharp peak in $S(i)$ is found at a pore size that is sufficient to accommodate a single layer of carbon dioxide molecules attracted by additional wall forces. As the pore size increases a second peak appears again. Relatively lower selectivity to carbon dioxide in ultra-narrow pores (H=7$\AA$) is likely due to the molecular sieving that occurs because of the carbon dioxide molecular

size.

Figure 6.8: *Selectivity vs. pore size for the mixture carbon dioxide - methane; P= 0.01 Bar, P=1 Bar.*

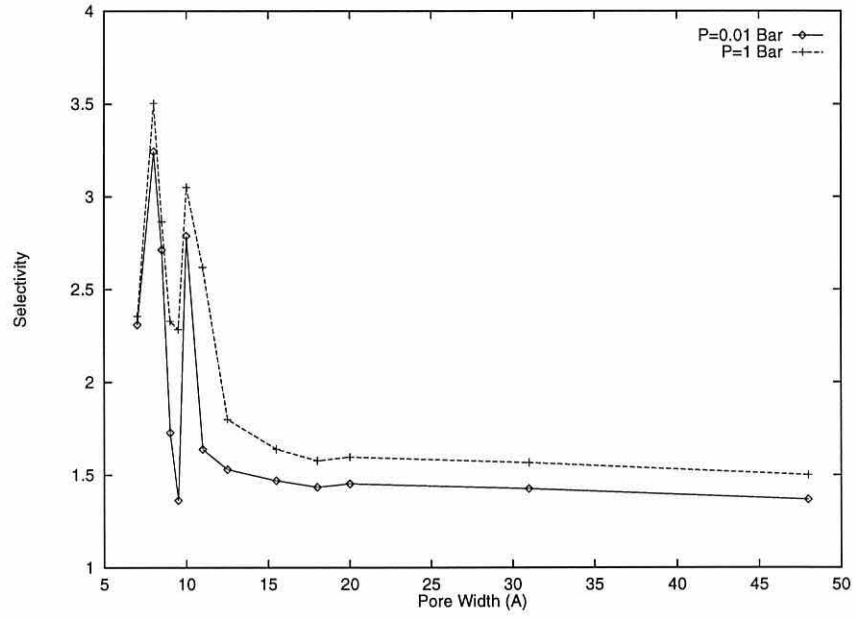

Design of the Microporous Structure

The design of the most suitable microporous structure for preferential adsorption of carbon dioxide from a *ternary* mixture (or higher mixtures) with methane and nitrogen could also be based in the prediction of behaviour of binary mixtures in adsorption. Generally, it is possible to evaluate the selectivity defined on the basis of Equation (6.4) for three gases. However, the information from the value of such a parameter is more general than that from combined $S(i)$ values for binaries.

The best way to design the structure of the prospective microporous material is based on the knowledge of the variation of the binary mixtures' separation factors

with the pore size at different pressures. A combination of pore size locations of the selectivity maxima for each of the mixtures shows a desirable microstructure profile. To maximise the efficiency of the adsorption, the selectivity maxima should be located at different well separated pore sizes. If the maxima overlap, competitive adsorption would take place, lowering the efficiency of the separation. If this is successfully achieved the proposed material is composed of regions which selectively adsorb a gas of interest from ternary or higher component gaseous mixtures. Each region is responsible for separation of the gas from a particular mixture. In the process of the microstructure design several pressures are usually worthy of inspection to find peaks with the best location.

Despite the different absolute values, the selectivity curves in Figs 6.6 and Fig 6.8 are very similar including maxima positions. It could be concluded that the PSD of a microporous material suitable for separation of carbon dioxide from a mixture with nitrogen and methane should mainly cover the region from 8.0$\mathring{A}$ to 11.0$\mathring{A}$ at the working pressure of a process at P=1 Bar. Due to the overlap of the most selective regions, competitive adsorption is likely to take place. This conclusion is, however, limited only to the model system presented here.

The $Sav.$ values were evaluated from the local selectivity isotherms, DFT databases and PSDs for AX21 computed from 293K carbon-dioxide experimental data and 293K local isotherm databases. Average selectivity ($S_{av.}$) isotherms for the mixtures carbon dioxide - methane and carbon dioxide - nitrogen are shown in (Fig 6.9) together with curves for $S_{exp.}$, which represent the behaviour of a real adsorbent (AX21), evaluated by IAS theory from experimental data (Fig 5.4). It is seen that

the agreement achieved between these two methods (a theory based selectivity approximation of the AX21 and its real behaviour in adsorption) is very good. The $S_{av.}$ values are, however, in general, slightly overestimated for both of the mixtures.

Figure 6.9: *Average Selectivity Isotherms for CO2/N2 and CO2/CH4 Mixtures.*

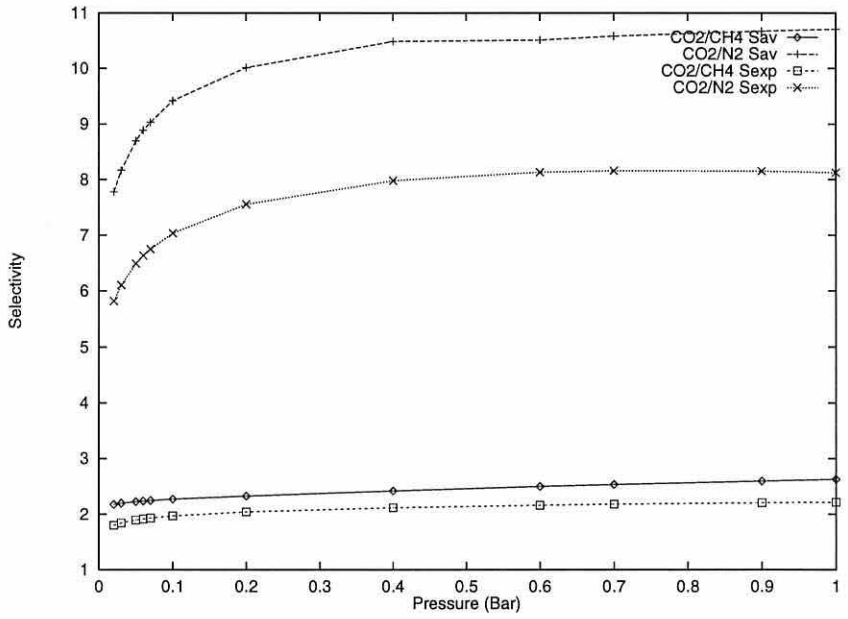

6.3 Conclusions

There are many advantages in using approximate theories to model the process of adsorption compared to measuring the adsorption isotherms experimentally. The most important comprises the fact that it is not possible to see in detail using experiments how adsorption isotherms and consequently selectivity isotherms change with varying pore size (or surface corrugation). A set of isotherms was generated by NL-DFT for the adsorption of nitrogen carbon-dioxide and methane on the model

surface of the microporous carbon with graphite slit-like pore geometry at 293K and pressures up to 1 Bar.

As discussed in Chapter 2, adsorbing molecules were modelled as one-centred hard spheres without quadrupole or partial charges. Fluid-fluid and solid-solid interactions were described by the Lennard-Jones (12-6) potential. For description of interactions of solid gas molecules with the graphitic surface the Steele (10-4-3) potential was chosen. Adsorption of the three gases was also measured experimentally at the same conditions on two model surfaces. AX21 microporous carbon represented a real adsorbent in this study. Experimental isotherms measured on non-porous graphitised carbon (Vulcan) were fitted by the large pore (H=360$\mathring{A}$) DFT generated data to evaluate potential parameters (Chapter 4). A variation of the shape of the DFT adsorption equilibrium curves with pore size was observed.

In ultra-narrow pores a monolayer formation appeared due to the additional attractive forces whose origin is in the overlap of potentials of opposite pore walls. The IAS theory was then used to predict multicomponent adsorption equilibria from DFT and experimentally measured adsorption isotherms. The IAS theory is not restricted to any particular type of semi-empirical fitting function. The best fits were obtained by using the Langmuir-Freundlich isotherm, which, despite an incorrect low pressure limit, described the data accurately over the whole pressure region. Separation factors obtained were discussed as functions of pressure and pore size. Carbon dioxide was preferentially adsorbed over nitrogen and methane from binary mixtures under the conditions studied here. The design/selection of the most suitable carbonaceous material (porous structure) was also based on separation factors

of binary mixtures. The micropore size interval of a carbonaceous adsorbent for selective adsorption of carbon dioxide from a mixture with nitrogen and methane should preferentially cover the region from 8.0 to 11.0$\mathring{A}$. Average selectivities evaluated from a set of DFT based local selectivity isotherms macroscopically represent a desirable real adsorbent and the agreement between experimental based selectivities and $S_{av.}$ was very good.

Chapter 7

Conclusions

The adsorptive properties of graphitic carbons were investigated by measuring their experimental uptake of nitrogen, argon and methane at 77K. Methane adsorption was found to occur much more readily than adsorption of argon or nitrogen. Non-local density functional theory based on statistical mechanics gives a good fit to experimental adsorption isotherms up to pressures of 0.1Bar for nitrogen and 0.02Bar for argon. The experimental adsorption of methane is more difficult to model since the adsorption isotherm show a sharper layering transition in this case. Although the non-local theory predicts the transition to a methane monolayer at approximately the right pressure, the region over which the monolayer forms is the most difficult to model accurately.

The magnitude of the fluid-fluid and solid-fluid interaction parameters obtained from the theoretical isotherms fitted to the experimental adsorbed amounts explain the differences between the experimental adsorption curves at 77K. Comparing the values of ϵ_{sf}/k for gas adsorption at 77K [Table 4.6] with the pressure range over which the monolayer forms, it is evident that the larger the value of ϵ_{sf}/k, the lower the monolayer completion pressure. We also showed that the larger the value of the molecular diameter, the lower the pressure at which the monolayer forms and the larger the value of ϵ_{ff}/k the steeper the gradient in the monolayer formation region.

Individual sets of parameters were evaluated by fitting to individual experimental isotherms for Vulcan, Sterling and graphite. However, it was shown that those parameters found for gases adsorbing onto Vulcan were applicable to all three materials. Thus the surfaces of Vulcan, Sterling and graphite are similar in the respect that their microstructure is approximated as a homogeneous sheet with no defects.

As Vulcan was shown to be a good approximation of a flat graphitic surface it was used as the standard for adsorption studies at room temperature.

At room temperature the amount of gas adsorbed varies exponentially with ϵ_{sf}/k, while ϵ_{ff}/k has no significant role at this temperature and pressures below 1Bar. Theoretical and experimental isotherms determined at higher pressures up to 50 Bar are required in order to investigate the role of the interaction parameters in the adsorption process at high temperatures. Under such conditions the rate of evaporation of the vapour from the surface will be reduced and a monolayer will be allowed to form.

Scanning electron microscopy and x-ray diffraction techniques provided some insight into the relative particle sizes of Vulcan, Sterling and graphite and explained much of the difference in calculated BET surface area values.

It was shown that the number of inflexion points in an experimental isotherm is a good indication of the number of peaks present in the pore size distribution. The step size in pore width in the NL-DFT databases is an important factor in determining the accuracy of the PSD and some previous studies were shown to use too small a step size. Further work is required to reduce the step size below $1\mathring{A}$ in more detailed calculations of adsorption isotherms to see if the PSD function f(H) is fully constrained.

Our calculation of the PSD of AX21 from nitrogen adsorption at 77K is an improvement on that presented previously [83] due to the smaller step size. The PSD's of microporous carbons Norit, Pica and Supersorbon have also been determined at 77K. Nitrogen and argon have both been used successfully as surface probes when

modelled as hard spheres. However, approximating the methane molecule as a hard sphere has been shown to be less appropriate since the resulting fits to the experimental isotherms of microporous carbons were much worse. Further work is required to improve the fit to a low-surface area carbon such as Vulcan in order to determine the PSD of porous carbons using methane as the adsorbate.

There are several features of the present analysis of PSDs that require further investigation. The fits to the experimental data for Vulcan could be improved by using more realistic molecular models of the Vulcan surface. The accuracy of the PSD could be improved by fitting the isosteric enthalpies as well as the adsorption isotherm [17], [2]. The change of the apparent PSD with temperature could be monitored by performing a series of isotherm measurements from temperatures above 293K to low temperatures. If pore blocking by freezing in pore junctions is occurring, the PSD at temperatures below 77K will not show pores at the smaller pore size range. The temperature at which the PSD changes will vary with the adsorbent and it will depend on whether the pore junctions induce freezing point elevation or depression.

The analysis of gas adsorption isotherms at 77K and room temperature for the typical high surface area activated carbon AX21 indicates that carbon-dioxide at room temperature is a more sensitive probe of micropore structure than nitrogen at 77K as the PSD extends to smaller pore widths. From high pressure data it should be possible to probe the full range of porosity. The universality of the PSD of AX21 from carbon-dioxide measurements at room temperature could be more rigorously tested by measuring adsorption at higher pressure and using a smaller

pressure interval between measurements.

The present knowledge on separation of carbon dioxide from carbon dioxide/methane and carbon dioxide/nitrogen binary mixtures on microporous carbonaceous adsorbents constitutes a good basis for further research. Especially promising is to treat nitrogen and carbon dioxide molecules as two-centred L-J spheres with quadrupole (or partial charges). This greater level of realism of the adsorption model has the potential to give further details (geometrical constraints, energetic aspects of optimal packing in pores, etc.) on preferential adsorption of carbon dioxide. It would also interesting to investigate selectivity results using molecular simulation techniques such as the GCMC method [117].

Appendix A

Lorentz-Berthelot Rules

For the interaction between unlike molecules the following expressions [4] are used which are based on the interactions between like molecules. The collision diameter is taken to be the arithmetic mean:

$$\sigma_{sf} = \frac{(\sigma_{ss} + \sigma_{ff})}{2} \tag{A.1}$$

and the well-depth is taken to be the geometric mean of those for the pure substances.

$$\epsilon_{sf} = (\epsilon_{ss} \text{ x } \epsilon_{ff})^{1/2} \tag{A.2}$$

Appendix B

Reduced Units

For convenience, quantities are scaled with respect to the fluid-fluid parameters and become dimensionless [6].

$$H^* = H/\sigma_{ff} \quad T^* = kT/\epsilon_{ff} \quad \rho^* = \frac{N}{V}$$
$$\sigma^3 = \rho\sigma_{ff}^3 \quad P^* = P\sigma^3/\epsilon_{ff} \quad \mu^* = \mu/\epsilon_{ff} \tag{B.1}$$

Appendix C

Conversion Factor

Conversion from reduced excess density to cubic centimetres of adsorbate per gram of adsorbate:

$$cc(STP)/g = \left(\frac{22400}{N_A} \text{x} \left(0.5 \text{x} \rho^*_{excess} \text{x} \left(\frac{H^*_{phys}}{\sigma^2_{ff}}\right)\right)\right) \text{x } S \tag{C.1}$$

Where N_A is Avogadro's constant, and S is the specific surface area of the adsorbent ($\text{m}^2.\text{g}^{-1}$).

Bibliography

[1] Kaneko, K.; Ishu, C.; Ruike, M.; Kuwabara, H. *Carbon.* **1992**, 30, 1075.

[2] Nicholson, D.; Quirke, N. *Studies in Surface Science and Catalysis.* **1999**.

[3] Walton, J. P. R. B.; Quirke, N. *Molecular Simulation.* **1989**, 2, 361.

[4] Rowlinson, J. S.; Swinton, F. L. *Liquids and Liquid Mixtures.* **1982**, Butterworths Monographs in Chemistry, p.280.

[5] Zemansky, M. W.; Dittman, R. H. *Heat and Thermodynamics.* **1981**, Sixth Edition, McGraw-Hill International Editions.

[6] Allen. M. P.; Tildesley, D. J. *Computer Simulation of Liquids.* **1989**, Oxford [England]: Clarendon Press; New York: Oxford University Press.

[7] Young, D. M.; Crowell, A. D. *Physical Adsorption of Gases.* **1962**, London: Butterworth, p.234.

[8] E04CCF - NAG Fortran Library Routine Document, Fortran Library Mark 17.

[9] Faust, S. D.; Aly, O. M. *Chemistry of Water Treatment.* **1983**, London: Butterworths.

[10] Letoquart, C., Rouquerol, F., Rouquerol, J. *Journal de Chimie Physique.* **1983**, 70, 559.

[11] Marsh, H. *Carbon.* **1991**, 29, 703.

[12] Maddox, M. W.; Gubbins, K. E., Quirke, N. *Molecular Simulation.* **1997**, 19, 267.

[13] Private discussion with Quirke, N.

[14] Miyahara, M.; Kanda, K.; Higashitani, K; Gubbins, K. E. *Preprint.*

[15] Radhakrishnan, R.; Gubbins, K. E. *Private communications.*

[16] Kluson, P.; Scaife, S. J.; Quirke, N. *In preparation.*

[17] Kluson, P.; Scaife, S. J.; Quirke, N. *Submitted J. Phys. Chem.*

[18] Kluson, P.; Scaife, S. J.; Quirke, N. *In preparation.*

[19] Pauly, H.; Toennies, J. P. *Advances in Atomic and Molecular Physics.* **1965**, Vol .1, Bates, D. R.; Eastermann, I. Academic Press, New York.

[20] Tan, Z.; Marini Bettolo Marconi, U.; van Swol, F.; Gubbins, K. E. *J. chem. Phys.* **1989**, 90, 3704.

[21] Evaluations carried out by Dr P. Kluson.

[22] Jaroniec, M.; Patrykiejew, A.; Borowko, M. *In Progress in Membrane and Surface Sciencs.* **1981**, Vol.14. [Edited by Cadenhead, D. A.; Danielli, J. F. Academic Press, New York, pp1-68.]

[23] Jones, R. O.; Gunnarsson, O. *Review of Modern Physics.* **1989**, Vol 61, No.3.

[24] Parr, R. G.; Yang, W. *Density Functional Theory of Atoms and Molecules.* **1989**, Oxford University Press, Oxford, p.689.

[25] Jackson, E. Atlee. *Equilibrium Statistical Mechanics.* **1968**.

[26] Atkins, P. W. *Physical Chemistry.* Fourth Edition. **1990**, p.578.

[27] Atkins, P. W. *Physical Chemistry.* Fourth Edition. **1990**, p.884.

[28] Weltner, K.; Grosjean, J.; Schuster, P.; Weber, W. J. *Mathematics for Engineers and Scientists.* **1986**, Stanley Thornes (Publishers), p.416.

[29] Brunauer, S.; Deming, L. S.; Deming, W. S.; Teller, E. *J. Amer. Chem. Soc.* **1940**, 62, 1723.

[30] Brunauer, S.; Emmett, P. H.; Teller, E. *J. Amer. Chem. Soc.* **1938**, 60, 309.

[31] Miller, G. F. *Numerical Solution of Integral Equations.* **1974**, Delves L. M.; Walsh, J. Eds.; Clarendon: Oxford; Chapter 13, p175.

[32] McEnaney, B.; Mays, T. J.; Causton, P. D. *Langmuir.* **1987**, 3, 695-699.

[33] Everett, D. H.; Powl, J. C. *J. Chem. Soc. Faraday Trans.* **1976** I, 72, 619.

[34] Horvath, G.; Kawazoe, K. *J. Chemical Engineering Jap.* **1983**, 16(6), 470.

[35] Bansal, R. C.; Donnet, J.; Stoeckli, F. *Active Carbon.* **1988**, Marcel Dekker: New York. Chapters 2 and 3.

[36] Seifert, J.; Emig, G. *Chem. Ing. Tech.* **1987**, 59(6), 475-485.

[37] Seifert, J. *Diploma Thesis.* **1985**, University Erlangen-Nurenburg.

[38] Mikhail, R.; Brunauer, S. H.; Bodor, E. E. *J. Colloid and Interface Sc.* **1968**, 26, 45-53.

[39] Carnahan, N. F.; Starling, K. E. *J. Chem. Phys.* **1969**, 51, 635.

[40] Evans, R. *Adv. Phys.* **1979**, 28, 143; Evans, R. *Fundamentals of Inhomogeneoues Fluids.* **1992**, 85.

[41] Gubbins, K. E. *Fluid Physics, Lecture Notes of Summer Schools.* **1994**; Gray, C. G.; Gubbins, K. E.; Joslin, C. G. *Theory of Molecular Fluids.* **1996**, 2, 8.

[42] Tarazona, P. *Phys. Rev.* **1985**, A31, 2672.

[43] Allen, M. P.; Tildesley, D. K. *Computer Simulation of Liquids.* **1987**, Oxford University Press, Oxford.

[44] Gubbins, K. E.; Quirke, N. *Molecular Simulation and Industrial Processes: Methods, Applications and Prospects.* **1996**.

[45] Lastoskie, C.; Gubbins, K. E.; Quirke, N. *J. Phys. Chem.* **1993**, 97, 4786.

[46] Lastokie, C.; Gubbins K. E.; Quirke, N. *Langmuir.* **1993**, 9, 2693.

[47] Lastoskie, C.; Gubbins K. E.; Quirke, N. *Characterization of Porous Solids 111.* **1993**, 51.

[48] Olivier, J. P.; Conklin, W. B.; Szombathely, M .von. *Characterization of Porous Solids 111.* **1994**, 81.

[49] Olivier, J. P. *Adsorption.* **In press.**

[50] Lastoskie, C.; Quirke, N.; Gubbins, K. E. *Equilibria and Dynamics of Gas Adsorption on Heterogeneous Solid Surfaces.* **In press.**

[51] Ebner, C.; Saam, W. F.; Shroud, D. *Phys. Rev. A.* **1976**, 14, 2264.

[52] Yang, A. J. M; Fleming, P. D.; Gibbs, J. H. *J. Chem. Phys.* **1976**, 64, 3732.

[53] Gubbins, K. E; Verlarde, M. G; Christov, C. I; Joslin, C. G. *Theory of Molecular Fluids.* **1994**, Vol 2, Chapter 8, in press.

[54] Kierlik, E; Rosinberg, M. L. *J. Chem. Phys.* **1990**, A42, 3382.

[55] Gregg, S. J.; Sing, K. S. W. *Adsorption, Surface Area and Porosity.* **1982**, London: Academic Press, Chapters 3 and 4.

[56] Patrick, J. W. *Porosity in Carbons.* **1995**, Edward Arnold Publishers.

[57] Gregg, S. J.; Sing, K. S. W. *Adsorption, Surface Area and Porosity.* **1982**, London: Academic Press, p.49.

[58] *Coulter Omnisorp Reference Manual* **1992**, Coulter Electronics Limited, Northwell Drive, Luton, Beds, LU3 3RH, England.

[59] Langmuir, I. *J. Amer. Chem. Soc.* **1916**, 38, 2221.

[60] Young, D. M.; Crowell, A. D. *Physical Adsorption of Gases.* **1962**, London: Academic Press, p174.

[61] Sing, K. S. W.; Everett, D. H.; Haul, R. A. W.; Moscou, L.; Pierotti, R. A.; Rouquerol, J.; Siemieniewska, T. *Pure and Applied Chemistry.* **1985**, 57, 603.

[62] de Boer, J. H.; Linsin, B. G.; Osinga, T. J. *J. Catal.* **1965**, 4, 643.

[63] Carrott, P. J. M.; Sing, K. S. W. *Pure and Applied Chemistry.* **1989**, 61, 1835.

[64] Sing, K. S. W. *Carbon*, **1989**, 27, 5.

[65] Gregg, S. J.; Sing, K. S. W. *Adsorption, Surface Area and Porosity.* **1982**, London: Academic Press, Chapters 2 and 4.

[66] Venero, A. F.; Chiou, J. N. *Mat. Res. Society Symp. Proc.* **1988**, Vol 111.

[67] Dubinin, M. M.; Serpinskii, V. V. *Carbon.* **1981**, 19, 402.

[68] Seeley, S, B. *Natural Graphite, Kirk-Othmer Encyclopedia of Chemical Technology.* **1978**, Volume 4, John Wiley and Sons, New York.

[69] Soffel, R, W. *Carbon and Artificial Graphite, Kirk-Othmer Encyclopedia of Chemical Technology.* **1978**, Volume 4, John Wiley and Sons, New York.

[70] *Powder Diffraction File of the JCPDS - International Centre for Diffraction Data.* **1978**, Swathmore-Pennyslvania.

[71] Emmett, P. H.; Brunauer, S. *J., Amer. Chem. Soc.* **1937**, 59, p1553.

[72] Ross, S.; Olivier, P. J. *On Physical Adsorption.* **1964**, Interscience: New York, p187.

[73] Sing, K. S. W. *Pure. Appl. Chem.* **1982**, 54, p2201-18.

[74] Gregg, S. J.; Sing, K. S. W. *Adsorption, Surface Area and Porosity.* **1982**, London: Academic Press, Chapter 1, p53.

[75] *Handbook of Chemistry and Physics.* **1984-1985**, pD-215, 65th Edition.

[76] Olivier, J. P. *Journal of Porous Materials.* **1995**, 2, 9-17.

[77] Maglara, E.; Pullen, A.; Sullivan, D.; Conner, W, C. *Langmuir.* **1994**, Vol.10, No.11, p4167-4173.

[78] Conner, W.; Fraissard, J.; Bonardet, J.; Unger, K.; Kumar, D.;Ferrero, M.; Ragle, J. *Studies of Surface Science and Catalysis.* **1994**, Roquerol, Ed.; Elsevier: New York.

[79] Conner, W. C.; Ferrero, M.; Bonardet, J.; Fraissard, J. *J. Chem. Soc., Faraday Trans.* **In press**.

[80] Laboratory of the Government Chemists, Teddington, UK.

[81] BDH Laboratory Gas Services.

[82] Locke, W. *J. Phys. Chem.* **1947**, 51, 644.

[83] Lastoskie, C.M. *PhD Thesis.* **1994**, Cornell University.

[84] Coulter Electronics Limited, Northwell Drive, Luton, Beds, LU3 3RH, England.

[85] Hirschfelder, J. O.; Curtiss, F. C.; Bird, R. B. *Molecular Theory of Gases and Liquids.* **1954**, John Wiley and Sons, Inc., New York Chapman and Hall, Ltd, London.

[86] Sing, K, S, W.; *Colloids and Surfaces.* **1989**, 38, 113.

[87] Weissermel, K; Arpe, H. J. *Industriele Organische Chemie.* **1978**, VCH, Weinhem.

[88] Ertl, G.; Knzinger, H.; Weitkamp, J, *Handbook of Heterogeneous Catalysis.* **1997**, VCH, Weinheim.

[89] Thampi, K. R.; Kiwi, J.; Graeizel, M. *Nature.* **1987**, 327, 506.

[90] Thomas, J. M.; Thomas, W. J. *Principles and Practise of Heterogeneous Catalysis.* **1997**, VCH, Weinheim.

[91] Myers, J.; Prausnitz, M. *A.I.Ch.E. Journal.* **1965**, 11, 121.

[92] O'Brien, J.; Myers, A. L. *Ind. Eng. Chem. Process Des. Dev.* **1985**, 24, 1188.

[93] O'Brien, J.; Myers, A. L. *Ind. Eng. Chem. Res.* **1988**, 27, 2085.

[94] Sircar, S.; Myers, A. L. *Surf. Sci.* **1988**, 205, 353.

[95] Eiden, U. *Chem. Eng. Process.* **1990**, 28, 1.

[96] Evans, R. *J. Phys. Cond. Matter 2.* **1990**, 8989.

[97] Tarazona, P.; Evans, R. *Molec. Phys.* **1984**, 52, 847.

[98] Kierlik, E.; Rosinberg, M. *Mol. Phys.* **1992**, 75, 1435.

[99] Kierlik, E.; Rosinberg, M. *Phys. Rev. A.* **1991**, 44, 5025.

[100] Quirke, N.; Tennison, S. *Carbon* **1996**, 34/10, 1281.

[101] Cracknell, R. F; Nicholson, D. *Adsorption 1.* **1995**, 7.

[102] Cracknell, R. F.; Nicholson, D.; Tennison, S; Bromhead, J. *Adsorption 2.* **1996**, 193.

[103] Kaneko, K.; Cracknell, R. F.; Nicholson, D. *Langmuir 10.* **1994**, 4606.

[104] Sing, K. S. W. *Pure Appl. Chem.* **1985**, 57, 603.

[105] Shigeta, T.; Yoneta, Y.; Nitta, T. *Mol. Sim. 16.* **1996**, 291.

[106] Turner, A. R.; Quirke, N. *Carbon.* **In print.**

[107] Cracknell, R. F.; Nicholson, D.; Quirke, N. *Mol. Sim. 13.* **1994**, 161.

[108] Cracknell, R. F.; Nicholson, D.; Quirke, N. *Mol. Phys.* **1993**, 80, 185.

[109] Kierlik, E.; Rosinberg, M.; Finn, J. E.; Monson, P. A. *Mol. Phys.* **1992**, 75, 1435.

[110] Richter, E.; Schutz, W.; Myers, A. *Chem. Eng. Sci.* **1989**, 44/8, 1609.

[111] Costa, E.; Sotelo, L.; Calleja, G.; Marron, C. *A.I.Ch.E. Journal.* **1981**, 27, 5.

[112] Dune, J.; Myers, A. L. *Chem. Eng. Sci.* **1994**, 49, 2941.

[113] Tan, Z.; Gubbins, K. *J. Phys. Chem.* **1992**, 96, 845.

[114] Kluson, P.; Scaife, S. J.; McGrother, S.; Quirke, N. **In preparation.**

[115] Sirkar, S. *J. Colloid. Interface Sci.* **1984**, 101, 452.

[116] Belohlav, Z.; Zamostny, P.; Kluson, P.; Volf, J. *Can. J. Chem. Eng.* **1997**, 75, 735.

[117] Leach, A. R. *Molecular Modelling Principles and Applications.* **1996**, Longman Singapore Publishers (Pte) Ltd, p.396.

[118] Freundlich, H. *Colloid and Capillary Chemistry (trans 1.).* **1926**, Metheun, London, pp110-134.

[119] Ryan, T. P. *Modern Regression Methods.* **1997**, John Wiley and Sons, New York.